Journal of the CERAMIC SOCIETY of Japan,
International Edition
Vol.99 Feb.1991

Journal of Ceramic Society of Japan, *International Edition*

CONTENTS

Information & Communications

Cover

A concept has been proposed by Japanese scientists to solve the problems of using ceramics as structural materials.

Ceramics are highly heat resistant but have low fracture toughness, while metals have high fracture toughness but less heat resistance. If a new material with the combined advantages of metals and ceramics could be created, it would solve the problems, and thus the concept has been proposed that ceramics and metals should be laminated in layers of atomic order thickness ranging from 100% metal to 100% ceramic. A material with this kind of functional gradient may have the fracture strength of metal combined with the high-temperature resistance of ceramics.

(clockwise from upper left)

1) Cross-sectional surface of SiC-C FGM by SEM
2) Cross-sectional surface of SiC-C FGM by EPMA. (1 & 2: Courtesy of Dr. Hirai and Dr. Sasaki, Institute for Materials Research, Tohoku University)
3) Example of microscopic observation of ZrO_2-Ni FGM made by the thin-film lamination method. This sample is a sintered lamination from 100% ceramic to 50% ceramic (Courtesy of Dr. Tamura, NKK)
4) Cross-section photo of C-SiC FGM coated on C/C composite. The composition continuously changes from C to SiC. (Courtesy of Dr. Igarashi and Mr. Kawai, Sumitomo Electric Industries, Ltd.)

Papers, Letters and Notes

High resolution electron microscope photograph of the modulation doped structure of $Bi_2Sr_2CaCu_2O_y$ ($T_c = 80K$) in the [100] direction. Figures at right side indicate number of copper layers, symbol B indicates bismuth rich region.

Synthesis of $K_2Ti_4O_9$ by the Hydrolysis of $KOH-Ti(iso-C_3H_7O)_4$ Ethanol Solution

Yoshihito Sakurai and Tetsuro Yoshida

Department of Chemistry, Faculty of Science and Engineering, Meisei University, Hodokubo, Hino-Shi, Tokyo 191, Japan

The precipitates with a TiO_2/K_2O mole ratio=4 were obtained by hydrolysis of $KOH-Ti(iso-C_3H_7O)_4$ ethanol solutions. The dried product was amorphous changed to a crystalline intermediate by heat-treating at about 600°C.
The well grown submicron crystals of $K_2Ti_4O_9$ were obtained by heat-treatment at 1000°C for 1h.

1. Introduction

The crystals of potassium tetratitanate $K_2Ti_4O_9$[1,2] have a layer structure, and it is possible from them to obtain hydrogen tetratitanate hydrate ($H_2Ti_4O_9 \cdot nH_2O$) by the acid treatment. These hydrated crystals are noticed to be useful for cation exchangers. In the case of melting method, $K_2Ti_4O_9$ is formed by peritectic reaction of $K_2Ti_6O_{13}$ and melt during cooling.[3] This reaction proceeds slowly if the molten oxides of stoichiometric composition are cooled from high temperature and so the crystals of single phase are difficult to obtain. It is also difficult to obtain well grown crystals by sintering the dry mixtures.

The experimental results were reported in the previous paper.[3] The mixed ethanol solution of metal alkoxides was hydrolyzed, and the amorphous precipitates were heat-treated at a temperature lower than the peritectic temperature and the well grown crystals of single phase $K_2Ti_4O_9$ were obtained.
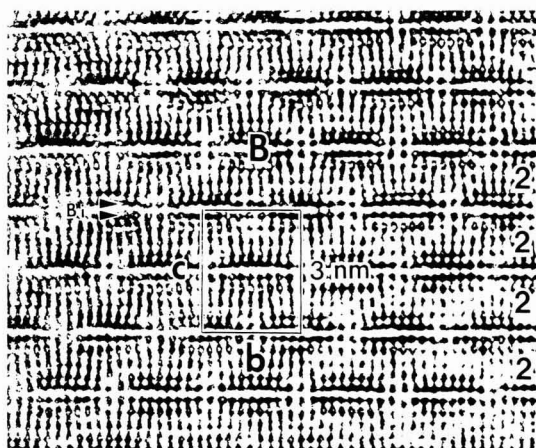
In this paper, the synthesis of $K_2Ti_4O_9$ crystals was carried out by using the more stable and useful reagent KOH in place of potassium alkoxides. One of the hydrolysis products, KOH, is known to be dissolved about 29wt% in C_2H_5OH at 28°C. However, it reacted with the hydrolysis product of titanium isopropoxide directly and the precipitates which were insoluble in the water-ethanol solution were obtained. The dried precipitates were amorphous. However, well grown submicrometer-sized crystals of $K_2Ti_4O_9$ single phase were obtained by heat-treating the dried precipitates.

2. Experimental Procedure

All chemicals used were of reagent grade and without any purification. Ethanol was treated by molecular sieve for 24h for dehydration, and 10%KOH ethanol solution was prepared. The apparatus for hydrolysis was the same as in the previous paper. However, the pH values of filtrates were measured after the dilution of filtrates to 1/100 to eliminate the obstruction of ethanol and by using the glass electrode pH meter HM-7E together with HM-20S (Toa Electronics Ltd.) in this paper.

The synthetic procedure of $K_2Ti_4O_9$ is as follows. Ti(iso-$C_3H_7O)_4$ was added to 1) 10wt%$(CH_3)_3COK$ ethanol solution or 2) 10wt%KOH ethanol solution and the mixed ethanol solutions were obtained. They were hydrolyzed by adding water-ethanol solutions (water content 9.5–63wt%). The hydrolysis reactions were carried out at 72–75°C for 1h by stirring and refluxing. The hydrolysis products were sealed in a Teflon container and preserved in water bath at 30°C for 24h for aging. The amounts of unreacted KOH remaining in the filtrates were estimated by the measurements of their pH values. The precipitates were dried at 100°C for 24h. The dried precipitates were heat-treated at various temperatures. The heat-treated samples were analyzed by X-ray diffraction (XRD) to identity crystalline phases and morphological observation was carried out by scanning electron microscopy (SEM).

3. Results and Discussion

3.1. The Hydrolysis Conditions and Products

The hydrolysis reaction of the mixed alkoxides in ethanol solution is

$$2(CH_3)_3COK+4Ti(iso-C_3H_7O)_4+18H_2O$$
$$= 2KOH+4Ti(OH)_4+2(CH_3)_3COH$$
$$+16iso-C_3H_7OH \quad \dots \dots \dots \dots \dots (1a)$$
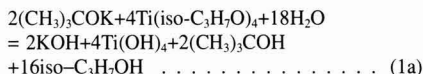
Then the dehydration and crystallization reaction take place by drying and heat-treating.

$$2KOH+4Ti(OH)_4 = K_2Ti_4O_9+9H_2O \quad \dots \dots (1b)$$

Therefore totally

$$2(CH_3)_3COK+4Ti(iso-C_3H_7O)_4+9H_2O$$
$$= K_2Ti_4O_9+2(CH_3)_3COH+16iso-C_3H_7OH \dots (1)$$

and

$$2KOH+4Ti(iso-C_3H_7O)_4+7H_2O$$
$$= K_2Ti_4O_9+16iso-C_3H_7OH \quad \dots \dots \dots \dots (2)$$
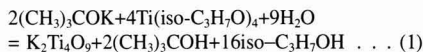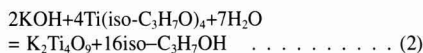
when KOH is used.

From Equation (1), the mole ratio of K-tert-butoxide: Ti-isopropoxide: H_2O is 1:2:4.5 in formular weight. On the other hand, from Equation (2) KOH: Ti-isopropoxide: H_2O is 1:2:3.5.

The amounts of unreacted KOH remaining in filtrate after the hydrolysis were compared in the case of using KOH with K-alkoxide ($(CH_3)_3COK$) by the experiments

Table 1. The conditions of hydrolysis and the identified crystalline phase after calcination.

Sample No.	Starting Material	Hydrolysis Reaction (temp/°C)	Aging (time/d)	[TiO₂]/[K₂O] mole ratio	[H₂O]/[K₂O] mole ratio (a)	[C₂H₅OH]/[K₂O] mole ratio	Filtrate pH	Crystalline phase. after calcined at 1000°C,1h
1	(CH₃)₃COK	72—75	1	4.0	9.0(1.0)	48	6.8	T
2	KOH	72—75	1	4.0	7.0(1.0)	48	6.3	T
3	(CH₃)₃COK	72—75	1	4.0	18(2.0)	48	6.6	T
4	KOH	72—75	1	4.0	28(4.0)	48	6.6	T
5	KOH	72—75	1	4.0	74(11)	48	6.7	T

a):multiples of· formular ratio

T: $K_2Ti_4O_9$
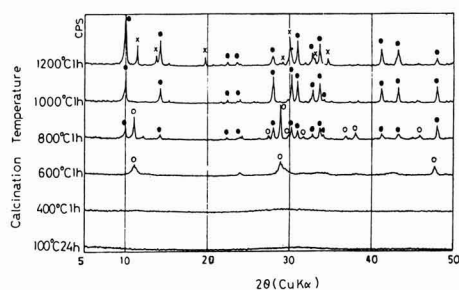
Fig. 1. XRD pattern of sample No.2 using KOH after heat-treated at various temperatures.

○: intermediate, ●: $K_2Ti_4O_9$, X: $K_2Ti_6O_{13}$

No.1-5 are shown in **Table 1**. The hydrolysis conditions such as reaction temperature (72–75°C), total ethanol quantity ([C₂H₅OH]/[K₂O]=48), aging time (1 day) and temperature (30°C) were selected to be the same. The pH values of the filtrates in samples No.1-5 were less than or nearly equal to 7. The pH values of less than 7 were considered to be equilibrated ones by absorbing CO_2 in the atmosphere during the measurements. The ion exchanged pure water used for the dilution of the filtrates at the pH measurement also showed nearly the same value of pH. Therefore, KOH quantities in these filtrates were considered to be negligibly small from their pH values. These results were nearly the same when the water content was increased from mole ratio H_2O/K_2O=7.0 to 74. KOH reacted with the hydrolysis product of titanium isopropoxide, and the precipitates which TiO_2/K_2O mole ratio=4 were obtained.

3.2. Change of Hydrolysis Product by Heat-treatment and Crystal Growth

The XRD pattern of the sample No.1-5 showed nearly the same change when heat-treated at various temperatures. The typical XRD pattern of the samples prepared by using KOH was shown in **Fig.1**. The only halo with maximum at about d=0.3nm (2θ=29°) caused by amorphous structure was observed in the samples which were dried at 100°C for 24h and heat-treated at 400°C for 1h. The crystalline diffraction lines began to appear in the sample heat-treated at 600°C. These lines are different from those of $K_2Ti_4O_9$ (mark●) and unknown. This unknown crystalline phase disappears when crystals of $K_2Ti_4O_9$ are formed by heat-treating at the higher temperature. Therefore, these diffraction lines are considered to be those of intermediate crystals (mark ○).

Table 2. XRD analysis of sample prepared by this method.

$K_2Ti_4O_9$,Dion et al (1981)JCPDS32-861			sample No.2 (1000°C,1h)	
d(A)	I/I₁	hkl	d(A)	I/I₁
8.76	100	200	8.803	100
6.19	35	201	6.197	48
5.75	2	002	-----	--
4.09	1	40$\bar{2}$	-----	--
3.95	3	20$\bar{3}$	3.962	12·
3.75	3	401	3.751	8
3.71	2	110	3.707	13
3.18	35	310	3.181	87
3.08	<1	402	-----	--
			2.999	11
2.95	35	311	2.953	97
2.88	30	004	2.884	78
2.80	1	40$\bar{4}$	-----	--
			2.749	13
2.72	20	60$\bar{3}$	2.728	43
2.66	30	31$\bar{3}$	2.658	71
2.62	4	312	2.618	12
2.55	<1	51$\bar{2}$	2.555	7
2.344	3	11$\bar{4}$	2.344	8
2.270	<1	80$\bar{1}$	----	-
2.186	25	512	2.188	56
2.089	25	205	2.089	55
2.047	2	71$\bar{3}$	-----	-
1.986	2	314	1.987	10
1.895	10	020	1.895	59
1.854	2	220	1.852	7
1.838	1	405	1.837	7
1.827	2	712	1.824	9
1.752	2	91$\bar{3}$	1.752	13
1.744	8	11$\bar{6}$	1.742	20

An exothermic peak corresponding to this crystallization was observed at 560–580°C in DTA of samples No.1–5. A mixed phase of intermediate and $K_2Ti_4O_9$ crystals was observed when heat-treated at 800°C for 1h. The only sharp diffraction lines of $K_2Ti_4O_9$ crystal were observed in the sample heat-treated at 1000°C for 1h and their intensities were substantially increased. Therefore, the samples heat-treated at 1000°C are confirmed to be well grown $K_2Ti_4O_9$ crystals. In the sample heat-treated at 1200°C for 1h, the deposition of $K_2Ti_6O_{13}$ (mark X) was observed which was caused by the incongruent melting of $K_2Ti_4O_9$ by the peritectic reaction $K_2Ti_4O_9 \rightarrow K_2Ti_6O_{13}$+melt at 1114°C. $K_2Ti_4O_9$ was identified by the results of Dion et al.[4] as shown in **Table 2**. Good agreement is obtained except for weak diffraction lines (2.999(Å) and 2.749(Å)), which confirmed to belong to diffraction lines other than $K_2Ti_4O_9$. The reason is now under investigation.

Figure 2 shows the SEM photographs of sample No.2 which was dried at 100°C for 24h and heat-treated at 600°C, 800°C and 1000°C for 1h respectively. The dried precipitates were amorphous and aggregated as shown in

about 600 to 800nm in length; these were confirmed to be $K_2Ti_4O_9$ crystals by XRD analysis and the plate-like crystals disappeared (Fig.2-d).

4. Conclusion

The synthesis of $K_2Ti_4O_9$ crystals was investigated by hydrolyzing the mixed KOH and $Ti(iso-C_3H_7O)_4$ ethanol solution and heat-treating the hydrolysis product.

The results are as follows:

1) All hydrolysis products were amorphous and insoluble in the water-ethanol solutions when TiO_2/K_2O mole ratio=4.0.

2) The dried precipitates heat-treated at 600°C for 1h were changed from amorphous to intermediate crystals.

3) The intermediate crystals were changed to well-grown $K_2Ti_4O_9$ crystals by heat-treating them at 1000°C for 1h.

4) No difference between of starting material $(CH_3)_3COK$ and KOH was found from the above results. Therefore, it was confirmed that the synthesis of $K_2Ti_4O_9$ crystals was possible by using KOH as well as K-alkoxide.

References:

1) H. Izawa, S. Kikkawa and M. Koizumi, J. Phys. Chem., 86, 5023-26 (1982).

2) Y. Fujiki, Y. Komatsu and T. Sasaki, Hiyoumen, 24, 683-91 (1986).

3) Y. Sakurai and T. Yoshida, Nippon Kagaku Kaishi, 1989, 33-38.

4) M. Dion, Y. Piffard and M. Tournoux, J. Inorg. Nucl. Chem., 40, 917-18 (1978), (JCPDS 32-861).

Fig. 2. SEM photographs of sample No.2 heat-treated at various temperatures
(a) 100°C, 24h (b) 600°C, 1h (c) 800°C, 1h (d) 1000°C, 1h (bar=1μm)

Fig.2-a. A small angle scattering was observed in the XRD pattern of this sample. However, the scattering disappeared when heat-treated at 400°C for 1h. Its SEM image was observed to be nearly same as shown in Fig.2-a. By heat-treating at 600°C for 1h, the dried precipitates were changed to crystalline intermediates which were identified by XRD analysis as shown in Fig.1, and rather amorphous than crystalline in shape (Fig.2-b). They were changed to a mixture of pillar-like and plate-like crystals when heat-treated at 800°C for 1h (Fig.2-c). The samples heat-treated at 1000°C for 1h were well grown pillar-like crystals of

Forming of Alumina Powder by Electrophoretic Deposition

Yoshihiro Hirata, Akihiko Nishimoto and Yoshimi Ishihara

Department of Applied Chemistry, Faculty of Engineering, Kagoshima University
1-21-40 Korimoto, Kagoshima 890, Japan

The electrophoretic deposition method was used to form an alumina layer with a thickness of about 1mm. Alpha alumina powders with average diameters of 0.2 and 0.6μm were dispersed in water at pH 2.5 to provide positive charge. Positively charged alumina particles in the aqueous suspension of 15vol% solid were deposited on a cylindrical carbon electrode by passing direct current of 5–200mA at 50–300V. The weight of the alumina layer was proportional to the deposition time and applied voltage. Electrolysis of the HCl solution occurred together with the electrophoretic deposition of alumina particles. The deposition efficiency calculated from the deposition rate of alumina particles was in the range of 0.13 to 0.15. The density and thickness of the formed alumina layer increased periodically with deposition time. The alumina layers with relative densities of 56-62%, formed from the 0.6μm-alumina powder, were sintered at 1100°–1500°C in air. The densification rate was reduced above 1400°C by large pores (200–500μm).

1. Introduction

The physicochemical or mechanical properties of advanced ceramics change greatly with their microstructures. For the processing of submicrometer particles, slip casting method using colloidal particles is superior to dry pressing in controlling the microstructure and density fluctuation of consolidated powder compacts.[1-8] This slip casting method is industrially useful to form the products of complicated shape which can not be formed by dry pressing. However, it takes a long time in slip casting method for the consolidation of colloidal particles and the drying of consolidated powder compacts. On the other hand, electrophoretic deposition is highly expected in for short-time forming of charged colloidal particles. By literature search of electrophoretic deposition at 1986-1990, it was found that this processing is widely applied to form many kinds of ceramics such as β, β''-alumina,[9-11] Al2O3,[12] apatite,[13,14] and superconducting ceramics.[15-18] This processing has the following advantages: (i) short-time forming, (ii) easy control of the thickness of products, (iii) little restriction on the shape of products, depending on the shape of electrodes, and (iv) being adequate for mass production. In addition to the above features, there are still problems such as gas appearance by the electrolysis of liquid media, which disturbs

the uniformity of the deposited layer of colloidal particles. The purposes of this research were to clarify (i) the deposition mechanism of colloidal particles in electrophoretic processing, (ii) properties of the deposited particle layer (density and microstructure), and (iii) sintering behavior of the green layer. An experiment of electrophoretic processing was done with the aqueous colloidal suspensions of α-alumina particles of the average diameters of 0.2 and 0.6μm, and carbon and platinum electrodes.

2. Important Parameters Affecting Electrophoretic Forming

To understand clearly the forming characteristic by electrophoretic deposition, we analyze the Faraday's law as follows. The deposition weight (w) of charge carrier i per unit area of electrode is expressed by Eq. (1),

$$\frac{w}{M} = \frac{Q_i}{Z_i F} = \frac{I_i t}{(Z_i e) N} \quad \cdots \cdots \cdots \cdots (1)$$

where

M = the weight of i particles of Avogadro's number (N),
Q_i = the electric charge carried by i particles
I_i = the electric current density of i particles
t = time
Z_i = the valence of per particle
F = Faraday's constant (F=Ne)
e = the electronic charge
$Z_i e$ = the charge per particle.

Equation (1) is transformed into Eq. (2).

$$w = \frac{1}{Z_i e} \frac{M}{N} I_i t \quad \cdots \cdots \cdots \cdots \cdots (2)$$

The weight of one i particle (M/N) is equal to Eq. (3),

$$\frac{M}{N} = \frac{C_i}{n_i} \cdots \cdots \cdots \cdots \cdots \cdots \cdots (3)$$

where C_i is the weight of i particles per unit volume and n_i the number of i particles per unit volume. From Eqs. (2) and (3), we obtain Eq. (4).

$$w = \frac{C_i}{n_i (Z_i e)} I_i t \quad \cdots \cdots \cdots \cdots (4)$$

Electric current density is defined by Eq. (5),[19]

$$I_i = \sigma_i \left(\frac{d\phi}{dx}\right) \quad \cdots \cdots \cdots \cdots \cdots \cdots (5)$$

where σ_i and $\left(\dfrac{d\phi}{dx}\right)$ represent the electrical conductivity by i particles and electric field strength, respectively. Substitu-
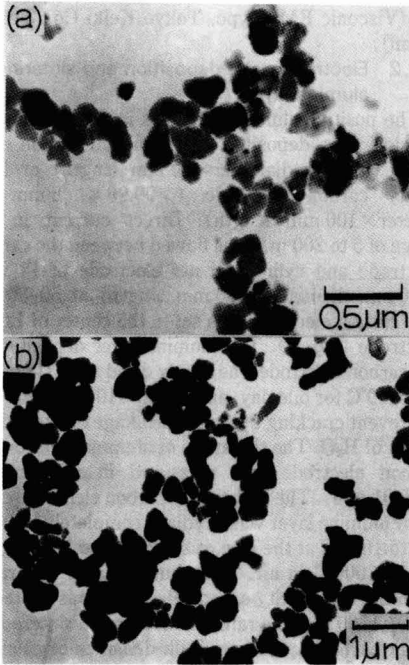
Fig. 1. Transmission electron micrographs of α-Al₂O₃ powders with the average diameters of 0.2 (a, powder A) and 0.6µm (b, powder B).

tion of Eq. (5) into Eq. (4) yields Eq. (6).

$$w = \frac{C_i}{n_i(Z_ie)} \sigma_i \left(\frac{d\phi}{dx}\right) t \quad \ldots \ldots \ldots (6)$$

Electrical conductivity is also defined by Eq. (7),[20]

$$\sigma_i = n_i(Z_ie) B''_i \quad \ldots \ldots \ldots \ldots \ldots (7)$$

where B''_i is the electrical mobility of i particles which is related to the drift velocity (V_i) of charged particles by Eq. (8).[21]

$$B''_i = \frac{V_i}{\left(\frac{d\phi}{dx}\right)} \quad \ldots \ldots \ldots \ldots \ldots (8)$$

The drift velocity of spherical i particle in the suspension is expressed by Eq. (9),[22]

$$V_i = \frac{2}{3} \frac{\varepsilon_o \varepsilon_r \zeta}{\eta} \left(\frac{d\phi}{dx}\right) \quad \ldots \ldots \ldots \ldots (9)$$

where
ε_o = the permitivity of vacuum
ε_r = the relative dielectric constant of liquid media
ζ = the zeta potential of charged particles i
η = the viscosity of suspension.
Substitution of Eqs. (7)–(9) into Eq. (6) gives Eq. (10).

$$w = C_i B''_i \left(\frac{d\phi}{dx}\right) t = C_i V_i t$$

$$= \frac{2}{3} C_i \varepsilon_o \varepsilon_r \zeta \frac{1}{\eta} \left(\frac{d\phi}{dx}\right) t$$

$$= \frac{2}{3} C_i \varepsilon_o \varepsilon_r \zeta \frac{1}{\eta} \frac{E}{L} t \quad \ldots \ldots \ldots \ldots (10)$$

where E and L are the applied voltage and distance between electrodes, respectively. Equation (10) indicates that the deposition weight of charged particles depends on four important parameters; (i) the surface property of colloidal particles (zeta potential), (ii) the electrical property of liquid media (relative dielectric constant), (iii) properties of the colloidal suspensions (solid content and viscosity) and (iv) applied voltage and time. In this experiment, the deposition characteristic of charged alumina particles and the properties of the formed alumina layer were investigated.

3. Experimental Procedures

3.1. Properties of Aqueous Alumina Suspensions

Two kinds of high purity α-alumina powders (>99.99%) of the average diameters of 0.2 (powder A) and 0.6µm (powder B) (Sumitomo Chemical Co. Ltd.) were used in the experiment (**Fig.1**). Zeta potential of the colloidal alumina particles in the dilute suspension (0.02wt%) was measured as a function of pH using a zeta meter (Zeta-Meter Inc., U.S.A.). In pH adjustment, HCl and NH₄OH solutions were used. **Figure 2** shows the zeta potential of colloidal alumina particles as a function of pH. The isoelectric points for both powders were in the pH range of 7 to 8. Electrophoretic deposition was done with the aqueous suspensions at pH 2.5 where positively charged alumina particles were well dispersed due to the strong repulsion force among highly charged particles.[6,23] The alumina suspensions were prepared at the concentrations of 1 to 20vol% at pH 2.5. After the suspensions were stirred by magnetic stirrers for 24hrs, ultrasonic vibration (20kHz) was applied for 5min to facilitate the powder agglomerates. The viscosities of alumina suspensions were determined by a cone and plate viscometer (Visconic EMD type, Tokyo Keiki Co., Tokyo, Japan).

3.2. Electrophoretic Deposition and Sintering of Alumina Layer

The positive alumina particles in the stirred suspension were deposited on the pencil carbon electrode (0.5mm diameter×60mm length) or high purity carbon electrode (>99.99%, 5mm diameter×100mm length). Direct current in the range of 5 to 200mA was applied between the carbon

Fig. 2. Zeta potential of the colloidal α-Al₂O₃ particles (powders A and B) as a function of pH.

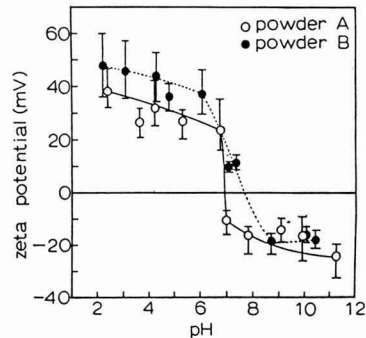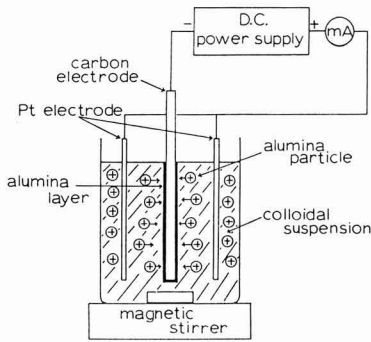**Fig. 3.** Electrophoretic apparatus with carbon and platinum electrodes.

diameter ×500mm length) at 50–300V. The carbon electrode was set in the center of the Pt net electrode (**Fig.3**). The alumina layer deposited on the carbon electrode was slowly dried at 10°C for two days, 50°C for one day, and finally 110°C for one day to prevent cracking by rapid shrinkage due to evaporation of H_2O. The alumina layer thickness on the carbon electrode was measured in micrometers (±0.01mm). The high purity carbon electrode coated by alumina layer was oxidized completely by heating to 1000°C at the rate of 2°C/min and keeping for 2hrs at 1000°C in air. The alumina layer separated from the high purity carbon electrode was heated to 1100°–1500°C at the rate of 7°C/min and sintered for 1hr at each temperature. Bulk densities of calcined and sintered alumina layer were measured by the Archimedes method using distilled water. The sintered alumina layer was polished with diamond paste of 0.25μm and thermally etched at 100°C lower than the sintering temperature for 1hr to observe microstructures by a scanning electron microscopy (H-7010A type, Hitachi Co., Tokyo, Japan).

4. Experimental Results and Discussion

4.1. Electrophoretic Deposition of Alumina Particles

The alumina suspension with concentration below 15vol% behaved as a Newtonian liquid, showing a linear relation passing the origin of shear rate and shear stress. **Figure 4** illustrates the weight of alumina layer as a function of deposition time for the suspension of powder A of 15vol% at pH 2.5. As predicted by Eq. (10), the weight of alumina layer increased linearly with time. A good linear relation between applied voltage and the weight of alumina layer was also confirmed on the data shown in Fig.4, which was in accordance with the theoretical prediction by Eq. (10). However, a small decrease in the deposition rate of alumina particles was observed at 50 and 100V after 90 and 120sec of deposition time, respectively. The above results suggest that the shield effect of deposited alumina layer on the following electrophoretic deposition was small at high voltage. The deposition rate of alumina layer shown in Fig.4 was compared with one calculated by Eq. (10). In the calculation the following values were substituted for the parameters in Eq. (10): ζ=40.0mV, C_i=0.586g/cm,³ η=3.63mPa · sec. The ratio of measured deposition ρατε (κ(εξπ.)) το χαλχυλατεδ δεποσιτιον ρατε (κ(χαλ.)) (δε-ποσιτιον εφφιχιενχψ=κ(εξπ.)/κ(χαλ.)) ωασ ιν τηε ρανγε οφ 0.13 το 0.15 ατ 50–300V. This low deposition effi-

ciency may be due to the formation of H_2 gas by the electrolysis of acidic media (pH=2.5) or the leakage of ion current by the charged alumina particles. A postulated relation between the low deposition efficiency and the H_2 gas formation implies an equivalent parallel circuit consisting of resistance Rh and Ra, which are related to H ions and positively charged alumina particles, respectively. The deposition efficiency of 0.13–0.15 means that Ra is 6 to 7 times as great as Rh. In other words, effective particle concentration in Eq. (10) results in 13–15% of the concentration of alumina suspension.

4.2. Thickness and Density of the Alumina Layer

Figure 5 shows the change in thickness of alumina layer (powder A) as a function of deposition time. The alumina layer grew with periodicity as seen in Fig.5. This result was compared with the calculated thickness of alumina layer. The volume (V) and weight (W) of alumina layer with the thickness Δr, deposited on the carbon electrode with the radius r and length h, are approximated by Eqs. (11) and (12), respectively,

$$V = h\pi \left\{ (r + \Delta r)^2 - r^2 \right\}$$
$$= h\pi (\Delta r^2 + 2r\Delta r) \quad \ldots\ldots\ldots\ldots\ldots (11)$$

$$W = w2\pi rh = 2k\pi rht \quad \ldots\ldots\ldots\ldots (12)$$

where w and k are the weight and deposition rate of alumina particles per unit area of electrode (see Eq. (10)). The bulk density (ρ) of alumina layer is defined by Eq. (13).

$$\rho = \frac{W}{V} = \frac{2k\pi\, rht}{\pi h\, (\Delta r^2 + 2r\Delta r)} = \frac{2krt}{\Delta r^2 + 2r\Delta r} \quad \ldots (13)$$
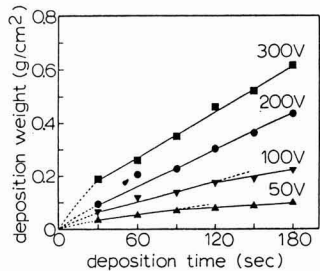

Fig. 4. The weight of alumina layer formed by electrophoretic deposition of the alumina suspension (powder A) of 15vol% at pH 2.5.
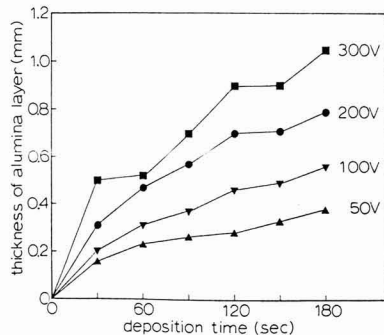

Fig. 5. Thickness of the alumina layer (powder A) as a function of deposition time.

Equation (13) is transformed to Eq. (14), and the solution about Δr of Eq. (14) is expressed by Eq. (15).

$$\rho\, r^2 + 2\, \rho\, r\, \Delta r - 2krt = 0 \quad\ldots\ldots\ldots (14)$$

$$\Delta r = r\, (\sqrt{1 + \frac{2kt}{\rho r}} - 1) \quad\ldots\ldots\ldots (15)$$

Equation (15) indicates that the thickness of alumina layer becomes bigger for a lower density layer formed at a higher deposition rate. **Figure 6** illustrates the comparison between calculated and measured thickness of alumina layer as a function of deposition time. In the calculation of Eq. (15), the deposition rate k was determined from the slope of lines in Fig.4. Figure 6 suggests that porous alumina layer was formed at early deposition time and grew densely with time.

The periodical increase of density and thickness of alumina layer can be understood from Eq. (16).

$$W = 2k\, \pi\, rht = \rho\pi\, h\, (\Delta r^2 + 2r\, \Delta r) \quad\ldots\ldots (16)$$

The weight increase of alumina layer which is directly proportional to deposition time, leads to density increase and/or increase in thickness of alumina layer. A large contribution of density increase to weight increase implies a small increase in the alumina layer thickness. The opposite case corresponds to a large increase in thickness under a constant
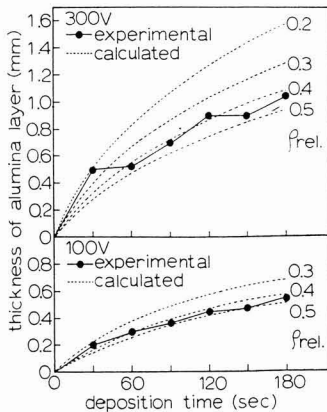
Fig. 6. Comparison between calculated and measured thickness of the alumina layer (powder A) as a function of deposition time at 100 and 300V. The $\rho_{rel.}$ indicates the relative density of alumina layer used in the calculation.
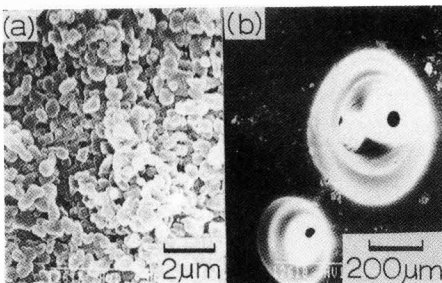
Fig. 7. Microstructure of the alumina layer (powder B) formed by electrophoretic deposition at 300V for 15min and calcined at 1000°C for 2hrs. The large pores (Fig.7(b)) were observed in the layer of densely packed alumina particles (Fig.7(a)).

density. The experimental results shown in Figs.5 and 6 suggest that alumina layer grows with alternative increase in density and thickness with deposition time.

4.3. Sintering Behavior of the Alumina Layer

Electrophoretic deposition of the alumina powder B at 200–300V for 10–20min provided the alumina layer with relative densities of 56 to 62%. The green density was higher for the layer formed at a higher voltage for a longer time. **Figure 7** shows the scanning electron micrographs of the alumina layer formed from colloidal particles with the average diameter of 0.6μm at 300V for 15min. Although the primary particles were densely packed (Fig.7(a)), large pores of diameters of 200 to 500μm (Fig.7(b)) were also produced. It is difficult to eliminate these large pores by sintering. Improvement in the processing of electrophoretic deposition of the acidic aqueous colloidal suspension is required to form a defect-free layer.

Figure 8 shows the density increase of alumina layer as a function of sintering temperature. A high density green layer formed at 300V was densified faster than the alumina layer formed at 200V. However, the densification rate was reduced above 1400°C. On the other hand, the green compacts formed by filtration of well-dispersed aqueous colloidal suspensions through gypsum molds gave higher density than those by electrophoretic deposition. As seen in Fig.8, the green compacts by filtration method were densified to full density at 1500°C. (The sintering data of alumina compacts by filtration method shown in Fig.8 were provided by Sumitomo Chemical Co. Ltd.) The above difference in densification behavior of the green compacts between electrophoretic deposition and filtration method suggests that large pores in the alumina layer (Fig.7) reduced the densification rate at high temperatures. Since the small pores are eliminated at lower temperatures more than large pores,[2,4,5,24,25] the large pores seen in Fig.7(b) would not affect the densification at low temperatures. **Figure 9** illustrates the microstructures of alumina layer sintered at 1500°C for 1hr. Although the density difference in sintered samples (a) and (b) shown in Fig.9 was small, the average grain size was larger for sample (b) (2.5μm) formed at 300V than sample (a) (1.7μm) formed at 200V. In addition, the pores in both samples were observed at the grain boundaries. These results suggest that grain growth rate was higher for the alumina layer with higher green density, and that pore
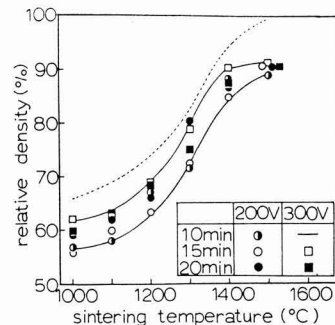
Fig. 8. Sintering behavior of the alumina layer (powder B) formed by electrophoretic deposition. The dotted line represents the sintering behavior of alumina compacts formed by filtration through gypsum molds. Sintering data on filtration method were provided by Sumitomo Chemical Co. Ltd.

Fig. 9. Microstructures of the alumina layer (powder B) sintered at 1500°C for 1hr. Samples (a) and (b) were formed by electrophoretic deposition at 200V for 15min and 300V for 15min, respectively.

coagulation occurred with grain growth.

5. Conclusions

Positively charged alumina particles in an acidic aqueous suspension of 15vol% solid were deposited on a cylindrical carbon electrode by direct current of 5-2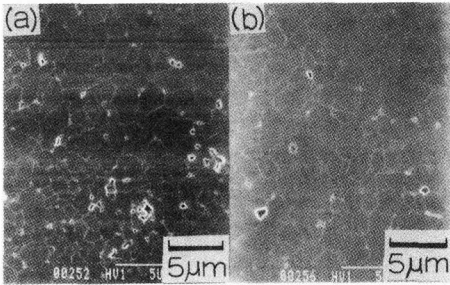00mA at 50-300V. The weight of alumina layer was proportional to the deposition time and the applied voltage. The deposition efficiency calculated from the deposition rate was in the range of 0.13 to 0.15. The density and thickness of alumina layer formed increased with periodicity as a function of deposition time. These phenomena were analyzed based on the theory of electrophoretic deposition and definition of density. The alumina layer with relative densities of 56-62%, formed from the alumina particles with the average diameter 0.6μm, was sintered at 1100°-1500°C in air. The densification rate was reduced above 1400°C by large pores (200-500μm).

Appendix

Forming of Alumina Layer by Alternative Current

Electrophoretic deposition of alumina particles (powder A) by alternative current at 6V (0.12, 1, and 10kHz) was investigated with the colloidal suspension of 15vol% at pH 2.5. **Figure A** shows the weight of alumina layer as a function of deposition time at a frequency of 10kHz. The weight of alumina layer increased in proportion to $t^{0.40}$ (t : deposition time). Under the alternative current, it is expected that diffusion process of alumina particles in the suspension dominates the deposition rate. This consideration predicts
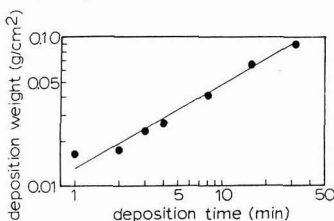
Fig. A. The weight of alumina layer (powder A) as a function of deposition time at AC (10kHz) of 6V. Alumina layer was formed from the suspension of 15vol% solid at pH 2.5.

that the weight of alumina layer increases in proportion to $t^{0.5}$. As shown in Fig.A, the experimental result was close to the diffusion-controlled process. However, no alumina particle was deposited on the carbon electrode at low frequencies of 120Hz and 1kHz. In the electrophoretic deposition by alternative current, high frequency is needed at low voltage. The properties of the alumina layer formed and further experiments are under investigation.

References:
1) F.F. Lange, J. Am. Ceram. Soc., 72, 3-15 (1989).
2) I.A. Aksay, in "Ceramics: Today and Tomorrow," Edited by S. Naka, N. Soga, and S. Kume, The Ceram. Soc. Japan (1986) pp.71-85.
3) L.M. Sheppard, Am. Ceram. Soc. Bull., 68, 979-985 (1989).
4) Y. Hirata and I.A. Aksay, in "Ceramic Microstructures '86: Role of Interfaces," Edited by J.A. Pask and A.G. Evans, Plenum Press (1987) pp.611-622.
5) Y. Hirata, I.A. Aksay, R. Kurita, S. Hori, and H. Kaji, in "Ceramic Transactions, Vol.6, Mullite and Mullite Matrix Composites," Edited by S. Sōmiya, R.F. Davis, and J.A. Pask, The Am. Ceram. Soc. (1990) pp.323-338.
6) Y. Hirata, S. Matsushita, S. Nakagama, Y. Ishihara, and S. Hori, J. Ceram. Soc. Japan, 97, 881-887 (1989).
7) Y. Hirata, I.A. Aksay, and R. Kikuchi, J. Ceram. Soc. Japan, 98, 126-135 (1990).
8) Y. Hirata, I. Haraguchi, and Y. Ishihara, J. Ceram. Soc. Japan, 98, 951-956 (1990).
9) R.W. Powers, Am. Ceram. Soc. Bull., 65, 1270-1277 (1986).
10) R.W. Powers, Am. Ceram. Soc. Bull., 65, 1277-1280 (1986).
11) S.N. Heavens, Br. Ceram. Proc., No.38, 119-126 (1986).
12) D.E. Clark, W.J. Dalzell, and D.C. Folz, Ceram. Eng. Sci. Proc., 9, 1111-1117 (1988).
13) T. Umegaki, K. Yamashita, and T. Kanazawa, Mem. Fac. Technol. Tokyo Metrop. Univ., No.38, 4003-4009 (1988).
14) T. Umegaki, Y. Hisano, K. Yamashita, and T. Kanazawa, Sekko to Sekkai, No.218, 24-28 (1989).
15) M. Era, S. Noge, T. Yamashita, and M. Takada, J. Ceram. Soc. Japan, 97, 1058-1064 (1989).
16) H.S. Maiti, S. Datta, and R.N. Basu, J. Am. Ceram. Soc., 72, 1733-1735 (1989).
17) N. Koura, Y. Mikuriya, and H. Shoji, Hyōmen, 27, 719-725 (1989).
18) N. Koura and Y. Mikuriya, Hyōmen Gigyutsu, 40, 819-824 (1989).
19) P.G. Shewmon, "Diffusion in Solids," McGraw-Hill Book Company (1963) p.141.
20) W.D. Kingery, H.K. Bowen, and D.R. Uhlmann, "Introduction to Ceramics, Second Edition," John Wiley & Sons (1976) p.848.
21) ibid., p.221.
22) H. Tamura and Y. Matsuda, "Gendai Denki Kagaku," Baihukan (1987) pp.92-94.
23) Y. Hirata, S. Nakagama, and Y. Ishihara, J. Ceram. Soc. Japan, 98, 316-321 (1990).
24) W.D. Kingery, H.K. Bowen, and D.R. Uhlman, "Introduction to Ceramics, Second Edition," John Wiley & Sons (1976) pp.448-515.
25) M.D. Sacks and J.A. Pask, J. Am. Ceram. Soc., 65, 70-77 (1982).

Fatigue Behavior of Tetragonal Zirconia Polycrystals Containing 4mol% Y_2O_3

Masahiro Ashizuka, Takeshi Honda and Yoshitaka Kubota*

Kyushu Institute of Technology, 1-1, Sensu-cho, Tobata-ku, Kitakyushu-shi 804, Japan

*Tosoh Corporation

2743-1, Hayakawa, Ayase-shi 252, Japan

Fracture stress (σ_f) of tetragonal zirconia ceramics containing 4mol% Y_2O_3 was measured as a function of stressing rate($\dot{\sigma}$) (dynamic fatigue). Linear relationships were obtained between log σ_f and log $\dot{\sigma}$ at room temperature. Crack growth parameters N obtained from the slopes of the linear relationships were 32 for grain size of 0.47μm(Z4Y-Ia), 33 for 0.16μm(Z4Y-Ic) and 46 for 1.34μm(Z4Y-II).

A linear relationship was observed between log σ_f and log $\dot{\sigma}$ for Z4Y-Ic at 250°C, and the N value was 41. log σ_f for Z4Y-II at 250°C was constant at stressing rates above 30.2MPa/s. The N value obtained for stressing rates below 3.02MPa/s was 8.7. The time to failure t_f under several applied stresses σ's measured for the specimen with a grain size of 2.34μm(Z4Y-II) at 250°C(static fatigue) was similar to the life time predicted from dynamic fatigue data. A linear relationship was observed between log t_f and log σ, and the N value obtained from the slope was 7.3.

[Received May 7, 1990; Accepted October 26, 1990]

1. Introduction

Yttria-containing tetragonal zirconia polycrystals (Y-TZP) is the material having the highest strength and toughness among ceramics. Its high strength, however, has only been evaluated over short time periods with a crosshead speed of about 0.5mm/min; there is no assurance that it can be maintained under a prolonged stress loading. It generally holds that when most ceramic materials are loaded for a long time with stresses lower than those reported as their strength values, they are fatigues due to the slow crack growth resulting in lowering of strength. By measuring the fatigue in TZP containing 2, 3 and 4mol% Y_2O_3 at room temperature and at 250°C, we discovered that not only the Y_2O_3 content, but also the grain size of specimens have a great effect on the fatigue of Y-TZP.[1-5] We also discovered that the monoclinic zirconia contents in the fracture surface decreases as the Y_2O_3 content decreases given a constant grain size; and decreases as the grain size decreases given a constant Y_2O_3 content. Furthermore, with 4mol% Y-TZP, the monoclinic ratio decreases to zero when the grain size is close to 0.5μm.[3] In our previous reports, measurements with 4-mol% Y_2O_3-TZP were carried out at room temperature and at 250°C for specimens with grain size of around

2μm, and at 250°C for specimens with grain size of around 0.5μm.[2,3] In the present study, we attempted to investigate the effect of grain size and phase transformation on the dynamic fatigue behavior of 4-mol% Y_2O_3-TZP by also measuring the fatigue of specimens with grain size of around 1μm at room temperature and at 250°C. Using the specimen having a grain size of about 0.5μm, we measured their dynamic fatigue to determine the grain size that would cause a phase transformation upon fracture, and to understand what effect such phase transformation would have on fatigue. Based on the present study and previously published data we attempted to ascertain the mechanism of Y-TZP fatigue. With some specimens we also measured static fatigue and compared the obtained data with life time estimated from measured values of dynamic fatigue.

2. Experimental Procedure

The specimens used in the present study were made by uniaxially pressing 4mol%Y_2O_3-containing zirconia powder prepared by a coprecipitation method, and then isostatically compacting at a pressure of 300MPa with a cold hydrostatic press. Their compacted specimens were sintered at 1400° to 1600°c in air (supplied by Tosoh Corporation). The average grain sizes of sintered body are three type of 0.47μm (Z4Y-Ia), 0.62μm (Z4Y-Ic) and 134μm (Z4Y-II). Specimen sizes were 3 by 4 by 40mm and their surfaces were ground with a #200 diamond grinding wheel. Dynamic fatigue was obtained by measuring, with a 30mm span 3-point bending fixture, variations in fracture stresses at various stressing rates. 8 samples were used for each crosshead speed.

Static fatigue was obtained by measuring the time until fracture under various constant stresses. The monoclinic ratios and the thickness of the transformation zone in the fracture surfaces were measured by a x-ray method.[6,7]

3. Results and Discussion

Regarding dynamic fatigue, following relationship exists between the stressing rate $\dot{\sigma}$ and the fracture stress σ_f.[8-10]

$$\sigma_f = B_2 \dot{\sigma}^{\frac{1}{N+1}} \quad \ldots \ldots \ldots \ldots \ldots \ldots (1)$$

$$\therefore \log \sigma_f = \log B_2 + \frac{1}{N+1} \log \dot{\sigma} \quad \ldots \ldots \ldots (2)$$

For static fatigue, the following relationship holds for the applied stress σ and the time to failure t_f:

Crosshead Speed (mm/min)
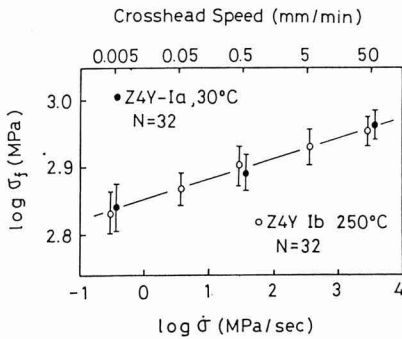
Fig. 1. Relation between fracture stress (σ_f) and stressing rate ($\dot{\sigma}$) for tetragonal zirconia polycrystals containing 4mol% Y_2O_3. Z4Y-Ia: Grain size of 0.47μm. Z4Y-IIb: Grain size of 0.56μm.

Crosshead Speed (mm/min)
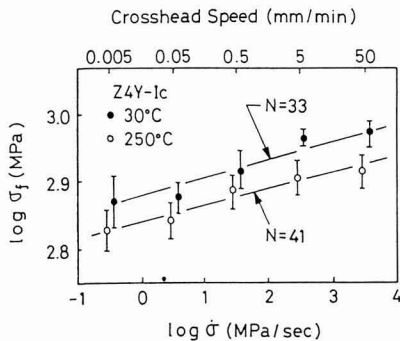
Fig. 2. Relation between fracture stress (σ_f) and stressing rate ($\dot{\sigma}$) for tetragonal zirconia polycrystals containing 4mol% Y_2O_3. Z4Y-Ic: Grain size of 0.62μm.

$$t_f = B_1 \sigma^{-N} \quad \ldots \ldots \ldots \ldots \ldots \ldots (3)$$

where represents the life time of the material continuously loaded with constant stress σ and N is a crack growth parameter. The larger is the N value, the smaller is the fatigue. B_1 in equation (3) and B_2 in equation (1) are related by in the following equation:

$$B_2^{N+1} = B_1 (N + 1) \quad \ldots \ldots \ldots \ldots \ldots (4)$$

Therefore, from the results of the measurement of dynamic fatigue, the life time of a material under a constant stress can be estimated.

3.1. Dynamic Fatigue

The dynamic fatigue of specimens having grain sizes of 0.47, 0.62 and 1.34μm was measured. The results are shown in **Fig.1 through 3**. Figure 1 also shows for comparison the results at 250°C for a sample with grain size of 0.56μm (Z4Y-Ib), previously reported.[3] As is evident from these figures, the log σ_f-log $\dot{\sigma}$ relationship at 30°C was linear. The values of the crack growth parameter N obtained from the gradients of the straight lines were 32 for Z4Y-Ia, 33 for Z4Y-Ic, and 46 for Z4Y-II. The log σ_f-log σ relationship at 250°C was linear for 4Y-Ib and Z4Y-Ic, and the values of N obtained from the gradients of the straight lines were 32 and 41, respectively. For Z4Y-II, with grain size above 1μm, the fracture stress increases as the stressing rate increased in the range below 3.02MPa/s (crosshead speed:

0.05mm/min), but it remained constant as the stressing rate increased over the range of 30.2 to 3.02×10^3MPa/s (crosshead speed 0.5 to 50mm/min). In the stressing rate range of 0.302 to 3.02MPa/s (crosshead speed: 0.005 to 0.05mm/min), the crack growth parameter N was calculated from the gradient as 8.7, and the specimens showed remarkable fatigue.

Using present results and previously reported data, we classified the specimens in terms of grain size into a 0.5μm group (grain size range: 0.46 to 0.62μm), a 1μm group (1.06 to 1.34μm) and a 2μm group (2.08μm) and plotted N values versus Y_2O_3 content as shown in **Fig.4**. At room temperature, grain size had no significant effect on N; as the Y_2O_3 content increased, the N values decreased but not below 32. On the other hand, at 250°C, fatigue was greatly affected by both grain size and Y_2O_3 content. For the 0.5μm group, at 3mol% Y_2O_3, the N values were about 50 showing small fatigue; at 4mol% Y_2O_3, values they were a
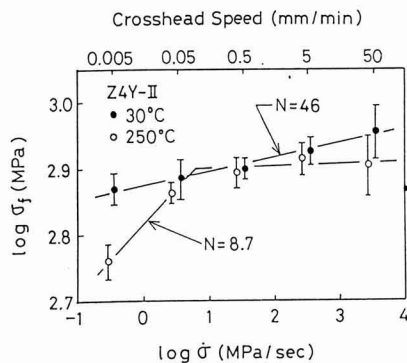
Crosshead Speed (mm/min)

Fig. 3. Relation between fracture stress (σ_f) and stressing rate ($\dot{\sigma}$) for tetragonal zirconia polycrystals containing 4mol% Y_2O_3. Z4Y-II: Grain size of 1.34μm.

| Grain	Temperature	
size	R.T.	250°C
0.5 μm	●	○
1 μm	■	□
2 μm	▲	△

Fig. 4. Relation between N values and Y_2O_3 contents for grain size groups of 0.5, 1.0 and 2.0μm. R.T.: Room temperature. C.S.: Grain size.

Fig. 5. Relation between monoclinic zirconia on the fracture surface and Y_2O_3 contents for grain size groups of 0.5, 1.0 and 2.0μm. R.T.: room temperature. G.S.: Grain size. The symbols in this figure are the same as those in Figure 4.

little lower: 32 to 41. At 2mol% Y_2O_3, the N values were much lower; about 22, and the fatigue was prominent. For grain sizes above 1μm, the N values were below 10 irrespective of Y_2O_3 content, and the fatigue was substantial.

Figure 5 shows monoclinic zirconia contents of the fracture surfaces after the measurement of dynamic fatigue. In the same manner as for Fig.4, the data was plotted versus Y_2O_3 concentration for the three groups of specimens. The monoclinic ratios decreased as Y_2O_3 content increased at a constant grain size, and increased as grain size increased at a constant Y_2O_3 content. This tendency of monoclinic ratios in fracture surfaces was consistant with that previously reported.[3]

Fracture stress σ_f at a stressing rate of 0.302MPa/s and crack growth parameter N are plotted as a function of the thickness of transformation zone in calculated from monoclinic zirconia contents in fracture surface in **Fig.6**. As is evident from Fig.6(a), the fracture stresses at room temperature increased asymptotically as $\sqrt{h}$ increased, increasing more rapidly in TZP specimens with a smaller grain size. Fracture stress σ_f at 250°C for specimens with a small grain size of 0.5μm, remained nearly constant in the h range below 0.063μm (monoclinic ratio: 4%) and gradually increased as h increased beyond the range. For the 1μm group, fracture stress σ_f did not increase as h increased, rather it rapidly decreased as h increased over 1μm.

As shown in Fig.6(b), N values of room temperature increased as h increased. At 250°C for the 0.5μm group, N values at h below 0.6μm increased with increasing h values, as they did at room temperature, but N values at h above 0.6μm rapidly decreased with increasing h values. By the comparison of (a) with (b) in Fig.6, in the case of 0.5μm group at 250°C, it is recognized that the N value at h f 1.2μm (Z2Y-I) rapidly decreased, whereas σ_f at the same h value asymptotically increased yet. That is, it is assumed that both figure do not entitly agree. However, a detailed examination of data for Z2Y-I reveals that the fracture stress at a crosshead speed of 0.005mm/min. was much lower than the values of crosshead speed of 0.5 or 50mm/min. In other words, Z2Y-I has already lost its strength at h of 1.2μm. This suggests that N vs $\sqrt{h}$ plots more effectively show the effect of the phase transformation on the loss of strength.

In our previous report, we plotted the results of fatigue

measurements on the coordinates of fracture stress σ_f and the square root of transformation zone thickness $\sqrt{h}$, and observed that if the strength values were in the flaw limited strength region a transformation from tetragonal to monoclinic (T→M transformation) acted as resistance to fatigue. Conversely, if the strength levels were in the transformation limited strength region, a T→M transform accelerated fatigue.[3] Reviewing the present data in Fig.6 in connection with the above observation reveals that the results obtained at room temperature were in the flaw limited strength region and the T→M transform acted against fatigue, causing N to increase as the thickness of the transformation zone (i.e., the magnitude of the transformation) increased. For the 0.5μm group, at 250°C, it is assumed that strength levels at h below about 0.6μm were in the flaw limited strength region, so that N increased with increasing h as it did at room temperature. For h greater than 0.6μm, strength levels were in the transformation limited strength region, so that N decreased as h increased. It is assumed that the intersection (point A in **Fig.7** in References[3]) in the relationship between σ_f and $\sqrt{h}$ and the relationship between σ_c (critical transformation stress) and $\sqrt{h}$ is nearer to the zero point of the coordinates in Fig.6 at 250°C than at room temperature; likewise it is nearer to the zero point for Y-TZP having a large grain size than with other specimens at a constant temperature of 250°C. In other words, it is assumed that the transformation limited strength region is more extended toward the zero point of the coordinates in Fig.6 at 250°C than at room temperature. Similarly the region is closer to the zero point for secimens with larger grain sizes at a constant temperature of 250°C. For Y-TZP with a grain size above 1μm at 250°C, it is assumed that strength levels were in the transformation limited strength region, thus N was small.

Fig. 6. (a) Relation between fracture stress σ_f and transformation zone size (h) for grain size groups of 0.5, 1.0 and 2.0μm. (b) Relation between N values and h for grain size groups of 0.5, 1.0 and 2.0μm.
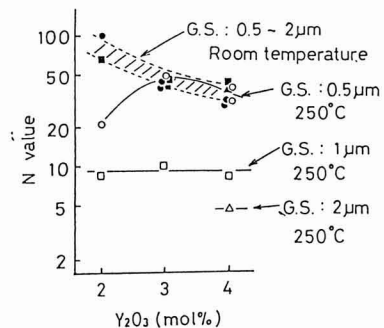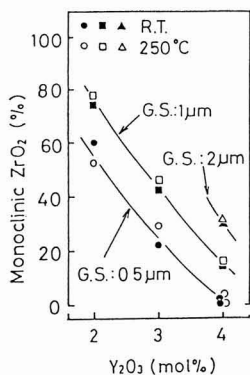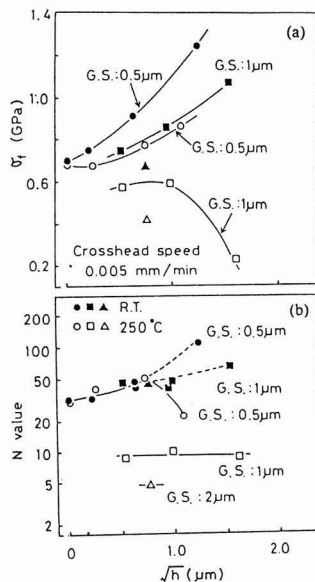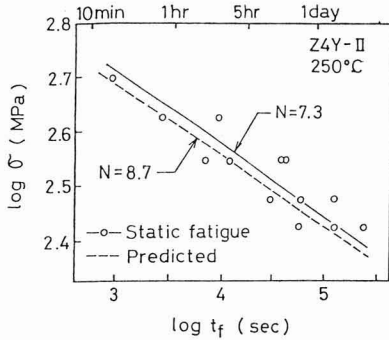R.T.: Room temperature. G.S.: Grain size. The symbols in this figure are the same as those in Figure 4.

Fig. 7. Relation between failure time (g$_f$) and applied stress (s) for tetragonal zirconia polycrystals containing 4mol% Y$_2$O$_3$(Z4Y-II) (static fatigue). The broken line represents the value predicted from dynamic fatigue data.

Fig. 8. Fracture surface of tetragonal zirconia polycrystals containing 4mol% Y$_2$O$_3$ (Z4Y-Ia) after dynamic fatigue test at 30°C. Stressing rate: 30.2MPa/s (crosshead speed: 0.5mm/min). The arrow mark shows the fracture origin.

3.2. Static Fatigue

Figure 7 show the measured static fatigue data for Z4Y-II at 250°C, plotting the applied stress σ versus duration time until fracture t_f. A linear relation between log σ and log t_f was observed. The crack growth parameter N=7.3 obtained from the gradient of the straight line was close to the value of N=8.7 obtained from the measurement of dynamic fatigue. Also, the material life time estimated from measured data on dynamic fatigue were very close to life time obtained in the measurement of static fatigue.

We had previously reported that the life time of 2 and 3mol% Y$_2$O$_3$-containing TZP measured by static fatigue technique were longer than the life time estimated from the data obtained by dynamic fatigue technique for 3mol% Y$_2$O$_3$-TZP and shorter than that for 2mol% Y$_2$O$_3$-TZP.[1,4] In the case of 3mol% Y$_2$O$_3$-TZP, this discrepancy may have been due to the phase transformation having a greater effect on the measurement of static fatigue than on the measurement of dynamic fatigue. It was also assumed that in the case of 2mol% Y$_2$O$_3$-TZP, thermal aging was additionally involved, causing the measured values to be lower than the estimated. On the other hand, for the specimens in the

present study, as for alumina ceramics,[10] the life time estimated from dynamic fatigue measurements were close to the measured valves from static fatigue data. This may be because compared with 3mol% Y$_3$O$_3$-TZP, a smaller transformation from tetragonal to monoclinic results in a smaller contribution of the phase transformation to fatigue as shown in Fig.5, and a greater contribution of stress corrosion becomes the main cause of fatigue such as slumina ceramics.

3.3. Observation of Fracture Surface

Figures 8 and 9 show fracture surfaces after the measurement of dynamic fatigue. Figure 8 shows one of Z4Y-Ia specimens after fatigue measurement at room temperature. It was similar to that of 3mol% Y$_2$O$_3$-TZP (Z3Y-I) at room temperature previously reported, and showed a mirror region near the fracture origin. Figure 9(a) shows a fracture surface of Z4Y-Ic at 250°C. It too, showed a mirror region near the fracture origin. Figure 9(b) shows one for Z4Y-II at 250°C. No discernable mirror region near the fracture origin was indicated. The size of the fatigue fractures surface of Y-TZP were related to the magnitude of phase transformation; those for 2mol% Y$_2$O$_3$-TZP (Z2Y-II) which had the most magnitude of phase transformation were large, while specimens of 3mol% Y$_2$O$_3$-TZP (Z3Y-I) which had a smaller phase transformation showed only small fatigue fractures surface near the fracture origin. Thus, in the present study for 4mol% Y$_2$O$_3$-TZP (Z4Y-II), it was assumed that magnitude of phase transformation was even lower, such that fatigue fractures surface were too small to be observed.

Figure 10 shows a fracture surface of Z4Y-II (mean grain
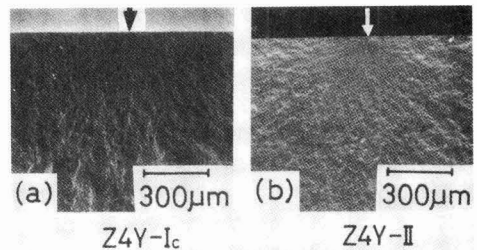
Fig. 9. Fracture surface of tetragonal zirconia polycrystals containing 4mol% Y$_2$O$_3$ (Z4Y-Ic and Z4Y-II) after dynamic fatigue test at 750°C.
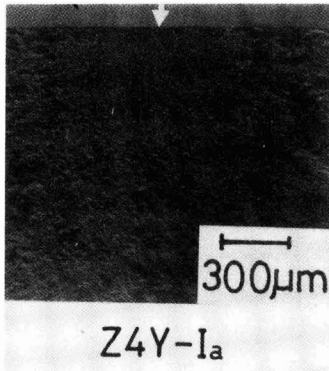Stressing rate: 0.302MPa/s (crosshead speed: 0.005mm/min).
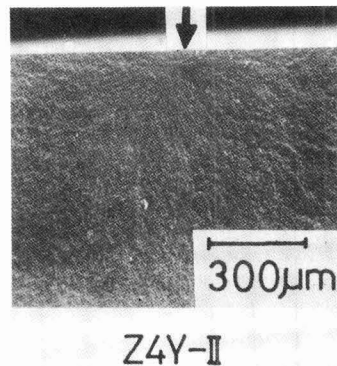
Fig. 10. Fracture surface of tetragonal zirconia polycrystals containing 4mol% Y$_2$O$_3$ (Z4Y-II) after static fatigue test at 250°C.

size: 1.34μm) after the measurement of static fatigue at 250°C. It is similar to the dynamic fatigue fracture surface shown in Fig.9(b). It did not show any pattern similar to that observed in the measurement of static fatigue of Z3Y-II (mean grain size: 1.06μm) at 250°C.[1]

4. Conclusions

Measuring the dynamic and static fatigues of 4mol% Y_2O_3-containing TZP specimens prepared by a pressureless sintering method, we obtained the following results:

1) A linear relationship was observed between log σ_f and log $\dot{\sigma}$ at room temperature. The values of the crack growth parameter N obtained from the gradient of the straight line, were 32, 33 and 46 for specimens with grain size: 0.47, 0.67 and 1.34μm, respectively.

2) At 250°C, the relationship between log σ_f and log $\dot{\sigma}$ was linear for grain size of 0.62μm; the crack growth parameter N was 41. For specimens having a grain size of 1.34μm, a linear relation was obtained in the stressing rate range ; 0.302 to 3.02MPa/s (crosshead speed range: 0.005 to 0.05mm/min), but the fracture stress remained constant as the stressing rate increased above 30.2MPa/s (crosshead speed; above 0.5mm/min). The value of the crack growth parameter N obtained from the gradient of the straight line in the stressing rate range below 3.02MPa/s was 8.7.

3) The life time obtained from static fatigue data for Y-TZP with grain size 1.34μm at 250°C were very close to the life time estimated from the results of measurement of dynamic fatigue. The log-log relationship between applied stress σ and time to failure t_f was linear, and the value of the crack growth parameter N was 7.3, which was close to 8.7, the value of N for dynamic fatigue.

References:
1) M. Ashizuka, H. Kiyohara, E. Ishida, M. Kuwabara and T. Tsukidate, Yogyo-Kyokai-Shi (J. Ceram. Soc. Japan), 94 (1986), 432-439.
2) M. Ashizuka, H. Kiyohara, M. Gondo and Y. Kubota, Yogyo-Kyoka-Shi (J. Ceram. Soc. Japan), 95 (1987), 387-393. Journal of the Ceramic Society of Japan, International Edition, 95 (1987), 348-353.
3) M. Ashizuka, H. Kiyohara, T. Okuno and Y. Kubota, Journal of the Ceramic Society of Japan, 96 (1988), 749-754. International Edition, 96 (1988), 731-736.
4) M. Ashizuka, H. Kiyohara, T. Okuno and Y. Kubota, Journal of the Ceramic Society of japan, 96 (1988), 820-824. International Edition, 96 (1988), 798-802.
5) M. Ashizuka and Y. Kubota, Journal of the Ceramic Society of Japan, 96, 1186-1191 (1988). International Edition, 96, 1157-1161 (1988).
6) H. Toraya, M. Yoshimura, and S. Somiya, J. Amer. Ceram. Soc., 67, (1984), C-119.
7) T. Kosmac. R. Wagner, and N. Claussen, J. Amer. Ceram. Soc., 64 (1981), C-72.
8) Mechanical Properties of Ceramics, Ceramic Society of Japan (1979).
9) H.C. Chandan, R.C. Bradt and G.E. Rindone, J. Amer. Ceram. Soc., 61 (1978), 207-210.
10) J.E. Ritter and J.N. Humenik, J. Mater. Sci., 14 (1979), 626-632.

Growth of Diamond Films by High-Speed Plasma CVD

Toyohiko Kobayashi and Shozo Ono

Fuji Research Laboratory, Tokai Carbon Co., Ltd.

394-1, Subashiri, Oyama-cho, Sunto-gun, 410-14 Japan

Using a radio-frequency (rf) thermal plasma torch with a water cooled nozzle, the diamond film was synthesized at the maximum rate of 880μm/h on a molybdenum substrate from CH_4 and H_2 at a torch pressure of 517 Torr. The deposition rate was studied as a function of following parameters: diameter of the nozzle (6 to 24 mm), diameter of the plasma torch (50 and 60 mm), plate power (44 to 81 KW), torch pressure (740 to 400 Torr), and CH_4/H_2 feed ratio (4 to 5%). The deposition rate increased with decreasing the nozzle diameter from 24 to 8 mm but decreased at 6 mm. The columnar-like films were obtained after one hour deposition with the nozzles of 12, 10, and 8 mm in diameter.

1. Introduction

Diamond is known for various favorable properties, in addition to its great hardness,such as high resistance to wear, thermal conductivity, resistance to chemicals and excellent semiconductor properties. Recently, a number of researchers have been extensively studying the vapor phase synthesis of diamond, in order to realize these favorable properties of diamond in thin films. With respect to the various synthetic processes, the thermal filament [1] and microwave plasma [2] processes have been attracting more attention than the others, because of their controllability, stability, reproducibility and productivity. Deposition rate of these processes, however, is generally low at approximately 0.5 to 1.0μm/h for a methane-hydrogen system and a variety of attempts have been made to increase the deposition rate. As a result, it has been increased by more than ten times by the use of methyl alcohol or acetone as the starting materials,[3] or by the use of an arc in the glow or arc transition regions.[4] In addition, thermal plasma may be used to speed up production. The deposition rate were 1 to 3μm/min for the radio-frequency thermal plasma[5] and DC plasma jet processes,[6,7] and 930 μm/h for the arc discharge plasma jet process.[8] It was believed that an arc or DC plasma provided higher optimum temperatures and energy densities than a radio-frequency plasma, which accounted for the former's higher deposition rates. The radio-frequency plasma process, though lower in deposition rate, produced a wider plasma flame, which was advantageous with respect to deposition quantity. In this study, the authors investigated whether the large deposition quantity available by use of radio-frequency plasma was convertible into a high-speed deposition rate. As a result, it was found that a diamond film possessing a maximum thickness of 960μm

was producible in a deposition time of 65mins, when a nozzle-equipped radio-frequency plasma torch[9,10] was used for a methane-hydrogen system. The effects of nozzle inner diameter, pressure, input power and feed rates of CH_4 and H_2 on deposition rate and quantity were clarified. Thus, it was considered that a high-speed diamond film deposition method had been established.

2. Experimental Procedure

2.1. Experimental Apparatus

The experimental apparatus consisted of a radio-frequency power source (4MHz, 100KW), reactor, gas supply and vacuum exhaust systems. The reactor consisted of a plasma torch, water-cooled substrate holder and chamber.

Fig.1 illustrates the plasma torch. It consisted of a water-cooled double tube of quartz, trebly wound radio-frequency coils, gas inlet nozzles at the top,and water-cooled copper nozzles at the bottom. In this study, two types of quartz double tubes (50 and 60mm I.D.) and five types of copper nozzles (6,8,10,12 and 24mm I.D.) were used.

The water-cooled substrate holder was provided with a vertically moving mechanism and sensor for substrate temperature (Accufiber Model 100). An optical sensor (1.27mm in diameter), connected to the external instrumentation system, was provided at the holder center, to measure temperature of the substrate back fitted into a disc-shape groove in the holder. Temperature thus measured was regarded as substrate temperature. The substrate consisted of molybdenum, 40mm in diameter and 3mm thick, polished
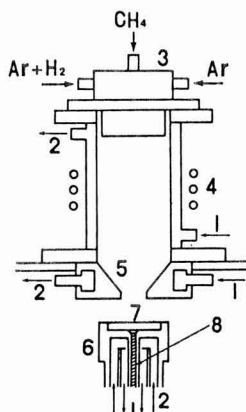

Fig. 1. Schematic view of the rf plasma torch: (1) cooling water inlet, (2) cooling water outlet, (3) gas supply, (4) induction coil, (5) nozzle, (6) substrate holder, (7)substrate, and (8) optical sensor.

by diamond paste of 10 μm in average particle size.

2.2. Experimental Procedure

The following plasma generation and deposition proce-
dures were adopted:
1) The torch and chamber were evacuated and purged with
   Ar gas and the plasma in the torch was ignited under a
   vacuum by radio-frequency electric power.
2) Applied power level was increased, while the sheath gas
   (Ar + H_2)and plasma gas (Ar) were introduced into the
   system, in order to set desired levels of gases and power.
   At the same time, the valves in the exhaust system were
   manipulated to regulate pressure within the torch or
   chamber.
3) The water-cooled substrate holder, situated immediately
   beneath the plasma torch, was moved upward, in order
   to set the temperature of the substrate.
4) Then, CH_4 was introduced into the torch from the top, in
   order to deposit the diamond film on the substrate.

In each run, nozzle-substrate distance and flow rates of
Ar and H_2 were set constant and torch inner diameter D_t,
nozzle inner diameter D_n, plasma torch inside pressure P_t
and chamber inside pressure P_c, pressure differential P_t-P_c,
power input, and CH_4 flow rate were varied in order to
follow their effects on deposition rate. The maximum thick-
ness at the film center was measured by a micrometer after
1h deposition time had elapsed and deposition rate was
determined.

The measurement error was ±10μm at the maximum,
which corresponded to approximately ±0.2μm/min with
respect to the deposition rate.

The diamond film thus produced was analyzed by Raman
spectroscopy.

Table 1 shows the typical experimental results. The at-
mospheric pressure for all the experimental runs was
700Torr (the experimental site was at 700m above the sea).

3. Results

The first run recorded a deposition rate of 14.6 μm/min
for the 960μm thick max. thickness film under the condi-
tions of Dt =50mm as torch inner diameter, Dt=8mm as

nozzle inner diameter, 65min as deposition time. No im-
provement in deposition rate was observed by increasing Dt
to 60mm and by increasing the input power.

3.1. Effects of Nozzle Inner Diameter Dn on Deposition Rate

Figure 2 shows the effects of nozzle inner diameter on
deposition rate for the conditions of Dt=50mm and
Pt=585±5Torr. The data marked withO's and Δ's was for
CH_4 flow rates of 0.16 and 0.20l/min, respectively. H_2 flow
rate and input power were set constant at 4.0l/min and
44KW. As shown, deposition rate increased as nozzle inner
diameter decreased to between 9.2 to 10μm/min at
Dn=8mm. Decreasing the inner diameter further to
Dn=6mm, however, decreased deposition rate to
4.5μm/min. **Figure 3** shows the results for the conditions
of Dn=60mm and input power of 68KW. Deposition rate
increased as nozzle inner diameter decreased, to
11.7μm/min at Dn=8mm.

3.2. Effects of Pressure on Deposition Rate

Figure 4 shows the effects of pressure on deposition rate,
under the conditions of Dt=50mm, Dn=8mm, CH_4 flow
rate=0.16l/min, H_2 flow rate =4.0l/min and input power
=44KW, where torch inside pressure Pt was varied in a
range from 400 to 740Torr (pressure differential between the
torch and chamber, Pt -Pc was varied from 110 to 40Torr).
The data marked with O's and ●'s was for the effects of Pt
on the deposition rate and conversion, respectively, while
those marked with Δ's related to the effects of pressure dif-
ferential Pt -Pc on deposition rate. The same numeral was
used for the same torch inside pressure. Increasing Pt in-
creased deposition rate linearly, from 6.7μm/min at
Pt=400Torr to 10.7μm/min at Pt=740Torr.

3.3. Effects of CH₄ Flow Rate and Input Power on

Table 1. Experimental conditions

Dt (mm)	Power (KW)	Reactants (l/min) H2	Reactants CH4	Dn (mm)	Pressure (Torr) Pt	Pressure Pc	Substrate temp.(°C)	L (mm)
50	44	4	0.16	24	400	300	800 – 830	8 – 13
			0.20	12	↑	↑		
				8	↓	↓		
				6	770	702		
	63	8	0.32	8	585	517	810 – 830	13
60	68	8	0.32	24	720	705	830 – 850	30 – 35
				12	↑	↑		
				10	↓	↓		
				8	740	710		
	81	8	0.32	8	635	537	840 – 850	30

Atmospheric pressure = 700 Torr
Dt : Torch inner diameter,   Dn : Nozzle inner diameter
Pt : Torch pressure,   Pc : Chamber pressure
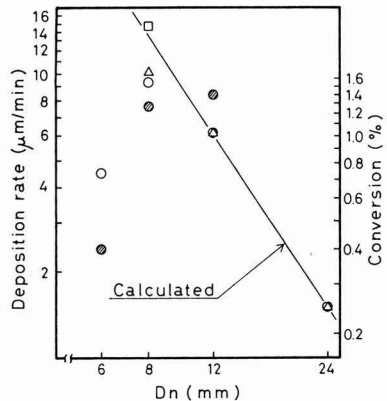L : Distance from the nozzle tip to the substrate

Fig. 2. The deposition rate and conversion rate as a function of the
nozzle diameter (D_n) with the torch of 50 mm diameter at the torch
pressure of 585±5 Torr.

	deposition	conversion
CH_4 0.16, H_2 4.0l/min, 44KW	O	◩
CH_4 0.20, H_2 4.0l/min, 44KW	Δ	
CH_4 0.32, H_2 8.0l/min, 63KW	❑	

Deposition Rate

No significant change in deposition rate was observed in a CH_4 flow rate range from 0.16 to 0.20l/min (CH_4/H_2 ratio: 4.0 to 5.0%) under the conditions of Dt=50mm, H_2 flow rate =4.0l/min and input power =44KW.

Next, input power was increased with Dt kept at 50mm, in order to investigate the effects of input power on deposition rate. Increasing input power at a constant gas flow rate would increase plasma diameter, which might melt and damage the quartz tube. Increased input power, therefore, was accompanied by increased H_2 flow rate and decreased the plasma diameter by thermal pinch effects and thereby prevented the above troubles. Increasing input power from 44 to 63KW increased deposition rate from 9.2 to 14.8μm/min, where Dt and Dn were set constant at 50 and 8mm, and H_2 and CH_4 flow rates were increased to 8.0 and 0.32l/min, respectively, in order to keep CH_4/H_2 ratio at 4%. Next, torch diameter was increased to 60mm and input power was increased, while H_2 and CH_4 flow rates were kept at 8.0 and 0.32l/min and input power at 68KW. However, it was found that the deposition rate under the conditions D_t=60mm and D_n=8mm was about 20% higher than that under D_t=50mm, D_n=8mm and input power=44KW, as discussed in Subsection 3.1, with the other conditions remaining essentially unchanged.

However, increasing input power to 81KW under Dt=60mm, Dn=8mm and the same gas flow rates as above decreased the deposition rate to 9.5mm/min. Since the results for Dt=50mm showd the tendency of the deposition rate to increase when the pressure inside the chamber was high, this pressure was set at the atmosphenic pressure without conducting differential exhaust when deposition was carried out under the condition Dt=60mm. In the case of 81KW as input power, the differential exhaust system was used to keep the pressure inside the chamber at 537Torr, hence, this increased torch inside pressure disturbed the conditions at the upper portion of the plasma.

3.4. Conversion and Deposited Quantity

Conversion was determined by the formula: Conver-
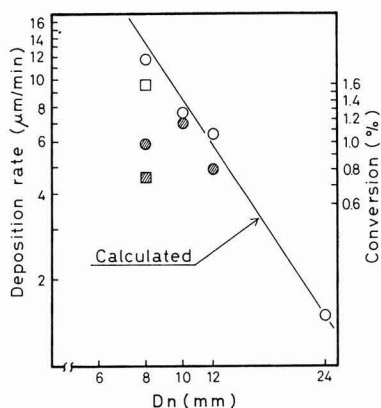
Fig. 3. The deposition rate and conversion rate as a function of the nozzle diameter (D_n) with the torch of 60 mm diameter at the chamber pressure of 700 Torr.

	deposition	conversion
68KW, Pt-Pc=15~50 Torr	○	◐
81KW, Pt-Pc=98 Torr	□	◩
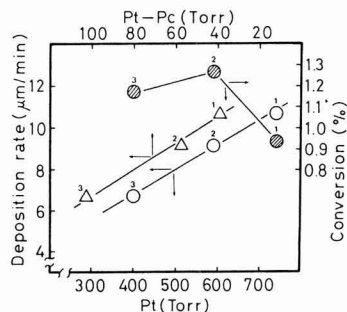
Fig. 4. The deposition rate and conversion rate as functions of the torch pressure (P_t) and the differential pressure (P_t–P_c) with 50 mm diameter torch and 8 mm diameter nozzle.
○,△: deposition rate, ◐: conversion rate.

sion(%) =Deposited Quantity (g)/(12(g) × CH_4 Flow Rate (l/min) × Deposition Time (min)/22.4 (l))× 100. This gave the conversion level of 0.4% with respect to Dt=50mm and Dn=6mm. The deposited quantity was 0.015g. Part of the conversion data for Dn=8,10 and 12mm are shown in Figures 2,3 and 4; the conversion levels for Dt=50 and 60mm were almost the same at approximately 1%, with the deposited quantities of approximately 0.05 and 0.1g, respectively.

3.5. Deposit Morphologies

The crystalline faces of the films deposited over the substrates were characterized by the (111) plane at the peripheral portion and by the (100) plane at the center. The multiple twins were found at the central portion. It was also observed that the (100) plane, though running in parallel to the substrate surface at the peripheral portion, became slanted to the surface as it moved towards the center, around which a new (100) plane was produced opposite to the slanted (100) plane. Furthermore, a triangular face was observed in the crystal possessing these two planes. The (100) plane increased in quantity, relative to the (111) plane, as CH_4/H_2 ratio increased; it was detected in only a small quantity at a ratio of 2% but covered almost the entire film surface at a ratio of 5%.

Of the films prepared in this study, only those by a 24mm diameter nozzle possessed uniform structures, the remainder were characterized by columnar structures, as shown in **Fig.5**. **Figure 6** presents the Raman spectral analysis results.

4. Discussion

4.1. Deposition Rate

Deposition rate increased as nozzle size decreased. This phenomenon may be explained by the reduced plasma space, resulting from use of a nozzle smaller in diameter than the torch, in order to increase density of the active species involved in the formation of the diamond films. Deposition rate Rd at a reduced nozzle area was estimated from the relationship of Rd=1.5×(24/Dn)², using the value of Rd=1.5μm/min at a nozzle inner diameter of Dn=24mm. The results are shown in Figures 2 and 3 (solid lines). As shown, the observed deposition rates were much lower than the calculated ones at Dn=8 and 6mm, for Dt=50mm(**Fig.2**). For those marked with ○'s and △'s, the data at a constant

torch inside pressure of Pt=585±5Torr, the differential pressure Pt-Pc increased as nozzle inner diameter Dn; 52 - 57Torr at Dn=8mm and 181 -244Torr at Dn=6mm. Decreased deposition rates with increasing differential pressure were probably attributed to the increased adiabatic cooling effects, which, in turn, decreased plasma temperature and densities of the reactive species. Deposition rate at a torch inner diameter Dt=60mm (marked with O's in Figure 3) was closer to the calculated value than that at Dt=50mm. As for the effects of pressure, pressure differential Pt - Pc was 15 to 30 Torr at Dt=60mm, which was lower than that at Dt=50mm. Decreasing pressure differential prevented decline of the deposition rates, making them closer to the calculated levels.

Increasing input power under the conditions of Dt=50mm and Dn=8mm increased deposition rate from 9.2 to 14.8μm/min, but decreased from 11.7 to 9.5μm/min under the conditions of Dt=60mm and Dn=8mm. These runs were performed, as discussed earlier, under the differential exhaust conditions, on account of the limitations set on the experimental parameters, as a result of which torch inside pressure Pt and differential pressure Pt -Pc varied from 755 and 49Torr to 635 and 98Torr, respectively, by increasing input power. These varied pressure conditions might have offset the effects of increased input power and decreased the deposition rates. Therefore, the effects of varied pressure conditions on the temperature decrease of the plasma gas emerging from the nozzle were estimated, where gas temperature immediately above the nozzle was assumed to be 6000K, based on the numerically determined temperature distributions in radio-frequency plasma torches[11-15] and the limitations set by the gas rate data.[16] The following equation was used to estimate temperature decrease by the adiabatic cooling effects, where Ar+H$_2$ plasma was regarded as an ideal gas and adiabatic coefficient as (γ=1.66) at a gas temperature of 6000K:

Fig. 5. Examples of the scanning electron micrographs for the diamond deposited. D$_t$=50 mm, D$_n$=12 mm, CH$_4$=0.16l/min, H$_2$=4.0l/min, Power supply=44KW, and P$_t$=580 Torr.
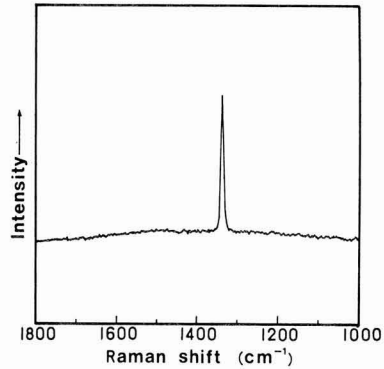
Fig. 6. Raman spectra of the diamond deposited. D$_t$=50 mm, D$_n$=12 mm, CH$_4$=0.16l/min, H$_2$=4.0l/min, 44KW, and P$_t$=580 Torr.

$$T_c = T_t \times \left(\frac{P_t}{P_c}\right)^{\frac{1-\gamma}{\gamma}}$$

where,

Tc: temperature of the plasma gas immediately below the nozzle (K)

Tt: temperature of the plasma gas immediately above the nozzle (K)

Pc: pressure in the chamber (Torr)

Pt: pressure in the torch (Torr)

The above equation gave the temperature decrease estimates of 6 to 7% at a torch inside pressure of Pt=700 to 600Torr and at a pressure differential of Pt-Pc=100Torr, and 13 to 15% at the same torch inside pressure and Pt-Pc=200Torr.

Referring to the relationship between conversion and deposition rate (Figure 4), decreased deposition rates were not always accompanied by decreased conversions. Two reasons were cited for decreased deposition rates: 1) Deposition area was found to increase as pressure differential increased. It was therefore considered that the increasing pressure differential might have changed the shape of the plasma flame hitting the substrate and the inside temperature distribution, causing the film thickness distribution over the substrate to vary from an uneven one with thickness much higher at the center than at the peripheral portions to a relatively flat one with higher thickness as a whole consequently, decrease the apparent deposition rate, although the quantity deposited remained essentially unchanged, and (2) Decreased temperature of the gases decreased deposited quantity, hence, substantial deposition rate. It was considered that decreases in deposition rate were controlled by variation in the film thickness distribution, when the pressure differential was substantially small and was determined more by decrease in the gas temperature as pressure differential increased.

Torch inner diameters of Dt=50 and 60mm gave almost the same conversion of approximately 1% and deposition rate, though deposited different quantities of 0.05 and 0.10g. Difference in substrate temperature was mainly attributed to the difference in plasma temperature under the same substrate cooling conditions. Substrate-nozzle distances were approximately 10mm at a torch inner diameter of Dt=50mm, and 28mm at Dt=60mm. The same substrate temperature in spite of different substrate-nozzle distance meant that the
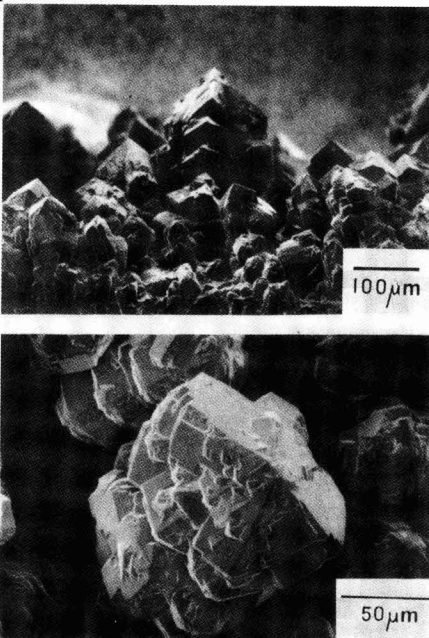
plasma temperature was the same in these cases. Assuming that deposition rate was determined by plasma temperature, any difference in the deposition quantity was due to difference in temperature distribution caused by difference in nozzle-substrate distance and by differences in deposit shape and deposition area caused by differences in temperature distribution and flame size.

In an arc discharge, decrease in arc column size meant an increase in plasma temperature. This phenomenon was known as the thermal pinch effect. It can be used to increase temperature at the arc center in a plasma jet or arc, by providing a relevant device, such as water-cooling nozzle, around the arc column to increase heat losses from the arc column sides.[17]

The same effect can be expected to occur around the water-cooling copper nozzle provided at the torch bottom, and, hence, the increased deposition rate was partly due to increased plasma temperatures.

## 4.2 Deposit Morphologies

The predominant crystalline plane changed from the (111) to (100) plane, as the CH_4/H_2 ratio increased and this phenomenon was also observed in the microwave plasma system.[18] The plane transfer in the thermal plasma system, however, tended to occur at a higher CH_4/H_2 ratio, conceivably due to its higher temperature. Some researchers have discussed that increasing substrate temperature at a constant CH_4/H_2 ratio grows the (111) plane preferentially over the (100) plane, with the result that the (100) plane was formed more at a higher temperature.[19,20]

There was a notable temperature distribution within the plasma flame produced in this study, with the substrate temperature much higher at the center than the peripheral portions. The transition from the (111) to (100) plane in the direction from the peripheral portions to the center, observed in this study, was in agreement with the above discussions,[19,20] when taking into account the temperature distribution over the substrate. It should be noted, however, that a triangle plane was found in the crystal possessing the two (100) planes. This was inconsistent with the above discussions, because it meant that the (111) plane appeared at a higher temperature side, when the triangle plane was regarded as the (111) plane, i.e., regarding the crystal as the Cubo-octahedron or part of the twin of the Cubo-octahedron (when diamond crystal was deposited on a substrate, it was divided by the substrate surface). A more detailed discussion required further investigations of the deposit morphologies.

5. Conclusions

Use of a nozzle-equipped, radio-frequency torch enabled high-speed deposition of a diamond film. The effects of nozzle inner diameter, pressure, input power, and CH_4 and H_2 flow rates on deposition rate and deposited quantity were investigated.
1) The film of columnar crystal, possessing the maximum thickness of 960μm, was produced in a deposition time of 65min.
2) Deposition rate increased as nozzle inner diameter decreased to a certain level, below which the opposite

phenomenon was observed, because of increased pressure differential accompanying decreased nozzle diameter.
3) Deposition rate decreased in two ways; one was an apparently not accompanied by decreased deposited quantity, and the other accompanied by the decreased deposited quantity, conceivably resulting from the adiabatic cooling effects.
4) Deposited quantity was essentially constant, irrespective of deposition rate, at a pressure differential of 100Torr or less.

References:
1) S. Matsumoto, Y. Sato, M. Kamo, and N. Setada, Jpn. J.Appl. Phys., 21,L183-L185 (1982).
2) M. Kamo, Y. Sato, S. Matsumoto, and N. Setaka, J. Cryst. Growth, 62, 642-644 (1983).
3) Y. Hirose and Y. Terasawa, Jpn. J. Appl. Phys., 25,L519-L521 (1986)
4) K. Suzuki, A. Sawabe, H. Yasuda, and T. Inuzuka, Appl. Phys. Lett., 50,728-729 (1987).
5) S. Matsumoto, N. Hino, and T. Kobayashi, Appl. Phys. Lett., 51, 737-739 (1987).
6) K. Kurihara, K. Sasaki, M. Kawarada, and N. Koshino, Appl. Phys. Lett., 52, 437-438 (1988).
7) M. Kawarada, K. Kurihara, K. Sasaki and N. Koshino, 2nd. Diamond Symposium Proceedings, 13-14 (1987)
8) S. Matsumoto, T. Kobayashi, M. Hino and Y. Moriyoshi, 34th Applied Physics Symposium Proceedings, 351 (1987)
9) H. Murakami, A. Nagai, T. Irokawa, T. Yoshida and K. Akashi, Seramikkusu Ronbun-shi, 97, 49-55, (1989)
10) N.Ohtake and M.Yoshikawa, NEW DIAMOND,No. 3, 38-39 (1989)
11) T. Yoshida, K. Nadagawa, T. Harada, and K. Akashi. Plasma Chem. Plasma Process., 1,113-129 (1981).
12) J. Mostaghimi, P. Proulx, and M. I. Boulos, Plasma Chem. Plasma Process., 4,199-217 (1984).
13) R. M. Young and E. Pfender, Plasm Chem. Plasma Process., 5, 1-37 (1985).
14) J. Mostaghimi, P. Proulx, and M. L. Boulos, J.Appl. Phys., 61, 1753-1760 (1987)
15) P. Proulx, J. Mostaghimi, and M. I. Boulos, Plasma Chem. Plasma Process., 7,29-52 (1987)
16) Japanese version pp.7-585 (1974) of N.B. Vargaftik, Spravochnik po Teplofizicheskim Svoistvam Gazov i Zhidkostei, Nauka (1972).
17) Y. Arata, "High Temperature Engineering," Nikkan Kogyo Shimbun, p.83-89 (1988)
18) K. Kobashi, K. Nishimura, Y. Kawate, and T. Horiuchi, Phys. Rev. B. 38,4067-4084 (1988)
19) B. V. Spitsyn, L. L. Bouilov and B. V. Derjaguin, J. Cryst. Growth, 52, 219-226 (1981).
20) Report No.39, National Institute for Researches in Inorganic Materials, 28 (1984)

Fabrication and Properties of (Y, Ce)-TZP/Al₂O₃ and Y-TZP/Al₂O₃ Composites from Fine Powders Prepared by a Hydrolysis Technique

Masanori Hirano and Hiroshi Inada

Noritake Co., Ltd., Noritake, Nishi-ku, Nagoya-shi 451, Japan

To improve the thermal stability of Y-TZP, the fabrication and properties of yttria- and ceria-doped tetragonal zirconia ((Y, Ce)-TZP)/alumina (Al_2O_3) and Y-TZP/Al_2O_3 composites using fine powders prepared by a hydrolysis technique were studied. The mean values of the bending strength of the composites consisting of 25wt%Al_2O_3 and (Y, Ce)-TZP with compositions 4mol%$YO_{1.5}$-4mol%CeO_2-ZrO_2, 2.5mol%$YO_{1.5}$-4mol%CeO_2-ZrO_2 and 2.5mol%$YO_{1.5}$-5.5mol%CeO_2-ZrO_2 were 1000 to 1100MPa. (Y, Ce)-TZP/Al_2O_3 composites showed no t → m phase transformation on aging at 250°C in air for 1500h. (4Y, 4Ce)-TZP/25wt%Al_2O_3 and (2.5Y, 5.5Ce)-TZP/25wt%Al_2O_3 composites showed no structural degradation and superior stability under the hydrothermal conditions at 180°C and 1MPa as compared with 3Y-TZP, (Y, Ce)-TZP and Y-TZP/Al_2O_3 composites.
[Received June 19, 1990; Accepted October 26, 1990]

1. Introduction

Sintered zirconia maintaining a meta-stable tetragonal structure at room temperature has been attracting considerable attention as a high-strength, high-toughness ceramic material utilizing a tetragonal to monoclinic phase transformation. It's commercial applications are promtoed currently, especially as a structural material. In particular, the Y_2O_3-containing tetragonal zirconia polycrystalline system (Y-TZP)[1] exhibits a high strength of 1000MPa or more.[2] However, tetragonal zirconia with Y_2O_3 as the stabilizing agent is meta-stable at room temperature, and will be transformed into the monoclinic phase from the surfaces, when exposed to low temperatures of 200° to 300°C in air. The phase transformation, accompanied by a volumetric change, may cause the degradation of surface properties as well as of mechanical properties in the long run.[3-5] It is also known that the phase transformation is accelerated in the presence of water.[4-7] A variety of attempts have been made to improve the thermal stability of the TZP system,[8] one of which was the addition of Al_2O_3 to Y-TZP.[9,10] The phase diagrams show that the CeO_2-ZrO_2 (Ce-TZP) system is more thermally stable than the Y-TZP system, because of the former's wider tetragonal region at high temperatures.[11] A Y-TZP system doped with CeO_2, (Y, Ce)-TZP, has also been studied.[10,12] It is, however, generally accepted that Ce-TZP and (Y, Ce)-TZP, although sufficiently thermally stable, are slightly inferior to Y-TZP in mechanical strength.[11]

Several approaches have ben used in the preparation of the starting zirconia material,[13,14] of which hydrolysis[15] is known to result in a highly sinterable starting material.[16] The authors have previously prepared (Y, Ce)-TZP sinters from the Y_2O_3-CeO_2-ZrO_2 fine powders synthesized by the hydrolysis technique, and have investigated the sinterability of the starting powder and properties of the sinters prepared therefrom.[17] In this study, the (Y, Ce)-TZP/Al_2O_3 and Y-TZP/Al_2O_3 composite sinters were prepared from a zirconia fine powders synthesized by the hydrolysis technique, and their mechanical properties, thermal stability in air, and stability under hydrothermal conditions have been investigated.

2. Experimental Procedure

2.1. Sample Preparation

The sample preparation process is illustrated in **Fig.1**. Ammonia water (28wt%) and H_2O_2 water (30wt%) were added to 0.2mol/l of an aqueous solution of zirconium oxychloride ($ZrOCl_2 \cdot 8H_2O$) in the ratio given in **Table 1**. The solution was heated to boiling, to hydrolyze the zirconium compound,[15] yielding hydrated zirconia (monoclinic ZrO_2) particles separated out from the aqueous solution. The average size of the monoclinic ZrO_2 particles thus produced is given in Table 1. Aqueous solutions of yttrium chloride ($YCl_3 \cdot 6H_2O$) and cerium chloride ($CeCl_3 \cdot 7H_2O$) were then added to the above solution, and the mixture was stirred sufficiently. This solution was
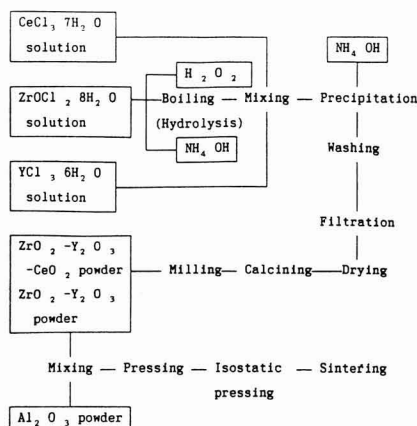

Fig. 1. Flow sheet for fabrication of (Y, Ce)-TZP-Al_2O_3 composites and Y-TZP/Al_2O_3 composites.

Table 1. Preparation conditions and characterization of hydrolyzed zirconia sols.

Starting solution			Boiling	Particle size (Å)	
ZrOCl$_2$	H$_2$O$_2$	NH$_4$OH	time	Crystallite	Secondary
(mol/l) (1)	(ml)	(ml)	(h)	size	particle size
0.2	45	500	750	48	45 a)	500 b)

a) by XRD.   b) by TEM

Table 2. Specific surface areas of zirconia powders.

Composition (mol%)	Specific surface area (m^2/g)
2.5Y$_2$O$_3$ 97.5ZrO$_2$	23
3Y$_2$O$_3$ 97ZrO$_2$	18
4YO$_{1.5}$ 4CeO$_2$ 92ZrO$_2$	27
2.5YO$_{1.5}$ 4CeO$_2$ 93.5ZrO$_2$	25
2.5YO$_{1.5}$ 5.5CeO$_2$ 92ZrO$_2$	26

Table 3. Compositions of specimens.

Material	Specimen	Composition			Al$_2$O$_3$
		Zirconia			
		Composition (mol%)	(wt%)		(wt%)
Y-TZP	2.5Y	2.5Y$_2$O$_3$ 97.5ZrO$_2$	100		0
	3Y	3Y$_2$O$_3$ 97ZrO$_2$	100		0
Y-TZP/ Al$_2$O$_3$	2.5Y25A	2.5Y$_2$O$_3$ 97.5ZrO$_2$	75		25
	2.5Y40A	2.5Y$_2$O$_3$ 97.5ZrO$_2$	60		40
	2.5Y60A	2.5Y$_2$O$_3$ 97.5ZrO$_2$	40		60
	2.5Y80A	2.5Y$_2$O$_3$ 97.5ZrO$_2$	20		80
	3Y25A	3Y$_2$O$_3$ 97ZrO$_2$	75		25
(Y,Ce)-TZP	4Y4Ce	4YO$_{1.5}$ 4CeO$_2$ 92ZrO$_2$	100		0
	2.5Y4Ce	2.5YO$_{1.5}$ 4CeO$_2$ 93.5ZrO$_2$	100		0
	2.5Y5.5Ce	2.5YO$_{1.5}$ 5.5CeO$_2$ 92ZrO$_2$	100		0
(Y,Ce)-TZP/ Al$_2$O$_3$	4Y4Ce25A	4YO$_{1.5}$ 4CeO$_2$ 92ZrO$_2$	75		25
	4Y4Ce40A	4YO$_{1.5}$ 4CeO$_2$ 92ZrO$_2$	60		40
	2.5Y4Ce25A	2.5YO$_{1.5}$ 4CeO$_2$ 93.5ZrO$_2$	75		25
	2.5Y4Ce40A	2.5YO$_{1.5}$ 4CeO$_2$ 93.5ZrO$_2$	60		40
	2.5Y5.5Ce25A	2.5YO$_{1.5}$ 5.5CeO$_2$ 92ZrO$_2$	75		25
	2.5Y5.5Ce40A	2.5YO$_{1.5}$ 5.5CeO$_2$ 92ZrO$_2$	60		40

added, with stirring, to ammonia water, to produce the precipitates, which were washed sufficiently, dried, calcined, and crushed, to produce the zirconia powders. Their compositions and specific surface areas are given in **Table 2**. In the next step, α-alumina (99.99% pure, Taimei Chemical Industry, TM-D) was added to the above powder in a ratio given in **Table 3**, and they were mixed under a wet process. The mixed powder thus prepared was pressed preliminary under 19.6MPa, and then formed by isostatic pressing of 196MPa. The compact was sintered at 1400° to 1600°C for 2h in air.

2.2. Analytical Procedure

Density was determined by the Archimedean method. For mechanical strength measurements, the sintered body was polished with a #140 diamond grindstone into a 3×4×40mm specimen, which was tested to determine its 3-point bending strength by a universal testing machine (Instron, 1123). The test conditions were, span width 30mm, and cross-head speed 0.5mm/min. At least 10 specimens were tested for each sample. Modulus of elasticity was determined for a 1.2×10×50mm specimen from the load-

strain chart, drawn based on the results obtained by the above testing apparatus. The fracture surfaces and the microstructures on the surfaces were observed by a scanning electron microscope (SEM, Hitachi, S450). For thermal stability, the specimen, surface-polished with a #140 diamond grindstone, was held at 250°C for a pre-specified time in air, before it was analyzed by X-ray diffractometry to identify the surface phase, and to analyze quantitatively the monoclinic phase using the method proposed by Garvie, et al.[18] Based on these results, the extent of the transformation from a tetragonal to monoclinic phase was determined. To test its stability under hydrothermal conditions, the specimen was exposed to hydrothermal cycles in an autoclave, each cycle tasting for 5hr from high temperature and high pressure to low temperature and pressure, as illustrated in **Fig.2**. The specimen surface was then analyzed for transformation to the monoclinic phase in the same manner as described above. Autoclave processing time was the total time in which the autoclave was exposed to 180°C and 1MPa.
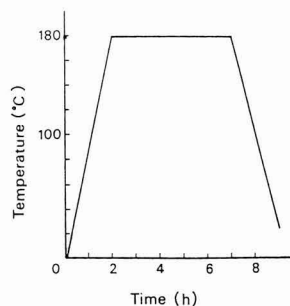
Fig. 2. Autoclave cycle.
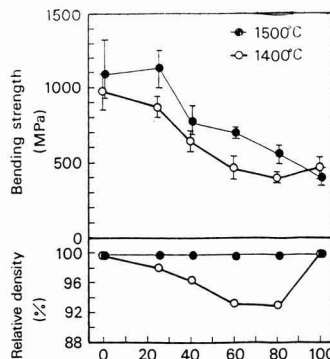
Fig. 3. Changes of bending strength and relative density of 2.5Y-TZP/Al$_2$O$_3$ composites sintered at 1400°C and 1500°C with Al$_2$O$_3$ content.

3. Results and Discussion

3.1. Mechanical Properties and Microstructures

Figure 3 shows the effects of alumina content on bending strength and density of the 2.5Y-TZP/Al$_2$O$_3$ samples, sintered at 1400° and 1500°C. The monolithic TZP and alumina samples were densified to almost their theoretical densities at 1400°C. The starting alumina material used in this study was sufficiently sinterable to be well densified at 1400°C or less.[19] For the samples sintered at 1400°C, the density of the sintered TZP tended to decrease gradually as alumina content increased. Conversely, the density of sintered alumina, decreased greatly when zirconia was added. The composition that gave the minimum sinter density was 60 to 80% by weight, or 70 to 90% by volume, of alumina. On the other hand, at a sintering temperature of 1500°C, the samples were densified to 99% or more of theoretical density in all the Y-TZP-alumina compositions tested, where relative density was based on true specific gravity of 6.10g/cm^3 for TZP and 3.98g/cm^3 for alumina. The X-ray diffraction analysis revealed that each sample consisted of the tetragonal zirconia and α-alumina phases. The strength of the sintered composite tended to decrease as the alumina content increased; however, it was above 1000MPa at an alumina content of 25wt% or less. Thus, essentially no adverse effects by the addition of alumina on the composite strength was observed in the above alumina content range.

Figure 4 shows the effects of alumina content on bending strength and density of the (Y, Ce)-TZP/Al$_2$O$_3$ composites of different zirconia compositions, sintered at 1500°C. No monoclinic phase was detected by the X-ray diffraction analysis on the surfaces of the (Y, Ce)-TZP and (Y, Ce)-TZP/Al$_2$O$_3$ composite samples. Relative density of the composite samples was based on true specific gravity of 6.13g/cm^3 for (2.5Y, 4Ce)-TZP, 6.12g/cm^3 for (4Y, 4Ce)-TZP, and 6.15g/cm^3 for (2.5Y, 5.5Ce)-TZP. The bending strength of partially stabilized zirconia and tetragonal zirconia polycrystals depend on the content and type of the stabilizing agent used, with yttria-stabilized zirconia (Y-TZP) exhibiting the highest strength among the zirconia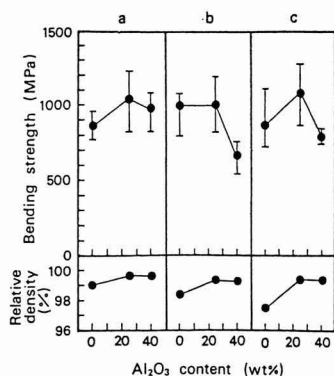-base composites. The yttria-stabilized zirconia has a maximum strength at Y$_2$O$_3$ content of 2 to 3mol%.[2] Of the three types of the (Y, Ce)-TZP composite samples prepared in this study, the (2.5Y, 4Ce)-TZP composition containing the smallest quantity of the stabilizing agent showed the highest average strength. Average strength of Y-TZP was 1000 to 1100MPa, while that of (Y, Ce)-TZP was slightly lower at 850 to 1000MPa. On the other hand, (Y, Ce)-TZP/Al$_2$O$_3$ containing 25wt% of alumina had an average strength of 1000 to 1100MPa, which was roughly 20% higher than that of (Y, Ce)-TZP and equivalent to that of Y-TZP and Y-TZP/Al$_2$O$_3$. Increasing the alumina content in the (Y, Ce)-TZP/Al$_2$O$_3$ composition to 40wt% decreased its strength to a level lower than that of (Y, Ce)-TZP, except in the case of (4Y, 4Ce)-TZP/Al$_2$O$_3$.

The three alumina-containing (Y, Ce)-TZP/Al$_2$O$_3$ composition types prepared in this study were densified to around 99.5% of the theoretical density, and exhibited essentially equivalent relative densities. The volumetric content of alumina in the composite samples containing 40wt% of alumina were only slightly different from each other with a very little difference which resulted from a difference in the true specific gravity of TZP. The volumetric content of alumina was almost the same as that of TZP. Increasing the alumina content beyond a 40wt% level decreased the quantity of zirconia that contributed to the tetragonal to monoclinic phase transformation. At the same time, it changed the major matrix component from TZP to alumina, which greatly decreased its composite strength. The (4Y, 4Ce)-TZP/Al$_2$O$_3$ composition when containing 40wt% of alumina decreased less in average strength than the other zirconia-base composites. This was considered to result from a larger contribution by zirconia in the above composition to the phase transformation, based on the composition's stronger tendency towards the TZP matrix, which resulted from differences in zirconia particle size and in microstructures. The composites containing 40wt% of alumina showed little increase in density, when sintered at 1600°C, and their bending strength was almost the same as that of the composites sintered at 1500°C, as shown in **Table 4**. It is reported that the addition of alumina to Y-TZP and Hip treatment produced highly strengthened sinter.[20] Y-TZP/Al$_2$O$_3$ composites sintered pressurelessly, however, showed little change in strength as shown in Fig.3, in the alumina content range 0 to 25wt%. On the other hand, in the (Y, Ce)-TZP system, the strength improved with the addition of alumina under pressureless sintering.

Table 5 shows the measured results of modulus of elasticity. (4Y, 4Ce)-TZP showed a slightly lower value than 3Y-TZP.

Adding alumina to TZP uniformly increased elastic modulus regardless of the zirconia compositions. No difference in elastic modulus was observed between 3Y-

Fig. 4. Bending strength and relative density of (a) (4Y, 4Ce)-TZP/Al$_2$O$_3$ composites, (b) (2.5Y, 4Ce)-TZP/Al$_2$O$_3$ composites and (c) (2.5Y, 5.5Ce)-TZP/Al$_2$O$_3$ composites sintered at 1500°C.

Table 4. Bulk density and bending strength of (Y, Ce)-TZP/Al$_2$O$_3$ composites sintered at 1600°C.

Specimen	Bulk density (g/cm^3)	Bending strength (MPa)
4Y4Ce25A	5.38	1010
4Y4Ce40A	5.03	990
2.5Y4Ce25A	5.39	970
2.5Y4Ce40A	5.03	750
2.5Y5.5Ce25A	5.40	1030
2.5Y5.5Ce40A	5.05	860

TZP/Al$_2$O$_3$ and (Y, Ce)-TZP/Al$_2$O$_3$. The reason for higher strength of (Y, Ce)-TZP/Al$_2$O$_3$ than (Y, Ce)-TZP can be explained as follows: The monolithic sinter of (Y, Ce)-TZP decreased in relative density as CeO$_2$ content increased,[17] and the density of the sinter did not reach the relative density of Y-TZP. (Y, Ce)-TZP/Al$_2$O$_3$ composites, on the other hand, densified almost to the theoretical density, which explains, 1) Adding alumina to (Y, Ce)-TZP increased relative density. 2) Elastic modulus of (Y, Ce)-TZP, which showed slightly lower value than that of Y-TZP, increased to the similar value of Y-TZP/Al$_2$O$_3$ when added alumina to make (Y, Ce)-TZP/Al$_2$O$_3$.

Figure 5 shows microstructures of fractured surfaces of samples sintered at 1500°C. In (Y, Ce)—TZP/Al$_2$O$_3$ composites, the black portion represents the alumina particle and the white portion the zirconia particle. As shown, the microstructures were characterized by alumina particles uniformly dispersed in the zirconia grain boundaries. The fracture suffaces of the TZP/Al$_2$O$_3$ composition, in which many intergranular fracture of alumina particles were observed were significantly different from those of plain TZP, which consisted of the particles of uniform size with grain boundaries clearly demarcated from the others. The zirconia particles in the (Y, Ce)-TZP/Al$_2$O$_3$ composition were larger than those in the Y-TZP/Al$_2$O$_3$ composition. **Figure 6** presents the SEM photographs of the surfaces of the (4Y, 4Ce)-TZP/Al$_2$O$_3$ composition containing 25wt% alumina sintered at 1400°C and 1600°C. The grains treated at 1600°C notably grew in size. No increase in density or strength was observed by increasing the sintering temperature from 1500° to 1600°C, as shown in Table 4. The desired sintering temperature, therefore, was 1500°C or below, which was consistent with the requirements for thermal stability, discussed below, and to control grain growth.

3.2. Thermal Stability in Air

Figure 7 compares the thermal stability of the (Y, Ce)-TZP/Al$_2$O$_3$ composition with that of the 3Y-TZP and 3Y-TZP/Al$_2$O$_3$ compositions. Thermal stability is represented by the change in monoclinic ZrO$_2$ content with time for

Table 5. Elastic modulus of Y-TZP, (Y, Ce)-TZP, Y-TZP/Al$_2$O$_3$ composites and (Y, Ce)-TZP/Al$_2$O$_3$ composites.

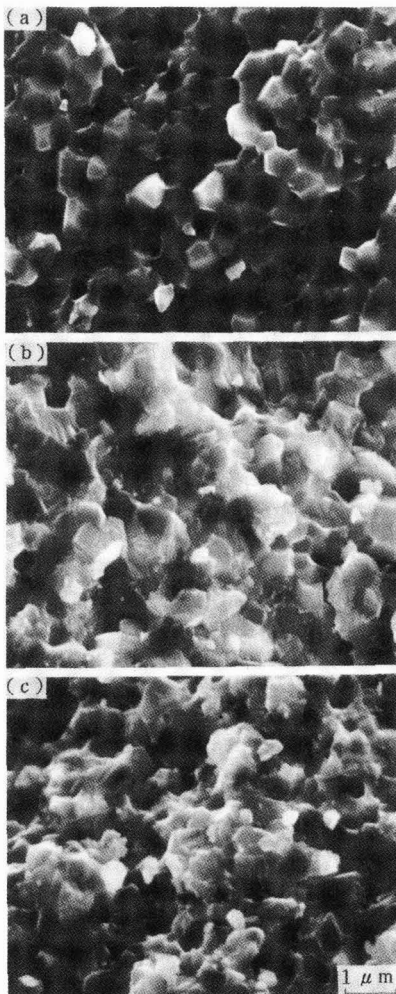| Specimen	Elastic modulus (GPa)
3Y	217
4Y4Ce	195
3Y25A	255
4Y4Ce25A	255
2.5Y5.5Ce25A	254

Fig. 5. SEM photographs of the fracture surface of (a) (4Y, 4Ce)-TZP, (b) (4Y, 4Ce)-TZP/25wt%Al$_2$O$_3$ composites and (c) 2.5Y-TZP/25wt%Al$_2$O$_3$ composites.
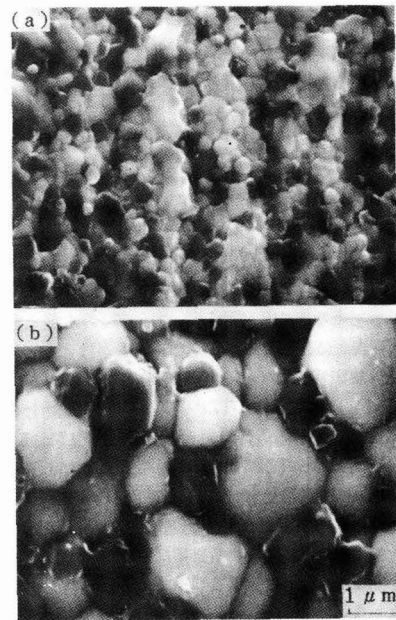

Fig. 6. SEM photographs of the surface of (4Y, 4Ce)-TZP/25wt%Al$_2$O$_3$ composites sintered at (a) 1400°C and (b) 1600°C.

samples maintained at 250°C in air. For the 3Y-TZP composition, the monoclinic phase content increased to 30% in the sample sintered at 1550°C (3Y-1550). The composition sintered at 1500°C (3Y-1500) also showed an increase in the monoclinic phase content with time, although more moderately. For the (Y, Ce)-TZP samples, the (2.5Y, 4Ce)-TZP composition increased in the monoclinic phase to 10%, but no increase or change in structure was observed in the (4Y, 4Ce)-TZP or (2.5Y, 5.5Ce)-TZP compositions up to 1500h.[17] For the alumina-containing composite samples, the 3Y-TZP/Al2O3 composition showed a similar time-dependent increase in the monoclinic phase content as the 3Y-TZP composition, although the level was lower. For the (Y, Ce)-TZP/Al2O3 samples, the (2.5Y, 4Ce)-TZP composition increased in the monoclinic phase content to 10%, whereas the composite containing 25wt% of alumina showed no increase. The three types of alumina-containing (Y, Ce)-TZP compositions contained no monoclinic ZrO2 phase and showed no structural changes on the surfaces after they were aged in air for 1500h. Thus it may be concluded that the addition of alumina to the (Y, Ce)-TZP composition

increases the resistance of the composite to aging under thermal conditions.

3.3. Stability under Hydrothermal Conditions

The sintered samples were exposed to the hydrothermal conditions of 180°C and 1MPa, to investigate the tetragonal to monoclinic phase transformation. **Figure 8** shows the results for the Y-TZP and (Y, Ce)-TZP compositions. The 3Y-TZP composition sintered at 1500° and 1550°C increased in the monoclinic phase content to 56% and 63%, respectively, when treated under the hydrothermal conditions for 10hr. This suggested that the meta-stable tetragonal phase present in the specimen surface was mostly transformed into the monoclinic phase by the hydrothermal treatment within 10hr. For the (Y, Ce)-TZP samples, the (2.5Y, 4Ce)-TZP composition showed the similar time-dependent monoclinic content change as the 3Y-TZP composition. The (2.5Y, 5.5Ce)-TZP and (4Y, 4Ce)-TZP compositions increased in the monoclinic phase content, when treated for 10hr, to 33% and 44%, respectively, which were lower than that for the 3Y-TZP and (2.5Y, 4Ce)-TZP compositions. The changes
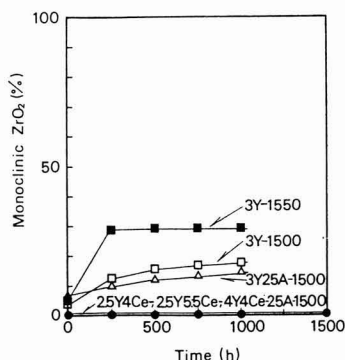
Fig. 7. Result of thermal aging at 250°C in air for Y-TZP, Y-TZP/Al2O3 composites and (Y, Ce)-TZP/Al2O3 composites sintered at 1500°C and 1550°C.
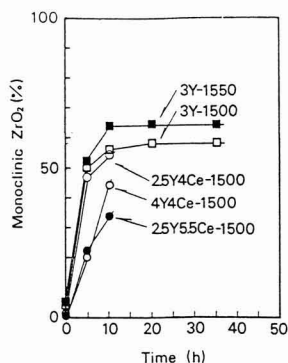
Fig. 8. Results of hydrothermal aging at 180°C and 1MPa for Y-TZP and (Y, Ce)-TZP sintered at 1500°C and 1550°C.
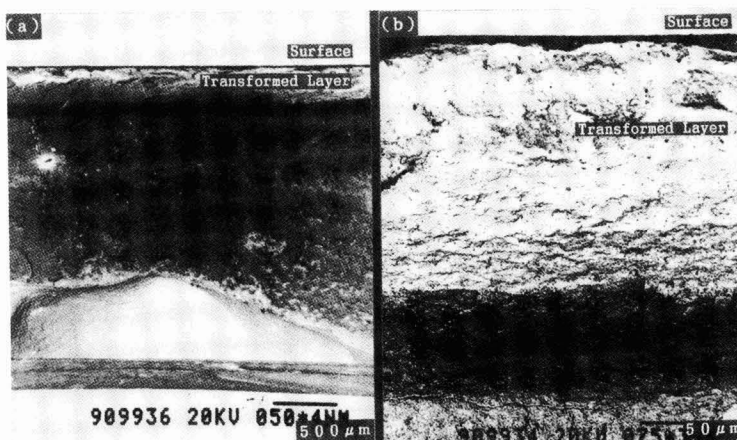
Fig. 9. SEM photographs of the section of (2.5Y, 4Ce)-TZP whose surface layer was peeled off by hydrothermal aging.
(a) The section of (2.5Y, 4Ce)-TZP after hydrothermal aging at 180°C and 1MPa for 35h., (b) A magnification view of (a).

in microstructures were considered to proceed gradually from the surface towards the interior, accompanied by the progression of the phase transformation during the
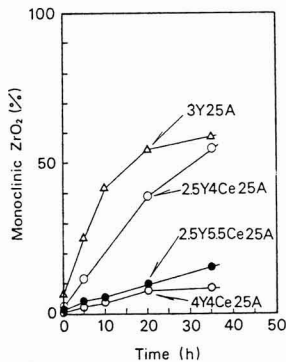
Fig. 10. Results of hydrothermal aging at 180C and 1MPa for Y-TZP/Al₂O₃ and (Y, Ce)-TZP/Al₂O₃ composites sintered at 1500°C.

hydrothermal process. The surface layer of the (Y, Ce)-TZP composition was peeled off, when hydrothermally treated for 15hr or more, making it difficult to analyze accurately the crystalline phases. **Figure 9** presents the SEM photographs of the above sample hydrothermally treated for 35hr, showing that the finely cracked, phase-transformed layer inside into the sample and part of the sample was peeled off. The 3Y-TZP composition showed less structural change in surface of the sample by the hydrothermal treatment than the (Y, Ce)-TZP composition, and had no exfoliated portion after it was ydrothermally treated for 15hr or more. The (Y, Ce)-TZP composition, which showed higher thermal stability than the Y-TZP composition during the aging process in air , was notably degraded, i.e., phase-transformed and exfoliated to a notable extent, during the accelerated aging process under the hydrothermal condition. One of the reasons for the notable degradation of the (Y, Ce)-TZP composition is that it was less densified than the 3Y-TZP composition, due to its lower sinterability, such that water molecules could penetrate through the surface into the interior via the pores in the grain boundaries to accelerate the phase transformation from the tetragonal to monoclinic phase.
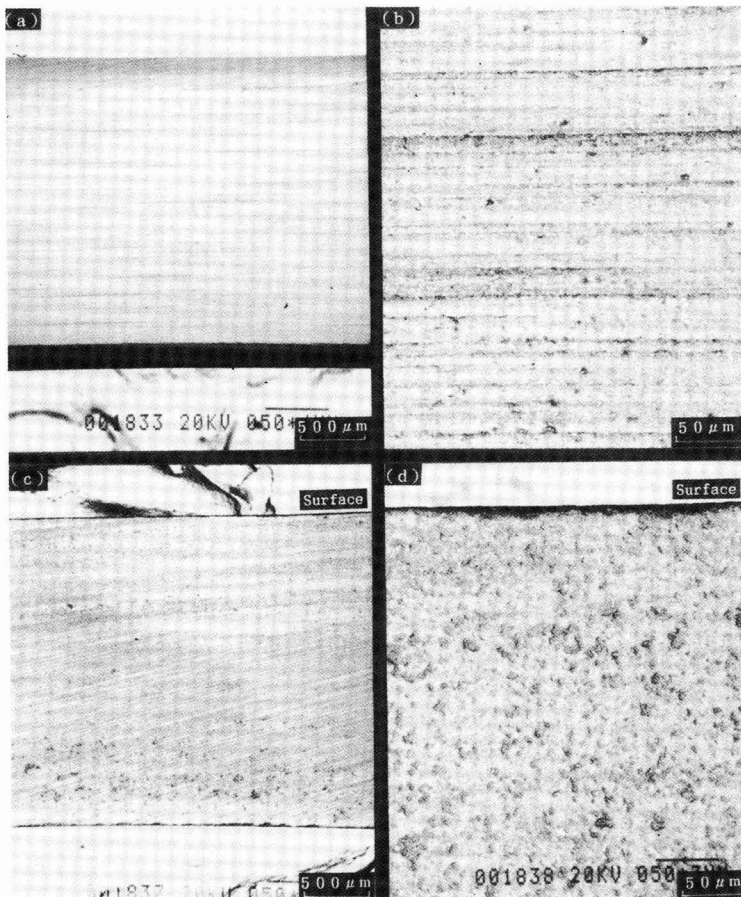
Fig. 11. SEM photographs of (4Y, 4Ce)-TZP/25wt%Al₂O₃ composites sintered at 1500°C after hydrothermal aging at 180°C and 1MPa for 35h: (a) and (b) are surfaces and (c) and (d) are cut surfaces.

Fig. 12. Bending strength of (Y, Ce)-TZP and (Y, Ce)-TZP/Al₂O₃ composites sintered at 1500°C before and after hydrothermal aging at 180°C and 1MPa for 35h.

in the alumina-containing composite samples than the alumina-free 3Y-TZP composites, shown in Fig.8. Of the three types of the (Y, Ce)-TZP/Al₂O₃ samples containing 25wt% of alumina, the (2.5Y, 4Ce)-TZP/Al₂O₃ composition had the largest quantity of the monoclinic phase. The content, however, was almost half the level of the alumina-free (2.5Y, 4Ce)-TZP composition. Increase in the monoclinic phase content was very small in the (2.5Y, 5.5Ce)-TZP/Al₂O₃ and (4Y, 4Ce)-TZP/Al₂O₃ compositions, 15% and 10%, respectively, when the samples were treated under the hydrothermal conditions for 35hr. **Figure 11** presents the SEM photographs of the (4Y, 4Ce)-TZP/Al₂O₃ composites containing 25wt% of alumina, treated under the hydrothermal conditions. No structural change was observed, unlike the case with the alumina-free (Y, Ce)-TZP composition (Fig.9). Thus, addition of alumina improved resistance to hydrothermal conditions, conceivably resulting from (1) increased relative density and modulus of elasticity, and (2) increased strain energy and the controlled release thereof in the presence of alumina: it should be noted that release of the strain energy would be accelerated under the hydrothermal conditions.

Figure 12 shows the bending strength before and after the hydrothermal treatment of the three types of the (Y, Ce)-TZP and (Y, Ce)-TZP/25wt%Al₂O₃ compositions. Each alumina-free composition significantly lost strength due to the hydrothermal treatment, to 30% or less that of the original strength. The alumina-containing compositions, on the other hand, lost no strength by the treatment, except the (2.5Y, 4Ce)-TZP/Al₂O₃ composition which lost strength slightly. It has been thus demonstrated that the (2.5Y, 5.5Ce)-TZP/25wt%Al₂O₃ and (4Y, 4Ce)-TZP/25wt%Al₂O₃ composites exhibit a strength of 1000MPa or more and have sufficiently high stability under thermal and hydrothermal conditions.

4. Conclusions

The (Y, Ce)-TZP/Al₂O₃ and Y-TZP/Al₂O₃ composites were prepared from zirconia fine powders, synthesized by the hydrolysis process, and alumina, where the zirconia powder contained yttria and ceria as the stabilizing agents. Their mechanical and thermal properties were investigated with the following results:

1) The (Y, Ce)-TZP/25wt%Al₂O₃ composition had an average strength of 1000 to 1100MPa, roughly 20% higher than that of the (Y, Ce)-TZP composition.
2) The (Y, Ce)-TZP/Al₂O₃ composition was thermally stable, undergoing essentially no structural change, when exposed to 250°C in air for 1500hr.
3) The (4Y, 4Ce)-TZP/25wt% Al₂O₃ and (2.5Y, 5.5Ce)-TZP/25wt% Al₂O₃ compositions were much more stable under the hydrothermal conditions of 180°C and 1MPa than the 3Y-TZP, (Y, Ce)-TZP and 3Y-TZP/Al₂O₃ compositions, undergoing essentially no structural change by the treatment.

References:

1) T.K. Gupta, F.F. Lange, and J.H. Bechtold, J. Mater. Sci., 13, 1464-70 (1978).
2) K. Tsukuma, Y. Kubota, and T. Tsukidate, Yogyo Kyokai-shi, 92, 11-19 (1984).
3) K. Kobayashi, H. Kuwajima, and T. Masaki, Solid State Ion., 3-4, 489 (1981).
4) T. Sato, S. Ohtaki, and M. Shimada, J. Mater. Sci., 20, 1466-70 (1985).
5) T. Sato and M. Shimada, Am. Ceram. Soc. Bull., 64, 1382-84 (1985).
6) M. Yoshimura, T. Noma, K. Kawabata, and S. Somiya, Seramikkusu Ronbun-shi, 96, 265-70 (1988).
7) T. Shigematsu and N. Nakanishi, "Zirconia Ceramics 9," Uchida Rokaku-ho, (1987), pp.63-71.
8) T. Sato and M. Shimada, Hyomen Kagaku, 10, 11-17 (1989).
9) T. Sato and M. Shimada, Ceramic Society of Japan Annual Meeting Preceedings, (1984) pp.461-62.
10) T. Sato, S. Ohtaki, T. Endoh, and M. Shimada, "Zirconia Ceramics 5," Uchida Rokaku-ho, (1985) pp.75-85.
11) K. Tsukuma, Am. Ceram. Soc. Bull., 65, 1386-89 (1986).
12) T. Watanabe, K. Urabe, H. Igawa, and S. Utagawa, Ceramic Society of Japan Annual Meeting Preceedings, (1984) pp.463-64.
13) S. Somiya, "Zirconia Ceramics 1," Uchida Rokaku-ho, (1983) pp.1-19.
14) T. Suzuki, Seramikkusu, 22, 22-28 (1987).
15) Y. Murase, E. Kato, and M. Hirano, Yogyo Kyokai-shi, 92, 64-70 (1984).
16) Y. Murase, E. Kato, and M. Hirano, Yogyo Kyokai-shi, 91, 561-64 (1983).
17) M. Hirano and H. Inada, Seramikkusu Ronbun-shi, 99, 23-29 (1991).
18) R.C. Garvie, and P.S. Nickolson, J. Am. Ceram. Soc., 55, 303 (1972).
19) Y. Shibazaki, H. Mizuta, S. Sakai, M. Katagiri, and H. Fujimoto, Powder and Powder Metallurgy Society of Japan Annual Meeting Preceedings, (1988) pp.134-135.
20) K. Tsukuma, K. Ueda, and M. Shimada, J. Am. Ceram. Soc., 68, c-56-c-58 (1985).

Impregnation and Firing of Al₂O₃ Compact with CrO₃ Saturated Solution

Takashi Mitamura, Nobuhiko Hayashi and Hidehiko Kobayashi

Department of Applied Chemistry, Faculty of Engineering, Saitama University, 255 Shimo-Ohkubo, Urawa-shi 338, Japan

Conditions of the operation (impregnation method) of the impregnation-dehydration-heating (under 800°C) of the CrO₃ saturated aqueous solution to Al₂O₃ compacts and the filling process of Cr₂O₃ to the basic materials have been investigated utilizing DTA-TG, XRD, SEM, and a Vickers hardness meter. In the heating operation of the Al₂O₃ compacts to which CrO₃ is impregnated, CrO₃ has produced only finely-powdered Cr₂O₃ (≤0.5μm) at a temperature of more than 500°C and the said fine powders of Cr₂O₃ has caused increase of the filling weight to the compacts. In case of more than the number of the times of impregnation where the filling weight of Cr₂O₃ to the fired bodies is almost saturated, a densification layer of Cr₂O₃ was formed in the vicinity of the surface of the fired bodies. The densification layer in question exerts remarkable influence upon the hardness values of Al₂O₃-Cr₂O₃ fired body surface, and the fired body surface hardness has been determined in accordance with the degree of densification layer.

1. Introduction

The process by which a ceramic compact or fired body is impregnated with a liquid, sol or slurry has been established as one method of preparing multi-component ceramic materials. This process involves a series of impregnation-dehydration-heating steps in which a ceramic compact or sinter is impregnated with a solution of an adequate compound, dried thoroughly and then fired to prepare a basic composite reinforced with a new phase. Compounds resulting in adequate impregnation include $SnCl_4 \cdot 5H_2O$,[1] CrO_3,[2-7] Cr_2O_3,[1,2,8] $Al(NO_3)_3 \cdot 9H_2O$,[9] $ZrOCl_2 \cdot 8H_2O$,[10,11] ZrO_2[12] and silicates.[13,14] Of these, CrO_3 is known to be dispersed well in the ceramic basic material to improve its mechanical properties,[1-3,8] corrosion resistance,[2,6,7] heat resistance,[4] and dimension stability,[3] by impregnating a matrix with a saturated aqueous solution of CrO_3, drying and then heating at a relatively low temperature of around 600°C. However, the optimum operating conditions of, and the mechanisms involved in, the impregnation-drying-heating (at 500° to 700°C) are not well understood, even when the process is limited to that for an Al₂O₃ compact saturated with an aqueous solution of CrO_3.

In this study, powdered CrO_3 was selected as the impregnation compound. Its thermal decomposition into Cr_2O_3, and the relationship between the number of impregnation cycles and the Cr_2O_3 filling process in the compact was

investigated for an Al₂O₃ compact treated with a saturated aqueous solution of CrO_3.

2. Experimental Procedure

For the preparation of the Al₂O₃ compact, granulated Al₂O₃ powder (containing 2% of PVA, Showa Denko) was uniaxially pressed (500kg/cm²) in a die into a 50×4×3mm shape, reformed by a rubber press (1t/cm²), heated in air at 1K/min to 500°C, and held at that temperature for 24h for degreasing (cleaning). The compact had a relative density of around 57% on the theoretical Al₂O₃ density of 3.98g/cm³. Powdered CrO_3 was dissolved in distilled water twice to form the saturated aqueous solution.

The impregnation-dehydration-heating process involved impregnation of the Al₂O₃ compact with the saturated aqueous solution of CrO_3, drying in a desiccator, and heating at 300° to 800°C for 30min (heating rate: 5K/min). This procedure was repeated 1 to 11 times to prepare the Al₂O₃-Cr₂O₃ fired body. (In this report, the compact which had undergone the impregnation process plural times is referred to as a fired body.)

The bulk density of the fired body was determined by the Archimedean method with distilled water, and its hardness was determined by a Vickers hardness meter (Akashi Seisakusho AVA-K, equipped with a diamond indenter) under a load of 1kg. For the determination of grain size of the powdered Al₂O₃, a centrifugal sedimentation grain size meter (Shimadzu SA-CP3L) was used for the degreased Al₂O₃ powder. The CrO_3 and $CrO_3+Cr_2O_3$ mixture were analyzed by a DTA-TG analyzer (Rigaku Denki TAS-200) for their thermal decomposition behavior, and by XRD, PSPC (Rigaku Denki RAD-C, PSPC/MDG) and SEM (Hitachi SEM S-800) for the determination of chromium oxides in the fired body and their distributions.

3. Results and Discussion

3.1. Thermal Behavior of CrO₃ Powder and CrO₃+Cr₂O₃ Mixed Powder

In order to optimize the heating conditions for the Al₂O₃ compact to which the CrO₃ saturated aqueous solution was impregnated, thermal decomposition behavior of the CrO₃ powder and CrO₃+Cr₂O₃ mixed powder in air was investigated by heating each sample at 5 to 20K/min. **Figures 1** and **2** show the DTA and TG curves of the CrO₃ powder and CrO₃+Cr₂O₃ mixed powder; the analysis of the CrO₃+Cr₂O₃ mixed powder was to investigate the thermal decomposition of CrO₃ in the presence of Cr₂O₃, since the impregnation (with a saturated aqueous solution of CrO₃)-dehydration-

heating process was repeated plural times. The DTA-TG curves of both the CrO_3 powder and the $CrO_3+Cr_2O_3$ mixed powder were scarcely affected by heating rate; endothermic and exothermic temperature levels, (except for the endothermic peak at around 200°C related to the melting point of CrO_3), and those levels at which sample weight changed, shifted to the high temperature side only gradually as the heating rate increased. Essentially no weight change was observed in the temperature range from around 200° to 300°C in either the CrO_3 powder or the $CrO_3+Cr_2O_3$ mixed powder. The thermal decomposition products obtained at higher temperatures were in the form of bulk agglomerates with traces of foaming; thus it was concluded that there was a liquid phase at the above temperatures.[15] Increasing the temperature of the CrO_3 powder further triggered a stepwise thermal decomposition, producing a 3-staged curve, which

Fig. 1. DTA curves of (a) CrO_3 powder and (b) $CrO_3+Cr_2O_3$ mixed powder.

Fig. 2. TG curves of (a) CrO_3 powder and (b) $CrO_3+Cr_2O_3$ mixed powder.

Shimizu et al. attributed to the formation of Cr_2O_5 and CrO_2 at 390° to 440°C.[15] In contrast, the weight of the $CrO_3+Cr_2O_3$ mixed powder decreased in two steps, with CrO_2 and Cr_2O_3 being detected in the sample heated to 400°C. The XRD analysis confirmed that Cr_2O_3 was the sole decomposition product in both samples at around 500°C, irrespective of the heating rate.

The differences between the CrO_3 powder and the $CrO_3+Cr_2O_3$ mixed powder in their thermal decomposition products and weight loss curve shapes at temperatures above the melting point of CrO_3 were conceivably due to the differences in temperature at which Cr_2O_5 was formed as the intermediate in the process of thermal decomposition of CrO_3 into Cr_2O_3.

Table 1 summarizes the DTA-TG data for the CrO_3 powder and the $CrO_3+Cr_2O_3$ mixed powder together with literature results.[15,16] Both the CrO_3 and $CrO_3+Cr_2O_3$ mixed powders were decomposed into the single final product Cr_2O_3 at around 500°C, when the heating rate was 20K/min or less. It was observed in the thermal decomposition process of the mixed powder that melting of CrO_3 and formation of Cr_2O_5 occurred simultaneously in the presence of Cr_2O_3, which decreased the Cr_2O_3 formation temperature slightly. Thus it was concluded that the Cr_2O_3 formed during the process of impregnation-dehydration-heating using a saturated aqueous solution of CrO_3 had little affect on the filling of Cr_2O_3 to the compact. Furthermore, these results suggested that adequate conditions for decomposing CrO_3 present in the Al_2O_3 compact into Cr_2O_3 were a heating rate of 20K/min or less and a firing temperature of 500°C or higher.

3.2. Effects of Impregnation Cycle Number and Heating Temperature on Cr_2O_3 Filling

Figure 3 shows the relationship between filling rate of chromium oxides to the fired body and the number of impregnation cycles, for the Al_2O_3 compact samples impreg-

Table 1. DTA and TG data for CrO_3 powder and $CrO_3+Cr_2O_3$ mixed powder.

(a) CrO_3 powder

Authors	rate(°C/min)	DTA(°C)	TG(°C)	Products
M.A.Khilla et.al.[16]	10	200(endo)		Cr_3O_8
		270-370(exo)	330,370	Cr_3O_8,Cr_5O_{12},Cr_2O_5
		420(exo)	420	CrO_2,Cr_2O_3
		470(endo)	470	Cr_2O_3
		860(exo)		Cr_2O_3
T.Shimizu et.al.[15]	20	200(endo)		Cr_3O_8
		347(exo)	358	Cr_2O_5,CrO_2
		489(endo)	489	Cr_2O_3
This work	10	204(endo)		
		343(exo)	352,377	Cr_2O_5
		475(endo)	482	Cr_2O_3
This work	20	204(endo)		
		359(exo)	367	Cr_2O_5
		497(endo)	497	Cr_2O_3

(b) $CrO_3+Cr_2O_3$ mixed powder

Authors	rate(°C/min)	DTA(°C)	TG(°C)	Products
This work	10	202(endo)		
		239(exo)		
		398(endo)	396	CrO_2,Cr_2O_3
		457(endo)	457	Cr_2O_3
This work	20	203(endo)		
		266(exo)		
		413(endo)	412	CrO_2,Cr_2O_3
		475(endo)	475	Cr_2O_3

Fig. 3. Relation between number of impregnations and filling rate of chromium oxide.

○: 400°C, △: 500°C, ☐: 600°C, ●: 700°C, ▲: 800°C
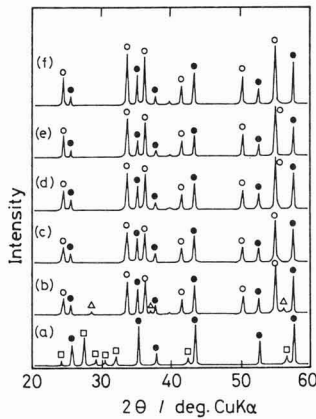
Fig. 4. XRD patterns of fired bodies in Al_2O_3-Cr_2O_3 system obtained by heating in air.

(a) 300°C, (b) 400°C, (c) 500°C, (d) 600°C, (e) 700°C, (f) 800°C,
○: Cr_2O_3, △: CrO_2, ☐: Cr_2O_5, ●: Al_2O_3

nated with a saturated aqueous solution of CrO_3 undergoing the impregnation-dehydration-heating process at least 4 times at 400° to 800°C as the heating temperature. The filling rate was based on the ideal filling of Cr_2O_3 to the Al_2O_3 compact. Chromium oxides included CrO_2 and Cr_2O_5, in addition to Cr_2O_3, taking into consideration thermal decomposition of CrO_3 into Cr_2O_3 at 500°C or above. The filling rate of the chromium oxides to the compact increased sharply at any heating temperature tested, as the number of impregnation cycles increased to 8, and more moderately thereafter. It was also observed that the filling rate increased as the heating temperature increased for a given number of impregnation cycles.

Figure 4 shows the X-ray diffraction patterns of the sample undergoing the 11 impregnation-dehydration-heat-

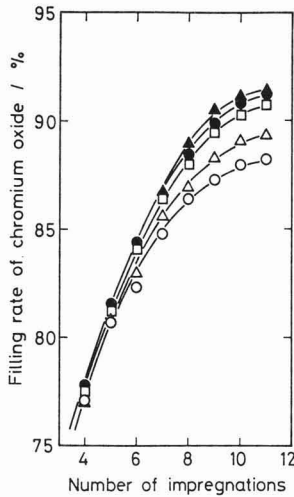ing cycles. Morphologies of the chromium oxides impregnated to the fired body were represented by Cr_2O_5 or CrO_2 when the heating temperature was 400°C or less, and by Cr_2O_3 alone when the temperature was 500°C or more. These results are in good agreement with the thermal analysis of both the CrO_3 powder and the CrO_3+Cr_2O_3 mixed powder. The lattice constants of the Cr_2O_3+Al_2O_3 mixed powder samples, calcined at 500° to 800°C, were also measured by X-ray diffraction analysis to investigate whether Cr_2O_3 was dissolved in the Al_2O_3.[7,18] It was confirmed that essentially no solid solution was formed at a heating temperature of 800°C or less.[3]

Microparticles (≤0.5μm in size) were detected by SEM analysis of the surfaces and fracture surfaces of the fired body. Since the median diameter of the Al_2O_3 powder was around 0.95μm, these microparticles were considered to be composed of Cr_2O_3 formed by the foaming phenomenon[15] accompanying the thermal decomposition of CrO_3. It was therefore concluded that Cr_2O_3 was dispersed in the fired body relatively uniformly, to increase the filling rate.

3.3. Relationship between Vickers Hardness and Heating Temperature of Al_2O_3-Cr_2O_3

Figure 5 shows the relationship between Vickers hardness and the heating temperature of the Al_2O_3 compact samples undergoing 11 cycles of the impregnation-dehydration-heating process. The TG curve of the CrO_3 powder is also shown for comparison. Vickers hardness increased as the heating temperature increased, corresponding to the weight loss accompanying the changes in the chemical morphologies of the lower chromium oxides which were the products of the thermal decomposition of CrO_3. This trend, i.e., increase in Vickers hardness was more noticeable at around 400°C, where Cr_2O_3 was the main product. Hardness increased less sharply above 500°C, where the formation of Cr_2O_3 was almost complete, to around 15GPa at 800°C. The dependence of Vickers hardness on firing temperature was considered to reflect the properties of Cr_2O_3 as the thermal decomposition product of CrO_3 and the filling rate of Cr_2O_3 in the fired body.

The distribution of Vickers hardness in the depth direction was also measured. **Figure 6** shows the distribution within the fired body undergoing 11 cycles of the impregnation-dehydration-heating (600°C) process. The surface of the former sample was ground in succession and it was
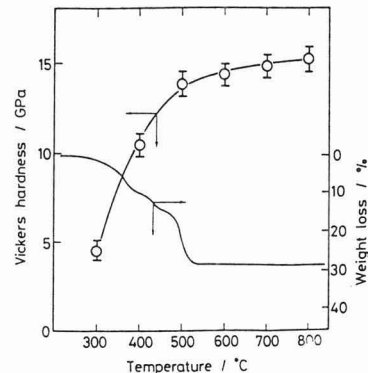

Fig. 5. Change in Vickers hardness and weight loss of TG with temperature.
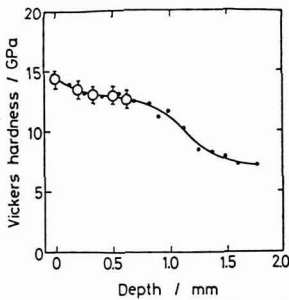
Fig. 6. Change in Vickers hardness in direction of depth for fired bodies obtained by heating at 600°C. Number of impregnations: 11
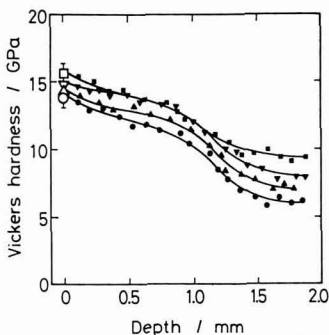
○ : surface, ● : cross-section

Fig. 7. Change in Vickers hardness in direction of depth for fired bodies obtained by heating at various temperatures. Number of impregnations: 11

○, △, ▽, □ : surface, ●, ▲, ▼, ■ : cross-section, ○: 500°C, △: 600°C, ▽: 700°C, □: 800°C

found that hardness of the ground surface was almost equivalent to that of each cross-section. Therefore, the hardness of cross-sections of the fired body interior was measured for each heating temperature. It should be noted, however, that the hardness of each cross-section differed depending on measuring points, to almost the same extent as did the surface hardness; thus the values shown in Fig.6 were the averages of the results obtained in the vicinity of the measuring points.

Figure 7 shows the distributions of Vickers hardness (hereinafter referred to as cross-sectional hardness) in the depth direction of the fired bodies undergoing 11 cycles of the impregnation process. Cross-sectional hardness tended to increase as heating temperature increased, and the effects of the heating temperature were more noticeable at increased depths. The hardness-depth curves of different temperatures were similar to each other in shape, indicating that Cr_2O_3 was filled in the fired body in a similar manner, irrespective of heating temperature.

Assuming that the relationship between Vickers hardness and porosity[3] is applicable to the relationship between Vickers hardness and Cr_2O_3 filling rate, the higher hardness at the surface than in the interior for any temperature level used in this study, indicates that a dense layer of Cr_2O_3 may have been formed in the vicinity of the surface. It was also

concluded that increasing the heating temperature caused the Cr_2O_3 to move further, which improved its dispersion and thereby increased hardness inside the sample. These assumptions are supported by the results shown in Fig.3, and account for differences in filling rates of chromium oxides and differences in hardness distribution by temperature. In an attempt to confirm these conclusions, samples taken from the surface and interior regions of fired bodies were tested by PSPC-aided X-ray diffraction analysis (spot area: 0.1mm in diameter, $CrK\alpha$), comparing the diffraction peak intensities of Cr_2O_3 and Al_2O_3. **Figure 8** shows the PSPC-X-ray diffraction patterns. The relative Cr_2O_3/Al_2O_3 peak intensity was measurably larger in the surface regions (Points A and C) than in the interior (Point B) at both 400° and 600°C. Thus it was confirmed that Cr_2O_3 was filled to a greater extent in the surface region to form a more dense layer than the inside.

3.4. Cr_2O_3 Filling Process and Hardness

The filling rate of Cr_2O_3 to Al_2O_3 and its filling quantity in the surface region differed depending on heating temperature, as shown in Figs.3 and 7; Cr_2O_3 was distributed much more in the surface region than the interior at 500° to 600°C; but at 800°C it had penetrated significantly into the interior. No clear explanation was reached, however, for the different Cr_2O_3 distributions by heating temperature.

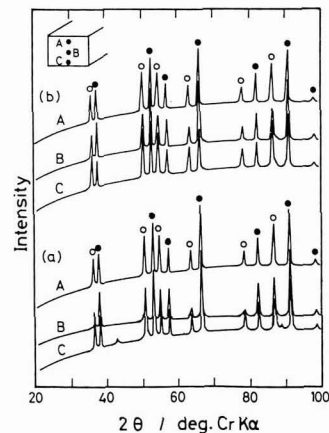The effects of the number of impregnations on Cr_2O_3

Fig. 8. PSPC patterns of Al_2O_3-Cr_2O_3 fired bodies. (a) 400°C, (b) 600°C, ○: Cr_2O_3, ●: Al_2O_3
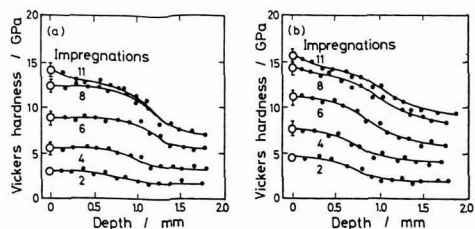

Fig. 9. Influence of number of impregnations of Vickers hardness in direction of depth for fired bodies obtained by heating at (a) 600°C and (b) 800°C.

○: surface, ●: cross-section

filling were investigated by analyzing cross-sectional hardness for the samples undergoing different impregnation cycles. **Figure 9** shows the hardness distributions in direction of depth for different numbers of impregnations at two temperature levels, 600° and 800°C. Cross-sectional hardness increased as the cycle number increased at each depth. The samples undergoing 8 or more cycles tended to have different distributions, and its cross-sectional hardness was notably higher in the surface region than in the interior for the sample undergoing 11 cycles; this indicated that the filled Cr_2O_3 formed a dense layer in the surface region. It should be noted, as shown in Fig.3, that the relationships between filling rate and the number of impregnations for different heating temperatures started to differ from each other at a cycle number of 8. The dense layer was not formed in the first cycle of the impregnation process, but was formed during the cycle in which the filled quantity of Cr_2O_3 was almost saturated, as shown in Fig.9. These results suggest that when Cr_2O_3 is filled sufficiently in the fired body by the impregnation-dehydration-heating process, it is difficult to accurately control dispersion and distribution of Cr_2O_3.[13,14]

The Vickers hardness results also suggested that hardness in the surface region is greatly affected by the dense layer of Cr_2O_3 formed in that region, and is determined by the extent of the dense layer.

4. Conclusions

Powdered CrO_3 was selected as the material to be impregnated to Al_2O_3 compacts via one or more cycles of an impregnation-dehydration-heating process using a saturated CrO_3 solution. The thermal behavior of CrO_3 powder and $CrO_3+Cr_2O_3$ mixed powder were investigated as well as the relationship between the number of cycles in the impregnation process and the Cr_2O_3 filling process.

1) In the heating operation of the Al_2O_3 compacts to which CrO_3 is impregnated, CrO_3 has produced only finely-powdered Cr_2O_3 ($\leq 0.5\mu m$) at a temperature of more than 500°C and the said fine powders of Cr_2O_3 has caused increase of the filling weight to the compacts.

2) In case of more than the number of the times of impregnation where the filling weight of Cr_2O_3 to the fired bodies is almost saturated, a densification layer of Cr_2O_3 was formed in the vicinity of the surface of the fired bodies.

3) Hardness in the surface region of the Cr_2O_3/Al_2O_3 fired body was greatly affected by the dense layer of Cr_2O_3

formed in that region, and was determined by the extent of the dense layer.

(Part of the results reported herein were presented to the annual symposium of the Ceramics Society of Japan in May, 1989.)

References:
1) H.P. Kirchner and R.M. Gruver, J. Am. Ceram. Soc., 49, 330-33 (1966).
2) M. Maruyama, Nikkei Mechanical, 73-79 (1984).
3) Y. Hamano, J.I. Mueller and R.C. Bradt, Ceram. Int., 15, 7-13 (1989).
4) W. Shioda, S. Tagami, and H. Yamaguchi, Unexamined Japanese Patent Publication No.62-234903.
5) S. Matsumoto and H. Kohama, Unexamined Japanese Patent Publication No.62-292681.
6) T. Mori, T. Kumaki, E. Kogure, K. Yamane, T. Arakawa, Y. Matsumoto, F. Noguchi, T. Iida, and T. Mitamura, Yogyo Kyokai-shi, 94, 961-69 (1986).
7) E. Kogure, H. Hiratsuka, C. Noguchi, T. Mori, F. Noguchi, T. Iida, and T. Mitamura, ibid., 95, 1023-30 (1987).
8) Y. Murakami, H. Yamamoto, S. Ono, and H. Tsunoda, Unexamined Japanese Patent Publication No.63-117949.
9) S.J. Glass and D.J. Green, Adv. Ceram. Mater., 2, 129-31 (1987).
10) A. Matsui, T. Ishikuro, and S. Takabayashi, Japan Ceramic Society Annual Meeting Proceedings, (1988) p.442.
11) J. Asaumi, H. Yoshida, N. Miyata, H. Kamiaka, and C. Yamagishi, Seramikkusu Ronbun-shi, 98, 49-55 (1990).
12) K. Nakane and M. Hama, Japan Ceramic Society Annual Meeting Proceeding, (1989) p.313.
13) B.R. Marple and D.J. Green, J. Am. Ceram. Soc., 71, C471-73 (1988).
14) B.R. Marple and D.J. Green, J. Am. Ceram. Soc., 72, 2043-48 (1989).
15) N. Shimizu, H. Yanagida, and K. Hashimoto, Yogyo Kyokai-shi, 84, 298-303 (1976).
16) M.A. Khilla, Z.M. Hanafi, and A.K. Mohamed, Thermochimica Acta, 59, 139-47 (1982).
17) T. Horiuchi, T. Sugiyama, and Y. Takashima, Seramikkusu Ronbun-shi, 96, 881-84 (1988).
18) L.R. Rossi and W.G. Lawrence, J. Am. Ceram. Soc., 53, 604-08 (1970).

Densification Behavior of High-Purity Al₂O₃ and Al₂O₃-15vol%ZrO₂

Hideyuki Harada* and Taketo Sakuma

Dept. of Materials Science, Faculty of Engineering, University of Tokyo, Bunkyo-ku, Tokyo, 113, Japan
*Research Student, on leave of absence from Tokyo Rope Mfg. Co., Ltd.

The densification and grain growth of high purity Al₂O₃ and Al₂O₃-15vol%ZrO₂ were examined in the final stage of sintering. Both densification and grain growth took place much faster in Al₂O₃ than in Al₂O₃-15vol%ZrO₂. The densification rate of Al₂O₃ was explained by the rate equation proposed by Ashby et al., which was slightly modified by taking into account the actual distribution of pores. On the other hand, the densification rate of Al₂O₃-15vol%ZrO₂ was much more sluggish than that estimated from the modified rate equation. The grain-boundary diffusion of constituents might be retarded by the zirconia addition.

1. Introduction

Al₂O₃-based ceramic materials are some of the most widely used oxide ceramics. Due to their superior mechanical and electrical insulating properties and chemical stability, they have been extensively used on a commercial scale. Claussen[1] successfully prepared ZrO₂-reinforced Al₂O₃ (ZTA) by sintering a mixed powder of Al₂O₃ and ZrO₃, which improved the toughness of Al₂O₃ and focused significant attention on the new material, ZTA. To enable the commercial applicability of these Al₂O₃-based ceramics as high-strength, high-toughness materials, it is necessary to sinter them to a high density; for that reason a number of studies have been conducted on the densification of these materials.[2-13] As a result of these studies, it is now generally accepted that a high temperature around 1600°C is needed to fully sinter Al₂O₃ and ZTA. They are normally sintered by hot-pressing or HIP to remove pores completely, and the use of small quantities of sintering aids such as MgO, NiO, CaO and Cr₂O₃, has been found effective, particularly in the case of sintering Al₂O₃. More recently, high-purity Al₂O₃ powders, much purer than the conventional ones, have become commercially available, which can be sintered at relatively low temperatures between 1250° to 1300°C pressurelessly in the absence of sintering aids.[14-16] In addition, these high-purity powders significantly improve the mechanical properties of the Al₂O₃ sinter; ZTA produced from these powders has exhibited excellent mechanical properties, and is expected to find wide use as a new ceramic material for various tools.[17-19] It has been noted that the densification behavior of high-purity Al₂O₃ powder and ZTA are fairly different from that of conventional

materials. In this study, the densification behavior of high-purity Al₂O₃ powder and its mixture with 15vol% of ZrO₂ were quantitatively investigated during the final stage of a pressureless sintering process.

2. Experimental Procedure

Starting materials were high-purity α-Al₂O₃ powder (99.99% pure, average grain size 0.15μm, Taimei Kagaku) and pure ZrO₂ powder (99.9% pure, average grain size 0.03μm, Tosoh) A mixture of Al₂O₃-15vol%ZrO₂ was ball-milled with 5mm diameter TZP balls in the presence of ethanol. The high-purity Al₂O₃ powder and the Al₂O₃-15vol%ZrO₂ mixture were separately reformed under 30MPa pressure in a die of cemented carbides, and then treated by cold isostatic pressing under 100MPa. The compact was sintered at 1150° to 1400°C in air and the linear shrinkage during the sintering process was measured using a thermomechanical analyzer (Rigaku Denki TMA 8140). The density of some samples was measured by the Archimedeth method, and the density of the others was determined from linear shrinkage measurements. Relative density was based on the respective theoretical densities of α-Al₂O₃ (3.987g/cm³) and Al₂O₃-15vol%ZrO₂ (4.296g/cm³). In addition, the sinters were analyzed by transmission (Hitachi-H800) and scanning (Hitachi-S2500) electron microscopes. Grain size was estimated from the fracture faces.

3. Results

Figure 1 shows the effects of sintering time on sinter density for an Al₂O₃ sample sintered at 1200°C and an Al₂O₃-15vol%ZrO₂ sample at 1300°C. Each of the com-
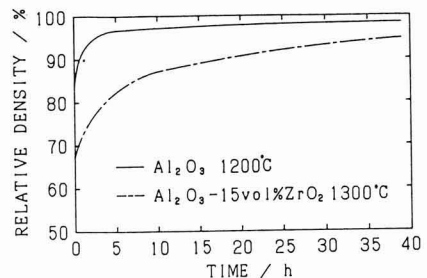

Fig.1. The relation between relative density and sintering time in Al₂O₃ at 1200°C and Al₂O₃-15vol%ZrO₂ at 1300°C.

pacts had a relative density of around 53% before sintering. These samples were sintered to some extent prior to the specified sintering temperature being reached, and at time=0 the Al$_2$O$_3$ sample had a density of around 85% and the Al$_2$O$_3$-15vol%Zr$_2$O sample 68%. As shown, the Al$_2$O$_3$ sample was sintered faster than the composite sample even at a lower sintering temerature (1200°C for Al$_2$O$_3$, 1300°C for the composite). The Al$_2$O$_3$ sample attained a density of above 90% during the heating process, when sintered at temperatures above 1200°C (heating rate:20°C/min). Also, the composite sample could not reach the 90% level even after a very long time when sintered at temperatures below 1300°C; this greatly hindered the quantitative analysis during the final stages of the sintering process. Therefore, the sintering behavior of these samples will be discussed for the Al$_2$O$_3$ sample sintered at 1200°C and the Al$_2$O$_3$-15vol%ZrO$_2$ sample sintered at 1300°C.

Figure 2 shows the densification behavior of each sample type during the latter stages of the sintering process where t=0 is defined as the time at which the density of each sample attained the 90% level. As shown, the Al$_2$O$_3$ sample was sintered much faster than the Al$_2$O$_3$-15vol% ZrO$_2$ sample.

Figure 3 shows the SEM-observed structures of the fractured surface of the Al$_2$O$_3$ sample sintered at 1200°C and the Al$_2$O$_3$-15vol%ZrO$_2$ sample sintered at 1300°C, both for 24h. The Al$_2$O$_3$ sample consisted of coarser grains than the composite, in spite of a lower sintering temperature for the former sample.

Figure 4 shows the effects of sintering time on the average grain size of the two sinter types, where the sizes

of the Al$_2$O$_3$ and ZrO$_2$ grains were averaged for the composite. Again, the time at which the density of each sample attained the 90% level was established as the origin of the time axis (0.5hr for the Al$_2$O$_3$ sample at 1200°C and 15hr for the Al$_2$O$_3$-15vol%ZrO$_2$ sample at 1300°C). The average grain size of the composite was initially larger than the Al$_2$O$_3$ sample. However, the grain growth rate of the Al$_2$O$_3$ sample was much higher than that of the composite under the same condition, resulting in significantly larger grain sizes for the Al$_2$O$_3$ sample. In general, a ceramic material having a smaller grain size is densified faster. Nevertheless, the Al$_2$O$_3$ sample was densified much faster than the composite sample in spite of its larger grain size. Densification behavior of the Al$_2$O$_3$ and Al$_2$O$_3$-15vol%ZrO$_2$ samples will be discussed based on their kinetics.

4. Discussion

The concept of densification rate, proposed by Ashby, et al.,[20] was used to discuss the rate-determining steps in the final stage of sintering of the pure Al$_2$O$_3$ and composite Al$_2$O$_3$-ZrO$_2$ samples. The densification rate $\dot{D}$, after the pores are isolated may be represented by the following equation:

$$\dot{D} = \frac{54\Omega\,(\delta D_b + r D_v)}{kTR^3} \cdot 5\,(1-D)^{1/2} \cdot \left(P_e - P_i + \frac{2\gamma}{r}\right) \quad \cdots (1)$$

where

D : relative density
R : grain radius
Ω : atomic volume
r : pore radius
D_b : diffusion coefficient in the grain boundaries
δ : effective width of the grain boundaries
D_v : volumetric diffusion coefficient
P_e : external pressure
P_i : pressure within the pores
γ : surface energy
k : Boltzmann constant
T : absolute temperature.

In Equation (1), it is assumed that the following relationship holds between the pore radius r and grain radius R:

$$r = R\left(\frac{1-D}{6}\right)^{1/3} \quad \cdots (2)$$

Of the many parameters involved in Equation (1), the pres-
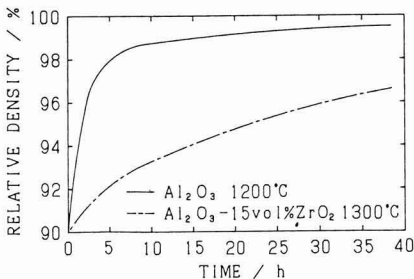
Fig.2. The change in relative density with final stage sintering time. The time when the relative density became 90% is taken to be zero.
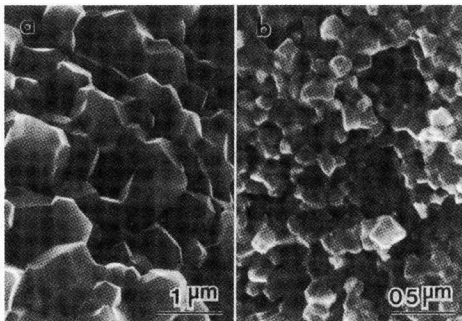
Fig.3. The SEM micrographs of fractured surfaces. (a) Al$_2$O^3 sintered at 1200°C for 24h and (b) Al$_2$O$_3$-15vol%ZrO$_2$ sintered at 1300°C for 24h.
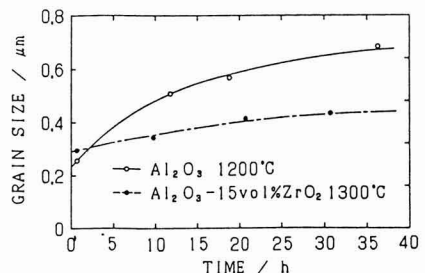
Fig.4. A plot of average grain size as a function of sintering time. The time when the relative density became 90% is taken to be zero.

sure term ($P_e-P_i+2\gamma/r$) as the driving force of densification is considered: P_e represents the external pressure, which is $1\times10_5$Pa for pressureless sintering. P_i is the internal pressure by the gases contained in the pore, and will be around 5.3×10^{-5}Pa at 1300°C, on the assumption that it is equivalent to the vapor pressure of Al_2O_3 at that temperature.[21] P_i is much smaller than P_e, and even though P_i will increase as the pore size shrinks, it will still be much smaller than P_e at around 8.3×10^{-4}Pa (assuming that the pore size is decreased from 0.05 to 0.02μm, and that the relationship PV=constant holds). If the vapor having a pressure of 1×10^5Pa is contained when the pores become closed, the internal prssure in the same manner to P_i=1.6MPa after shrinkage of the pore, which can retard the densification process. In this study, however, the effects of internal pressure were neglected, based on the observation that the densification rate in air was essentially the same as that under a vacuum of 1.0×10^{-1}Pa.

The pressure term $2\gamma/r$ represents the effects of surface energy of the pores. Assuming that the surface energy of Al_2O_3 is $1.0J/m^2$,[22] a pressure of 40MPa would be applied to pores 0.05μm in radius during the final stages of sintering. This is fairly large compared to the afore-mentioned P_e or P_i levels, suggesting that the surface energy term represents the major driving force for the systems handled in this study. In other words, a decrease in the surface energy of the whole system is the major driving force for densification.

Next, the mass transfer mechanisms involved in the densification are discussed. Equation (1) considers two diffusional paths for the constituent ions; the grain boundaries and the grains themselves. Diffusion through these paths are represented by the δD_b and rD_v terms in Equation (1), respectively. The route that transfers more mass will determine the densification rate. For the pores to vanish, the positive as well as negative ions must move, and rate of the overall mass transfer will be determined by the ions that move more slowly. A number of studies have discussed the diffusion of alumina;[3,23-34] diffusion coefficient in the grain boundaries and its volumetric diffusion coefficient of Al^{3+} in Al_2O_3 at 1200°C are:[32]

$$\delta D_b^{Al^{3+}} = 1.0\times10^{-24} \ m^3/s$$

$$D_v^{Al^{3+}} = 6.0\times10^{-20} \ m^2/s$$

When r=0.05μm, $\delta D_b^{Al^{3+}}$=$1.0\times10^{-24}m^3/s \geq rD_v^{Al^{3+}}$=$3.0\times10^{-27}m^3/s$, and the above relationship will be valid in the temperature range used in this study. Diffusion of O^{2-} was predicted in a similar manner. The above analysis suggests that diffusion, as the rate-determining step for densification, proceeds much faster through the grain boundaries than through volumetric diffusion. These results are in agreement with the HIP map of alumina proposed by Ashby et al., in which the regions determined by the diffusion through the grain boundaries account for the entire area.[20] The rate of densification is predicted using the value of δD_b of Al^{3+}, because it is much smaller than that for O^{2-}. **Figure 5** compares the observed densification behavior of alumina at 1200°C during the final stage of the sintering process with the densification behavior calculated from Equation (1), using a grain size $d=2R=0.6$μm and an atomic volume $\Omega=4.25\times10^{-29}m^3$.[20] As shown, the actual densification rate was much slower than the rate predicted by Equation (1). Similar results were obtained for the Al_2O_3-15vol%ZrO_2 samples. One of the reasons for the discrepancy is the pore size distribution at the corners of the grain boundaries.

Figure 6 presents the TEM- observed structures of the Al_2O_3 sample sintered at 1200°C for 10hr. The pores were not always found in all the corners of the grain boundaries, but were found in some of the corners. This was conceivably due to their Ostwald growth, and was based on each pore having its own dimensions including a radius of curvature.[35-38]

Figure 7 shows the Ashby model of the pore distribution,[39-41] and the actual pore distribution of the pure Al_2O_3 and Al_2O_3-15vol%ZrO_2 sample during the final stages of sintering. According to the Ashby model, all of the corners of each grain boundary are occupied by pores, as shown in Figure 7 (a), and the effective diffusion distance is given by:

$$D = 1 - \left(\frac{r}{b}\right)^3 \quad \dots \dots \dots \dots \dots \dots (3)$$
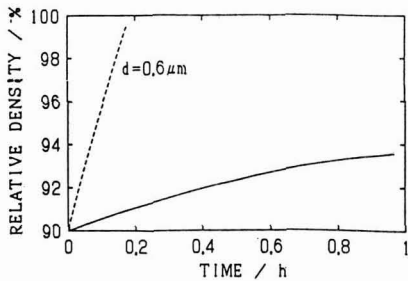

Fig.5. Comparison of theoretical densification rate evaluated from Eq. (1) with experimental data of Al_2O_3 sintered at 1200°C.

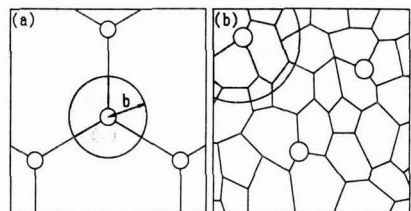**Fig.6.** The microstructure of Al_2O_3 sintered at 1200°C for 10h. The relative density was about 98%.

Fig.7. The pore distribution in two cases, (a) Ashby model and (b) actual distribution in Al_2O_3 and Al_2O_3-ZrO_2.
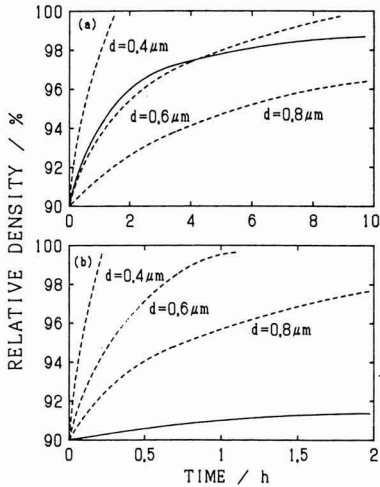
Fig.8. Comparison of theoretical densification rate evaluated from Eq. (6) with experimental data of (a) Al_2O_3 sintered at 1200°C and (b) Al_2O_3-15vol%ZrO_2 sintered at 1300°C. Solid lines are the observed data and broken lines are the calculated ones from Eq. (6) for various grain sizes.

In the case where the pores are present in only some of the corners of each grain boundary, as empirically confirmed in this study, the effective diffusion distance is approximated by:

$$b' = \left(\frac{N}{k}\right)^{1/3} b \quad \ldots \ldots \ldots \ldots \ldots (4)$$

where N is the number of grain boundary corners and n is the number of grain boundary corners in which pores are present. Therefore, in this case, the densification rate given by Equation (1) should be multiplied by a correction factor, N/n.

The empirically predicted N/n level increases as the densification proceeds, and is approximated by the following equation, in a range of relative density D from 0.90 to 0.99:

$$\frac{N}{n} = \frac{0.3}{1 - D} \quad \ldots \ldots \ldots \ldots \ldots \ldots (5)$$

Therefore, the following relationship is introduced to approximate the relative density D, taking into account the correction with respect to the pore distribution and the decreased number of pores during the sintering process:

$$\dot{D} = \left(\frac{0.3}{1-D}\right)^{-4/3} \cdot \frac{54\Omega\delta D_b^{Al^{3+}}}{kTR^3} \cdot 5(1-D)^{1/2} \cdot \frac{2\gamma}{r}$$
$$\ldots \ldots \ldots \ldots \ldots \ldots \ldots \ldots (6)$$

Figure 8 shows the observed and calculated (using Equation (6)) results of the Al_2O_3 and Al_2O_3-15vol%ZrO_2 samples. The results of the Al_2O_3 samples, shown in Figure 8(a), are in fairly good agreement with the calculated results based on the assumption of d=0.6μm. The results of the grain growth behavior, shown in Fig.4, suggest that the size of the Al_2O_3 grains during the sintering process is in a range from 0.25 to 0.65μm. It may be thus concluded that the rate of Al_2O_3 densification is determined by diffusion of the ca-

tions through the grain boundaries. It should be stressed that the densification of readily sinterable, high-purity Al_2O_3 can be represented by kinetic controlled densification described by Equation (6). Commercial Al_2O_3 is generally much less sinterable than the one used in this study, and is sintered at 1500°C or more. That is, ordinary Al_2O_3 is sintered much slower than predicted by Ashby's densification equation. This may be attributable to the retarded diffusion of Al^{3+} through the grain boundaries, caused by impurities and crystallinity of the sample.

The Al_2O_3-15vol%ZrO_2 system, on the other hand, is considered to consist of grains of 0.30 to 0.38μm, as shown in Figure 4. Its densification rate, predicted from Equation (6) using the above grain size, is higher than the observed one by about 2 orders of magnitude; i.e., it is difficult for Equation (6) to explain the densification of a composite system, even when the correction factor is considered. This may result from the retarded diffusion of Al^{3+} through the grain boundaries in the presence of added ZrO_2. As mentioned earlier, the possiblity of a controlled diffusion of Al^{3+} through the grain boudaries in the presence of impurities was one of the reasons for Al_2O_3 being densified differently depending on the purity of the starting material. Viewed from this angle, ZrO_2 can function as an impurity. Perhaps the densification rate of the Al_2O_3-ZrO_2 composite should be assessed using $\delta D_b^{Zr^{4+}}$, if the diffusion coefficient of Zr^{4+} moving through the grain boundaries is much smaller than that of Al^{3+}. Another possibility which cannot be ruled out is that there are interfaces in the sintered composite between the dissimilar phases of Al_2O_3 and ZrO_2, in addition to the grain boundaries of Al_2O_3 and ZrO_2, with the ions diffusing much slower along the interfaces than through the grain boudaries.

As discussed above, several possible reasons can be cited for the lower densification rate of Al_2O_3-ZrO_2 compared to that of the high-purity Al_2O_3 sample. However, there are no measured results for the effects of impurities on diffusion coefficients through the grain boundaries, the $\delta D_b^{Zr^{4+}}$ level in Al_2O_3, and diffusion coefficients along the interfaces of the dissimilar phases. Thus it is difficult to quantitatively discuss how the rate of densification of the Al_2O_3-ZrO_2 composite is determined by the above phenomena. Values of the related properties must be obtained before the densification of the composite system can be fully discussed.

5. Conclusions

Densification behavior of Al_2O_3 and Al_2O_3-15vol%ZrO_2 composite samples during the final stage of the sintering process were investigated.
1) Al_2O_3 was densified much faster than the Al_2O_3-15vol%ZrO_2 composite.
2) The Al_2O_3 grains grew much faster than the grains in the Al_2O_3-15vol%ZrO_2 composite system.
3) The kinetic densification equation, proposed by Ashby et. al., could be used to quantitatively explain the densification behavior of high-purity Al_2O_3, when corrected for an effective diffusion distance.
4) Densification behavior of the Al_2O_3-15vol%ZrO_2 composite could not be explained by the corrected Ashby equation, conceivably due to the retarded diffusion of

Al^{3+} through the grain boundaries, caused by the presence of added ZrO_2.

Reference:

1) N. Claussen, J. Am. Ceram. Soc., 59, 49-51 (1976).

2) H.P. Cahoon and C.J. Christensen, J. Am. Ceram. Soc., 39, 337-344 (1956).

3) R.L. Coble, J. Appl. Phys., 32, 793-799 (1961).

4) S. Kato, T. Iga, M. Sano, and E. Ishii, Yogyo Kyokai-shi, 72, 204-209 (1964).

5) W.R. Rao and I.B. Cutler, J. Am. Ceram. Soc., 56, 588-593 (1973).

6) G. Rossi and J.E. Burke, J. Am. Ceram. Soc., 56, 654-659 (1973).

7) W.C. Johnson and D.F. Stein, J. Am. Ceram. Soc., 58, 485-488 (1975).

8) A.H. Heuer, J. Am. Ceram. Soc., 62, 317-318 (1979).

9) M.P. Harmer and R.J. Brook, J. Mater. Sci., 15, 3017-3024 (1980).

10) T. Kosmac, J.S. Wallace, and N. Claussen, J. Am. Ceram. Soc., 65, 66-67 (1982).

11) F.F. Lange and M.M. Hirlinger, J. Am. Ceram. Soc., 67, 164-168 (1984).

12) T. Hamano, T. Hara, K.Ou, Z. Nakagawa, and Y. Hasegawa, Yogyo Kyokai-shi, 94, 372-379 (1986).

13) K.A. Berry and M.P. Harmer, J. Am. Ceram. Soc., 69, 143-149 (1986)

14) S. Kato, T. Iga, S. Hatano, and Y. Izawa, Yogyo Kyokai-shi, 84, 215-220 (1976).

15) S. Kato, T. Iga, S. Hatano, and Y. Izawa, ibid., 84, 255-258 (1976).

16) S. Kato, Fine Ceramics, 4, 100 (1983).

17) H. Kamiya, M. Takatsu, K. Ohya, M. Andoh, and A. Hattori, Seramikkusu Ronbun-shi, 98, 456-463 (1990).

18) H. Kamiya, M. Takatsu, Y. Kubota, and H. Kodama, ibid., 98, 13-21 (1990).

19) I. Kondoh, M. Asahina, and N. Tamari, ibid., 97, 1424-1427 (1989).

20) A.S. Helle, K.E. Easterling, and M.F. Ashby, Acta Metall., 33, 2163-2174 (1985).

21) Y. Motoki, "Detailed Sintered Ceramics No.4," Giho-do, (1976) pp.337-353.

22) A. Kelly, Strong Solids, Clarendon Press, Oxford (1966).

23) Y. Oishi and W.D. Kingery, J. Chem. Phys. 33, 480-486 (1960).

24) A.E. Paladino and W.D. Kingery, J. Chem. Phys., 37, 957-962 (1962).

25) H.A. Wang and F.A. Kroger, J. Am. Ceram. Soc., 63, 613-619 (1980).

26) D.J. Reed and B.J. Wuensch, J. Am. Ceram. Soc., 63, 88-92 (1980).

27) R.C. Folweiler, J. Appl. Phys., 32, 773-778 (1961).

28) S.I. Warshaw and F.H. Norton, J. Am. Ceram. Soc., 45, 479-486 (1962).

29) R.L. Coble and Y.H. Guerard, J. Am. Ceram. Soc., 46, 353-354 (1963).

30) C.W. Hewson and W.D. Kingery, J. Am. Ceram. Soc., 50, 218-219 (1967).

31) A. Mocellin and W.D. Kingery, J. Am. Ceram. Soc., 54, 339-341 (1971)

32) R.M. Cannon, W.H. Rhodes, and A.H. Heuer, J. Am. Ceram. Soc., 63, 46-53 (1980)

33) R.L. Coble, J. Am. Ceram. Soc., 41, 55-62 (1958).

34) P.A. Lessing and R.S. Gordon, J. Mater. Sci., 64, 174-182 (1981).

35) O.J. Whittemore and J.A. Varela, "Sintering Process," ed. by G.C. Kuczynski, Plenum Press (1980) pp.51-60

36) Y. Uezono and T. Hamano, Yogyo Kyokai-shi, 86, 476-484 (1978).

37) Y. Ohishi, Powder and Powder Metallurgy, 15, 427-431 (1969).

38) W.D. Kingery, H.K. Bowen, and D.R. Uhlmann, "Introduction to Ceramics, Second Edition," A Wiley-Interscience Publication (1976).

39) D.S. Wilkinson, Ph .D. Thesis, Univ. of Cambridge (1977).

40) D.S. Wilkinson and M.F. Ashby, Proc. 4th Int. Conf. on Sintering and Related Phenomena, Plenum, New York (1975) p.473.

41) D.S. Wilkinson and M.F. Ashby, "Science of Sintering," 4th Int. Round Table on Sintering, Vol. 10 (1978) pp.67-76.

Surface-Chemical Study on Stress Corrosion of Glass in Aqueous Solutions (Part 2)
– Influence of Alkali Metal Ions –

Shin-ichi Takeda, Shinji Nakada* and Isao Tari

Department of Applied Chemistry, Faculty of Engineering, Okayama University, 3-1-1 Tsushima Naka, Okayama 700 Japan
*Asahi Chemical Industry Co., Ltd.
1-3-1, Yakou, Kawasaki-ku, Kawasaki-shi, Kanagawa 210 Japan

Post-indentation slow crack growth in soda-lime-silica glass in various aqueous RNO_3 (R, Li, Na K, Rb) solutions was investigated in order to elucidate the mechanism of stress corrosion of glass. The crack growth was found to depend on both the concentration and the nature of the supporting electrolytes. The crack growth was enhanced by the change in the concentration of alkali metal ions from $10^{-4} \sim 1M$, and also by the change in nature of alkali metal ions in the order of Hofmeister series Li^+ Na^+ K^+ Rb^+ at the ion concentration of $10^{-2}M$. This behavior showed that the results obtained can be interpreted in terms of the molecular structure of the glass/electrolyte interface based on the charged states.

1. Introduction

The present study was performed in order to reveal the mechanism of the stress corrosion of glass at molecular level from the viewpoint of the surface-chemistry in which the surface charge developed at the glass/solution interface can be controlled by changing the composition of the test solutions.

Several theories so far have been proposed to account for the mechanism of stress corrosion of glass.[1-7] A generally accepted theory among them is the theory proposed by Hilling and Charles[1] in which the glass was fundamentally taken to be a continuum and they did not intend to elucidate the mechanism of the stress corrosion of glass at molecular level.

In 1980's, Michalske et al.,[4-6] attempted to reveal the mechanism of stress corrosion from the standpoint of molecular theory dealing with the breaking bond reaction at the crack tip. Recently, a new stress corrosion theory at molecular level has been presented by Wiederhorn[7] taking into account the surface force arising between the crack walls. Another paper reported by Zhang et al.,[8] proposed a mechanism based on the water solubility of silicate glass under two-dimensional compressive stresses.

By regarding the oxide-type glass as a metal oxide, we thought we could explain the mechanism of stress corrosion at molecular level utilizing the results of various studies on the state of the surface functional groups of metal oxides.[9-14] Therefore, we compared the charged state of metal oxide with its surface functional groups and attempted to elucidate the mechanism of the stress corrosion of glass.

In our previous paper, we studied the stress corrosion of glass in the aspect of variations in charges at the glass/solution interface with various pH, and found that crack growth in aqueous solutions could be explained in terms of the surface charge.[15] This study continued the investigation using various alkali metal ions to vary the charge at the glass/solution interface, and confirmed that the crack growth could also be explained by the surface charge. We will also attempt to explain the reaction mechanism of breaking bond using the results of quantum mechanical calculations for the charged state of the surface functional groups, and discuss how breaking bond reactions are affected by changes in chemical bonding at the glass surface.

2. Experimental Procedure

2.1. Glass Samples
Commercially available soda-lime silica glass (produced by Matsunami Glass Ind., Ltd. Japan) was used as glass sample. Plate-shaped specimen with 20mm×26mm×1.5mm was used for the crack growth experiments.

2.2. Preparation of Test Solutions
The charged state at the glass/aqueous solution interface was systematically varied using various metal ions. The aqueous solutions for the crack growth tests were prepared as follows:

1) Aqueous solutions containing 1mol/dm³(M) of potassium nitrate were prepared by dissolving a given quantity of potassium nitrate in distilled water.

2) 1M of pottasium nitrate solution was diluted with various pH solutions in order to investigate the concentration dependence on crack growth at various pH solutions.

3) RNO_3 solutions O(R=Li, Na, K, Rb) were diluted with distilled water to obtain $10^{-1}-10^{-4}$ M of solutions in order to investigate a dependence of the concentration of electrolytes on crack growth in constant pH solutions.

A pH meter (made by TOA Electronics Ltd. Japan, Type HM-26S) was used to measure the pH of the solutions.

2.3. Crack Growth Tests
Crack growth tests were performed by the same method as described in our previous paper.[15] Since no further crack growth was apparently observed after the sample immersed for 24hrs, the immersion time was fixed at 24hrs and we made a measurement of crack length at that time.

3. Relationship between Charged State and Crack Growth Behavior

3.1. Fracture Surface Energy and Interfacial Energy

Since the charged state at glass/solution interface can be correlated with interfacial energy, we will interpret crack growth in terms of the energy consumed at the interface. Interfacial energy at glass/solution depended on the composition of the electrolyte solutions. The total energy balance of crack growth in the present test system taking into account of the interfacial energy, is given by

$$\frac{\partial U_e}{\partial A} = \frac{\partial \Gamma}{\partial A} + \frac{\partial \gamma_{KE}}{\partial A} \quad \cdots \cdots \cdots \cdots \cdots (1)$$

$$\frac{\partial \Gamma}{\partial A} = \frac{\partial \gamma_s}{\partial A} + \frac{\partial \gamma_p}{\partial A} \quad \cdots \cdots \cdots \cdots \cdots (2)$$

where ∂A is the increment of the crack surface area. U_e, Γ, and γ_{KE} are the elastic strain energy accumulated in the sample glass by indentation, the fracture surface energy, and the dynamic energy for crack growth, respectively. The terms γ_s and γ_p in equation (2) respectively represent the interfacial energy and the energy consumed during the formation of a nonelastic deformation zone near the crack tip.[16,17] Reversible thermodynamic surface energy has been conventionally used as the term γ_s.[16] In the present test which was carried out in aqueous solutions, the interfacial energy instead of the reversible thermodynamic surface energy was used by taking into account the chemical reaction occurred at the glass surface. If the energy $(\partial \gamma_p / \partial A)$ consumed with the formation of a nonelastic deformation zone in soda-lime silica glass is assumed to be small, the value of the fracture energy for this glass approaches that for the interfacial energy. Therefore, most of the residual stress accumulated in the deformation zone just under the indenter should consume with the fracture surface energy as the crack growth rate is very low $(\partial \gamma_{KE} / \partial A0)$. The rate of the crack growth in this test was as low as 10^{-7} to 10^{-10}m/s and about 10^{-10}m/s or lower toward the end for the crack growth.[15] The fact that the rate of crack growth was very low suggested that the variations in interfacial energy could be reflected in the crack growth.

3.2. Interfacial Energy and Surface Charge Density

Many measurements on the interfacial energy at the metal oxides/aqueous solutions were carried out. These results show that the interfacial energy varied with the composition of the solutions.[18-23] Supposing that soda-lime silica glass is a kind of metal oxide, we can expect for the interfacial energy at the crack tip to vary with the composition of the solution.

It has been generally known that the surface charge density of metal oxides varies with the concentration and the nature of the electrolytes.[10-13] The isoelectric point of the soda-lime silica glass used in the present study was about pH 2.5[15] which agreed closely with that obtained for silica. This agreement may allow to expect the surface charged state of the soda-lime silica glass from the data on surface charge density for silica. Tadros and Lyklema,[10] and Abendroth[11] have reported that the surface charge density of silica in aqueous solutions increases with the concentration of the alkali metal ions such as Li^+, K^+, Cs^+ in the pH range 3 to 9 in which the silica surface has a

negative charge. In the pH range above 5 to 6, the negative surface charge density was in the sequence of $Cs^+ > K^+ > Li^+$ at the concentration of 0.1M.[10,11] These results suggested that the same results on the surface charge density of the soda-lime silica glass should be obtained.

Ahmed at al., have experimentally shown that the interfacial energy has the maximum value at the pH where the surface charge density is zero, and decreases as the surface charge density increases.[9]

We summarized the crack growth behavior in aqueous solutions predicted from the surface charge density as follows:

The further the solution pH is apart from the isoelectric point and the more the concentration of alkali metal ions increases, the higher the glass has the surface charge density. In the case of the constant pH and the concentration of electrolyte, the sequence of the surface charge density was $Cs^+ > K^+ > Li^+$. Since the interfacial energy decreases with increasing the surface charge density, the crack growth should increase to the extent that it is possible to consume the elastic strain energy equivalent to the decrease in interfacial energy.

4. Results and Discussion

4.1. Relation between Crack Growth and Residual Stress

When a microcrack growth test is carried out using Vickers indentation, different from conventional DCB and chevron notch methods, the driving force for crack growth is the residual stress existing in the deformation zone just under the indenter. Therefore, when we discuss the variations in crack growth behavior by changing the composition of electrolytes in terms of the interfacial energy, it is necessary to confirm that the term of $(\partial U_e / \partial A)$ in Equation (1) is not affected by the environment.

Miyata, et al., have already reported that the post-indentation slow crack growth was found to depend on the crack shape and residual stress from the test performed in the environments with various content of moisture.[24] They also reported a technique for calculating the stress intensity factor at the crack tip from the median/radial crack length.[25] In reference to the change in residual stresses caused by the environment, which was the results Miyata, et al., obtained. In our tests, microcracks were first initiated in samples in air with a relative humidity of 40 to 60% and when the length of median/radial crack attained at 95μm, the sample were immersed in the solution prepared in advance. And then, it could be assumed that when the microcracks were initiated, elastic/plastic region were the same size, and also that the size of elastic/plastic region would not changed after the sample immersed. This suggested that there are no difference in the magnitude of residual stresses between various composition of solutions.

4.2. Effect of Concentration of Alkali Metal Ions on Crack Growth

To investigate the effect of alkali metal ions on crack growth, the crack growth for 24hr in a 1M of potassium nitrate solution was compared with that in a solution without potassium nitrate. The results are shown in **Figure1**. Each plot indicates the mean value, and its standard deviation was about ±2%. The effect of solution pH on crack growth
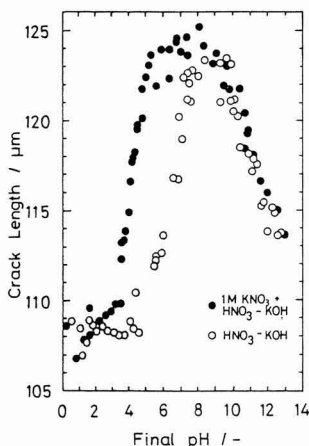
Fig. 1. Crack length as a function of pH for soda-lime-silica glass in aqueous solutions with the 1M KNO₃ (●) and without 1M KNO₃ (○).
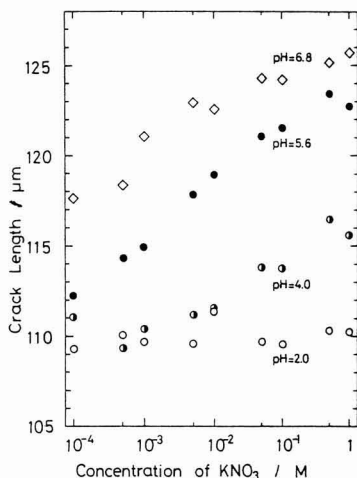

Fig. 2. Crack length as a function of KNO₃ concentration for soda-lime-silica glass in aqueous solutions. Solution pH (◊) 6.8, (●) 5.6, (○) 4.0, (○) 2.0.

potassium ion on crack growth. A relation between crack length and concentration of potassium ion in the pH range from 2 to 7 is shown in **Figure2**. The further the pH of electrolyte solution was apart from the isoelectric point, the more marked was the effect of potassium ion. At the same pH above 4, crack length increased with increase in concentration of potassium ion. When the solution pH was varied, however, the ion concentration dependence of crack growth was not the same. At a relatively low pH such as 4, the effect of potassium ion on crack growth was not significantly unless the ion concentration was high.

These results demonstrated that the effect of the concentration of alkali metal ions on crack growth agreed with the prediction based on the surface charge density.

4.3. Variations in Crack Growth with The Nature of Alkali Metal Ions

To compare the effects of the different nature of alkali metal ions, we investigated crack growth varying the concentration of alkali metal ions systematically within the pH range 5 to 6. The results are shown in **Figure3**. In the concentration from 10^{-4} to 1M of alkali metal ions of any kind, crack length increased with increasing concentration. In addition, their concentration dependence was different in each ions. The Hofmeister series which was well-know in the field of surface chemistry and colloid chemistry[26]

$$Rb^+ > K^+ > Na^+ > Li^+$$
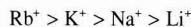
was observed in the crack growth at the concentration of 10^{-2} M. These results also agreed with the results predicted from the surface charged state at the glass/aqueous solution interface.

4.4. Mechanism of Stress Corrosion based on Chemical Bonding

Section 4.1 through 4.3 showed that the crack growth behavior correspond to the variation in surface charge density or interfacial energy, which was controlled by the concentration and the nature of the electrolytes. We will discuss the chemical bonding on the glass surface on the basis of the relation between the state of surface charge and that of the surface functional groups, in order to elucidate the mechanism of stress corrosion at molecular level.

Bond breaking reactions occurred at the crack tip due to the stress corrosion of glass in aqueous solutions have been conventionally explained as a bond breaking resulting from

shows the same tendency. At around pH 2.5, the isoelectric point of soda-lime silica glass, the crack were the smallest, and as the pH increased from the isoelectric point, the crack grew larger. Near the isoelectric point, there were no marked differences due to variation in the concentration of potassium ion. In the pH range 4 to 8, the crack size increased with the increase in the concentration of potassium ion. As the solution pH above 8 to 10, cracks in both solutions become smaller. This decrease in crack size may be due to the dissolution of glass which would result in the change in the surface state of glass, as previously reported.[15] We intend to investigate further relation between slow crack growth and glass dissolution, which will be reported in other paper.

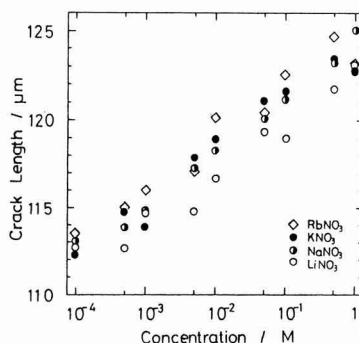We also investigate an effect of the concentration of

Fig. 3. Crack length as a function of concentration of alkali metal ions for soda-lime-silica glass in aqueous solutions.

the change in bonding strength at Si-O bond by the interactions between siloxane bonds and water molecules.[4-6] Michalske, et al., proposed a reaction mechanism which was focused on the molecular structures of the corrosive chemical species.[4-6] The results of the present study such that the crack growth depended on the concentration and the nature of alkali metal ions suggested that the interaction between the siloxane bonds and water molecule is not sufficient to explain the reaction mechanism. In the field of the surface chemistry, the reactions occurred in the presence of water molecules shown in **Figure4(a)** was confirmed using the adsorption test.[14,27] As indicated by the results in Fig.1 through 3, dissociation of protons from the silanol groups on the surface shown in **Figure4(b)** occurred in the pH range above isoelectric point, in addition to the reaction shown in Fig.4(a). Therefore, it is also assumed that the alkali metal ions behave as counter ions against the glass surface which is negatively charged due to the dissociation of protons. Since the glass surface in the aqueous solutions is charged as described above, it is necessary to investigate the variation in the bonding strength in each chemical bond on the surface shown in **Fig.4(I)** to **(III)**. Taking into account of the result that crack growth depends on the solution pH, we thought that the strength of chemical bond shown in **Fig.4(III)** is the dominant stage for the crack growth. Calculating the variation in the electron densities of oxygen at the silanol groups substituted –OH for other halogens in condition (II) and (III) by Xα method, Yoshida, et al., found that the electron density of oxygen was changed with the nature of halogens.[28,29] Based on their results, it is also expected that protons will be dissociated from silanol groups depending on the solution pH, and result to change the electron density of oxygen or the strength of the adjacent siloxane bonds. This suggests that in the pH range above the isoelectric point, the silanol groups on the glass surface are in a stage (III), implying that the strength for the bond between oxygen and silicon atoms which are under stress may change easily. In addition, if an alkali metal ion approaches the oxygen site, the strength of the bond may change to the greater extent. These considerations are supported by the concept of donor and acceptor proposed by Gutmann.[30]
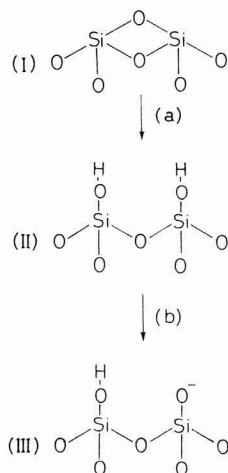
The above discussion at molecular level suggests that the interfacial energy between glass and solution is closely correlated with the strength of bond between atoms near the surface. We believe that if the relationship between the interfacial energy and the strength of bond between atoms is explained, the above mechanism will be applicable to reveal not only the stress corrosion of glass but also the corrosion and grinding of ceramics composed of other metal oxides. At present, it is not possible to show how the chemical bonding is affected by the charge transfer resulting from the interaction between alkali metal ions and the glass surface. Nevertheless, the alkali metal ions definitely affect the bond strength because the crack growth depends on the concentration of alkali metal ions, and the sequence of ion radius and the thermodynamic characteristics of hydration as shown in **Table 1**[3] agree with the sequence observed in the crack growth data. So for the interactions between the glass surface and the approaching alkali metal ions for each stage shown in Fig.4, possible acting agents may be (1) unhydrated (bare) alkali metal ions, (2) hydrated alkali metal ions, and (3) water molecules hydrated with alkali metal ions. It is evident that each of these interactions induces a charge transfer between atoms near the glass surface, but the reaction dynamics for the solid/liquid interface still remains unknown because of the variations in hydration with ion concentration and also because of dissolution of the surface. We are planning to study these aspects in detail by examining the dissolution of glass surface and by characterizing the surface state by a spectroscopy.

5. Conclusion

An effect of alkali metal ions on stress corrosion reactions of glass was investigated, using soda-lime silica glass from the view point of surface chemistry. We found that the gradual crack growth in glass was affected by change in the surface charged state that was affected by the concentration and the nature of the alkali metal ions as well as the

Fig. 4. Schematic representation of the stages in (a) forming surface hydroxyl groups and (b) dissociating proton from the surface hydroxyl groups.

Table 1. Ionic radii and thermodynamics of hydration of alkali metal ions at 25°C.

ion	ion radius[1] nm	hydration entropy ΔS_h J/K·mol	hydration enthalpy ΔH_h J/K·mol	hydration free energy ΔG_h J/K·mol
Li⁺	0.073(4)[2] 0.090(6)	140	552	510
Na⁺	0.113(4) 0.116(6)	108	443	410
K⁺	0.152(6) 0.165(8)	73	358	337
Rb⁺	0.166(6) 0.175(8)	61	333	316

‡1 After R.D.Shannon.

‡2 The number in parentheses is the coordination number.

solution pH. This surface charge effect was thought to be induced by the approach of the positively charged alkali metal ions in the solution toward the negatively charged glass surface. Our study gave evidence that the effect of alkali metal ions could be explained by the surface charged state on the glass as well as the effect of the solution pH. Variations in surface charged state is considered to be corresponding to the strength of chemical bond in solid surface. Therefore, it was concluded that stress corrosion reactions are basically dominated by the strength of chemical bond in glass surface. We believe that this consideration is widely applicable to find reasons for the variations in the interfacial state between metal oxides and solutions as well as all phenomena related to surface reactions.

References:

1) W.B. Hillig and R.J. Charles, "High Strength Materials," Ed. by V.F. Zackey, Wiley & Sons, New York (1985) pp.682-705.

2) S.M. Wiederhorn and H. Johnson, J. Am. Ceram. Soc., 56, 192-97 (1973).

3) Idem. ibid., 58, 342 (1975).

4) T.A. Michalske and S.W. Freiman, Nature, 295, 511-12 (1982).

5) T.A. Michalske and S.W. Freiman, J. Am. Ceram. Soc., 66, 284-88 (1983).

6) T.A. Michalske and B.C. Bunker, J. Appl. Phys., 56, 2686-93 (1984).

7) S.M. Wiederborn and E.R. Fuller, Jr., J. Am. Ceram. Soc., 72, 248-51 (1989).

8) Z. Zhang, K. Nakanishi, K. Hirao and N. Soga, Transaction of Ceramics Society, 97, 365-69 (1989).

9) S.M. Ahmed, "Oxides and Oxide films," vol.1, Ed. by J.W. Diggle, Marcel Dekkr, New York (1972) pp.319-517.

10) The. F. Tadros and J. Lyklema, J. Electroanal. Chem., 17, 267-75 (1968).

11) R.P. Abendroth, J. Colloid and Interface Sci., 34, 591-96 (1970).

12) G.R. Wiese, R.O. James and T.W. Healy, Discuss, Faraday Soc., 52, 302-11 (1971).

13) W.M. Heston, Jr., R.K. ller and G.W. Sears, J.r., J. Phys. Chem., 64, 147-50 (1960).

14) M.L. Hair and W. Hertl, J. Phys. Chem., 73, 4269-76 (1969).

15) S. Takeda, S. Nakata and I. Tari, Transaction of Ceramics Society, 97, 911-115 (1989).

16) T. Nishida and E. Yasuda, Evaluation of Dynamic Properties of Ceramics, Nikkan Kogyo Shinbun, (1986) pp.97-116.

17) M. Sakai, K. Urashima, and M. Inagaki, J. Am. Ceram. Soc., 66, 868-73 (1983).

18) S. Brunauer, D.L. Kantro, and c.H. Weise, Can. J. Chem., 34, 729-42, (1956).

19) Idem. ibid., 34, 1483-96, (1956).

20) J. Laskowski and J.A. Kitchener, J. Colloid and Interface Sci., 29, 670-79, (1969).

21) R.J. Huang, T. Demirel, and T.D. Mcgee, J. Am. Ceram. Soc., 55, 399-405, (1972).

22) Idem. ibid., 56, 87-91 (1973).

23) D.A. Griffiths and D.W. Fuerstenau, J. Colloid and Interface Sci., 80, 271-83 (1981).

24) N. Miyata, S. Takeda and H. Kamino, Materials, 35, 138-44 (1986).

25) N. Miyata, S. Takeda, and H. Kamino, part II, Ms for lectures at 1986 annual meeting of Ceramics Association, 215-16 (1986).

26) F. Kitahara and M. Watanabe, Electrical Phenomena on Surfaces – Basics and Applications –, Kyoritsu Shuppan, (1972), p.59.

27) R.K. ller, "The Chemistry of Silica," Chap. 6, John Wiley & Sons, New York (1979) pp.622-729.

28) K. Yoshida and H. Kawakami, Surface, 21, 737-47 (1983).

29) H. Kawakami, S. Yoshida and T. Yonezawa, J. Chem. Soc., Faraday Trans, II, 80, 205-17 (1984).

30) V. Gutmann, translated by H. Ohtaki and K. Okada, Donors and Acceptors, Molecular Interactions in Solution Reactions, Society Publishing Center, (1982) pp.65-68, 82-84, 91-92.

31) H. Ohtaki, Chemistry of Solutions, Dainihon Tosho, (1987) pp.224-226.

Effects of Carbide Addition on the Mechanical Properties of Ti(C$_{0.5}$, N$_{0.5}$)−30wt%TiB$_2$ Sintered Compacts

Tadahiko Watanabe

Advanced Ceramics Section, Government Industrial Research Institute, Kyushu,
Shuku-machi, Tosu-shi, Saga 841, Japan

Hot pressed Ti(C,N)-30wt%TiB$_2$ ceramics have an average bending strength of 900MPa, but have a wide distribution of bending strength. The additive effects of carbide, namely ZrC, HfC and NbC, were examined in order to improve the distribution.
Addition of these carbides caused that the recommendable sintering temperature is lower than that of Ti(C, N)-30wt%TiB$_2$ system. The addition of 5wt%HfC improved the Weibull coefficient from 8 to 12. Ti(C, N)-30wt%TiB$_2$-5wt%HfC materials had the Vickers hardness of 2100 and the fracture toughness K$_I$C of 4MPam.$^{1/2}$ The hardness and K$_I$C values were same as those of Ti(C, N)-30wt%TiB$_2$ materials.
These phenomena can be explained by the following facts. Added HfC particles react with the Ti(C, N) particles to form Ti rich or Hf rich solid solution of (Ti, Hf) (C, N). These solid solutions limit the grain growth of Ti(C, N). The lower sintering temperature of this system is also effective to suppress the grain growth. The limited grain growth makes higher transverse rupture strengths and their minimized distribution. However, no change in hardness and K$_{1c}$ occurred because of the formation of Ti rich or Hf rich solid solution of (Ti, Hf) (C, N).
[Received July 30, 1990; Accepted November 19, 1990]

1. Introduction

Cutting tools made of sintered Ti(C, N)-30wt%TiB$_2$ are more wear-resistant, and hence more useful for machining carbon steel, than conventional WC-Co or TiC-based cermet tools.[1] Hot-pressed Ti(C, N)-30wt%TiB$_2$ ceramics have an average bending strength (transverse rupture strength) of 900MPa,[2] but the distribution of strengths is fairly wide ranging between 650 and 1150MPa. In an attempt to improve its mechanical properties, several types of carbides such as cubic ZrC, NbC, and HfC were added to the titanium-based composite material, and their effects were investigated.

2. Starting Materials and Experimental Procedure

Table 1 summarizes the chemical components and particle sizes of the starting powders used in this study. Each starting powder was sieved, to remove coarse particles. They were mixed in a given ratio in an agitator-equipped to prepare the starting mixture.

The starting mixture, packed in a die, was hot-pressed under vacuum for 3.6ks; the die pressure was 20MPa.

The hot-pressed ceramics were ground with a #200 diamond wheel into a 4×2×12cm shape with surface roughness of 1.5s or less, to prepare the specimen for bending tests. The transverse rupture strength was determined by a 3-point bending test,[3] under the conditions of span 10mm and loading rate 8.3μm/s. Each sample was tested 6 times, and the average value was reported.

Porosity was determined stereologically from the photographs of the structures. Hardness and fracture toughness were determined by a Vickers hardness test. The elementary analysis (EPMA) was carried out under the conditions of acceleration voltage 25kV, sample current 3×10^{-3}A, and electron beam diameter 1 to 2μm.

3. Results and Discussion

3.1. Effects of Added Carbides on Optimum Sintering Temperature

Figures 1(a) and (b) respectively show the effects of the sintering temperature on the transverse rupture strength and porosity of the titanium-carbonitride-based composite material and that added with 5wt% of ZrC, HfC and NbC. The results shown in Fig.1(a) indicate that the optimum sintering temperature with respect to transverse rupture strength was 1973°K for the binary system of Ti(C, N)-30wt%TiB$_2$; the optimum temperature for the ternary system containing 5wt% of ZrC, HfC or NbC was lowered to 1873°K. It was

Table 1. Chemical composition and particle size of raw materials.

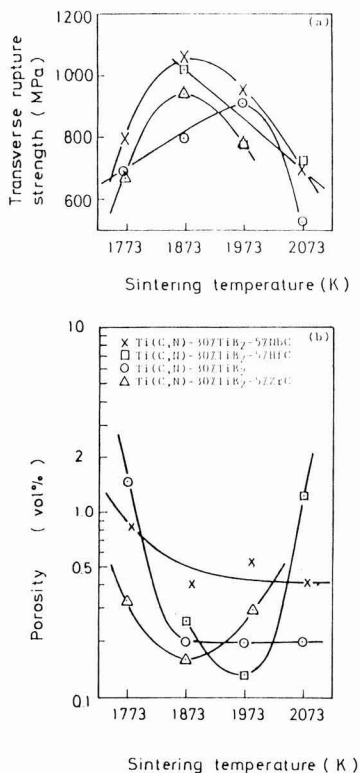| Raw material	Chemical composition	Particle size
TiB$_2$ Ti(C.N)	99.2%pure:C(0.08) , O(0.6) N(10.76) , C(9.78) , O(0.76) Fe(0.16)	<3 μm <3 μm
NbC ZrC	C(11.06) , Ia(0.47) 98.0%pure:Hf(1.65) , O(0.3) N(0.3)	<3 μm <3 μm
HfC	96.5%pure:Zr(1.36) , O(0.02) N(0.15)	<3 μm

Fig. 1. (a),(b) Sintering temperature vs (a) transverse rupture strength and (b) porosity of each material sintered for 3.7ks under the die pressure of 20MPa in a vacuum.

also noted that the NbC- and HfC- containing ternary systems were higher than the binary system in average maximum transverse rupture strength. Each material was sufficiently densified, when sintered at 1873°K, although the NbC-containing ceramics had a slightly higher porosity than the others, as shown in Fig.1(b).

Figure 2 presents photographs of the structures of the Ti(C, N)-30wt%TiB$_2$ system, and the ternary systems containing HfC or ZrC. It is particularly noted that the binary system had a grey Ti(C, N) portion surrounded by a lighter grey Ti(C, N) component. The dark grey portion represents TiB$_2$, the white portion is the HfC- or the ZrC-rich regions, and the black portion reflects the pores. Each sample was sufficiently densified.

It is thus confirmed that addition of 5wt% of HfC to Ti(C, N)-30wt%TiB$_2$ can reduce the optimum sintering temperature and increase the transverse rupture strength.

3.2. Effects of Added Carbide on Ceramic Properties

The sintering temperature was set at 1973°K for the binary system, at 1873°K for the ternary HfC-containing system, and 1973°K for the ternary ZrC- and NbC-containing systems. **Figure 3(a) and (b)** show the effects of carbide content on the transverse rupture strength and porosity, respectively. The carbide content which gave the highest transverse rupture strength differed depending on the type of carbide additive used. The optimum contents were 2, 5 and 10wt% for ZrC, HfC, and NbC, respectively. The highest strength at the optimum content ranged from 1020 to 1120MPa, which as higher than the binary system's strength of 930MPa. Porosity, on the other hand, was less sensitive to carbide content, ranging from 0.15 to 0.4vol%. Ceramic hardness was in a range from 1950 to 2050Hv, almost unaffected by the addition of the carbide. Fracture toughness, K_{IC}, in the range 3.5 to 4.0MPam$^{1/2}$ was also nearly unaffected by the addition of the carbide; in the case of added NbC, however, the fracture toughness did decrease slightly.
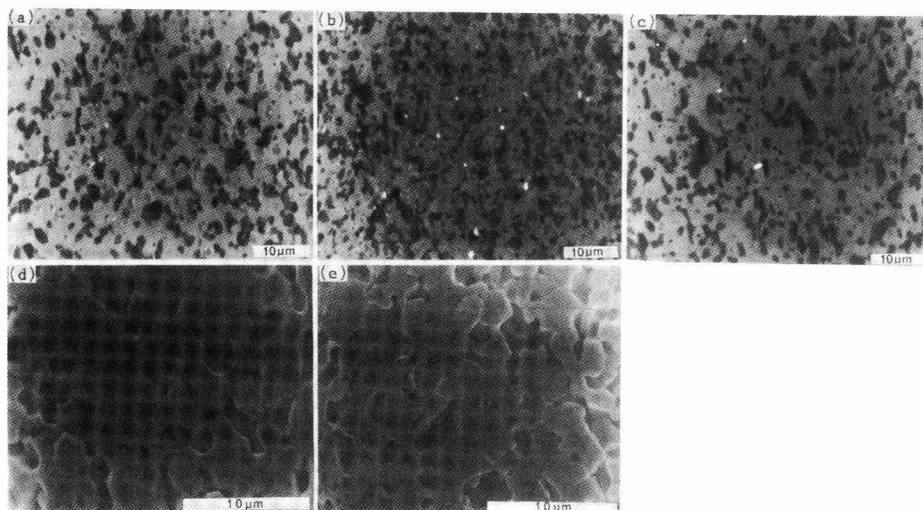

Fig. 2. Back scattered images of (a) Ti(C, N)-30wt%TiB$_2$, (b) Ti(C, N)-30wt%TiB$_2$-5wt%HfC, (c) Ti(C, N)-30wt%TiB$_2$-5wt%ZrC and SEM of (d) Ti(C, N)-30wt%TiB$_2$ and (e) Ti(C, N)-30wt%TiB$_2$-5wt%HfC. Sintering temperature: (a), (b) and (d) 1973K; (c) and (e) 1873K.

4. Discussion

Of the carbide additives used in this study, 5wt% HfC improved the transverse rupture strength, porosity, hardness and fracture toughness better than the other. In particular, the transverse rupture strength was notably improved. However, in general, increases in hardness and fracture toughness were minor.

In order to investigate the increases in transverse rupture strength due to the addition of 5wt% HfC to the Ti(C, N) composition, the strength of each of the binary and HfC-containing ternary systems was measured 30 times, and Weibull plots were drawn, with the results shown in **Figure4**. The addition of 5wt% HfC increased the Weibull coefficient from 7.6 for the binary system to 12.2 for the ternary system. Of particularly note is the fact that the ter-
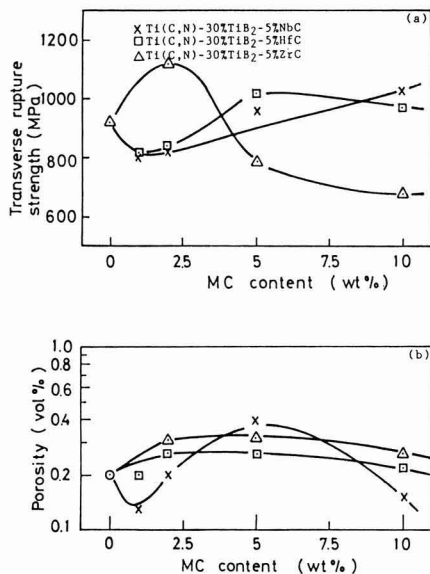

Fig. 3.(a), (b) Carbide content vs (a) transverse rupture strength and (b) porosity of each material. Sintering temperature: 1973K in case of ZrC and NbC addition, and 1873K in case of HfC addition.
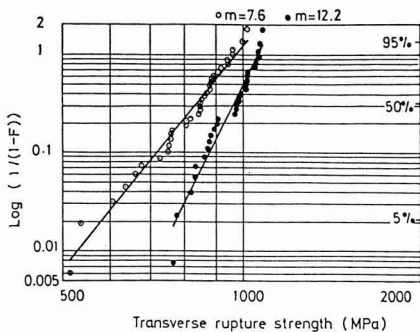
nary system had a strength of 750MPa or less, and that the strengths of one-third of the specimens were concentrated in a range from 1000 to 1100MPa. These results suggested that the addition of HfC reduced the quantity of structural defects in the binary system.

In general, the structural defects were pores and coarse particles. The porosity was relatively constant whether HfC was present or not; thus it was concluded that these samples had equivalent amounts of similarly sized pores.

Figure 2 shows the back-scattered images of the (a) Ti(C, N)-30wt%TiB$_2$, (b) Ti(C, N)-30wt%TiB$_2$-5wt%HfC, and (c) Ti(C, N)-30wt%TiB$_2$-5wt%ZrC compositions, as well as the SEM photographs of the etched (d) Ti(C. N)-30wt%TiB$_2$ and (e) Ti(C, N)-30wt%TiB$_2$-5wt%HfC compositions. Photographs (d) and (e) show the Ti(C, N) particles only, because the TiB$_2$ particles were eluted out by etching. The average sizes of the Ti(C, N) and TiB$_2$ particles present in these systems were measured in the Ti(C, N)-30wt%TiB$_2$ composition sintered at 1973°K as 3.2 and 1.5μm, respectively; in the Ti(C, N)-30wt%TiB$_2$-5wt% HfC composition, average sizes of 2.2 and 1.0μm, were respectively recorded. Thus, both Ti(C, N) and TiB$_2$ particles present in the HfC-containing ternary system were smaller than those in the binary system. One of the reasons for this was the lower sintering temperature which controlled the grain growth.

Figure 5 shows the X-ray diffraction patterns of the starting Ti(C, N)-30wt%-5wt%HfC powder and its material sintered at 1973°K. As a result of sintering, the Ti(C, N) peak was shifted to the low angle side with its half-width increased, and the HfC peak disappeared. These results suggested the formation of a solid solution of (Ti, Hf) (C, N).   This was confirmed by the elementary analysis (EPMA) of the sintered material.   **Figure 6** shows the linear analysis results of the sintered Ti(C, N)-30wt%-05wt%HfC, where the black, grey and white portions represent TiB$_2$, Ti(C, N) and HfC, respectively. N and a small quantity of Ti were found, in addition to Hf and C, in the agglomerated HfC particles, indicating that HfC in the starting powder was sintered into a Hf-rich (Ti, Hf) (C, N) composition. The analysis result also suggested formation of a Ti-rich (Ti, Hf) (C, N) composition from the Ti(C, N) particles, based on the presence of only a small quantity of Hf in these particles. Thus, controlled grain growth as a result of the formation of these solid solutions could be one of the reasons for the increased strength of the sintered ternary

Fig. 4. Weibull plot of transverse rupture strength for (○) Ti(C, N)-30wt%TiB$_2$ and (●) Ti(C, N)-30%TiB$_2$-5%HfC materials.
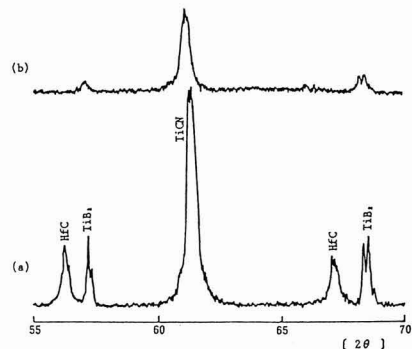

Fig. 5. X-ray diffraction patterns of (a) Ti(C, N)-30wt%TiB$_2$-5wt%HfC raw powder and (b) Ti(C, N)-30wt%TiB$_2$-5wt%HfC sintered materials.

5. Conclusions

Fig. 6. EPMA results of Ti(C, N)-30wt%TiB₂-5wt%HfC materials
sintered at the temperature of 1873K.

system. The formation of the Ti-rich (Ti, Hf) (C, N) and
Hf-rich (Hf, Ti) (C, N) compositions would also account for
the relatively unchanged hardness and fracture toughness
(K_{IC}) of the ternary system relative to the binary system.

ZrC, HfC and NbC were individually added to the binary
Ti(C, N)-30wt%TiB₂ system to form sintered ternary sys-
tems. The transverse rupture strengths, porosities, hardness
and fracture toughness of the sintered materials were mea-
sured to discuss the effects of the additive carbides on sinter
properties.

1) Addition of 5wt% of ZrC, HfC, or NbC to the binary
   system reduced the optimum sintering temperature by
   100°K to 1873°K to give the highest transverse rupture
   strength.

2) Addition of 5wt% of HfC to the binary system increased
   the sinter transverse rupture strength and narrowed its
   distribution, conceivably resulting from the formation of
   solid solutions and from a reduced sintering temperature
   which controlled grain growth.

3) The ternary Ti(C, N)-30wt%TiB₂-5wt%HfC system had
   almost the same hardness and fracture toughness as the
   binary system.

4) The above phenomena were considered to result from
   formation of Hf-rich (Hf, Ti) (C, N) and Ti-rich (Ti, Hf)
   (C, N) solid solutions.

References:

1) T. Watanabe and T. Michitsu, Tool Engineer, 26, 91 (1985).

2) K. Shobu, T. Watanabe and H. Yamamoto, Yogyo Kyokai-shi, 93,
   252 (1985).

3) T. Watanabe and K. Ishikai, Powder and Powder Metallurgy, 26, 304
   (9179).

Preparation of Trimagnesium Phosphate by Mechanochemical Reaction

**Yoshiyuki Yokogawa, Yukari Kawamoto, Motohiro Toriyama, Takahiro Suzuki
and Sukezo Kawamura**

Government Industrial Research Institute Nagoya
1-1, Hirate-cho, Kita-ku, Nagoya-shi, 462 Japan

Trimagnesium phophate hydrate was synthesized by mechanochemical reaction of a slurry of magnesium hydrogen phosphate trihydrate and magnesium oxide with a molar ratio of 2:1 in a pot mill for a few hours. $Mg_3(PO_4)_2 8H_2O$ was obtained by using a slurry with more than 60wt% water; $Mg_3(PO_4)_2 22H_2O$, with 40 wt% water. The anhydrate of trimagnesium phosphate was obtained by heating $Mg_3(PO_4)_2 8H_2O$ or $Mg_3(PO_4)_2 22H_2O$ above 700°C.

1. Introduction

Trimagnesium phosphate has unique characteristics, such as being sparingly soluble in nitrohydrochloric acid.[1] In addition, its octahydrate is useful as a stabilizing agent for calcium hydrogen phosphate ($CaHPO_4 2H_2O$).[2] Trimagnesium phosphate is known to have many polyhydrates, such as ($Mg_3(PO_4)_2 8H_2O$) and ($Mg_3(PO_4)_2 22H_2O$). The octahydrate is called bobierrite, named after its discoverer Bobierre. $Mg_3(PO_4)_2 8H_2O$ is commonly produced from $MgNH_4PO_4 6H_2O$ in an alkaline ammonia solution.[3] However it can take as long as 2 months to complete the production of the target material. Kanazawa, et al., proposed a method to reduce the reaction time,[4] and the process was later refined to react Na_2HPO_4 and $MgSO_4$ in an aqueous solution, initially adjusted to a pH of 6.4 to 7.0 and maintained at 80° to 90°C for 2 to 48hr, to produce $Mg_3(PO_4)_2 8H_2O$.[5] These liquid-phase synthesis processes frequently require accurate pH adjustments.

The authors have developed a mechanochemical synthesis to produce phosphates more simply: calcium hydrogen phosphate and calcium carbonate are mixed in a ratio of 2:1, to which water is added to make a 10% slurry, and then stirred in a pot mill to produce calcium-deficient apatite which is then calcined into tricalcium phosphate consisting of particles having an average size of 1 μm or less.[6] In this process, a mechanochemical action is applied to the starting materials which are sparingly soluble in water; the reaction requires no pH adjustment, and is characterized by the relatively simple synthesis of tricalcium phosphate particles of uniform size. In this study, the mechanochemical approach was applied to the production of trimagnesium phosphate.

2. Experimental Procedure

2.1. Synthesis of Trimagnesium Phosphate

To a mixture of 0.2mol of magnesium hydrogen phosphate trihydrate (special grade, Wako Junyaku) and 0.1mol of magnesium oxide (special grade, Wako Junyaku) varying quantities of water (0-90wt%) were added to make a slurry. The slurry thus prepared was milled using 500g zirconia balls in a zirconia pot mill (75mm inner diameter, 90mm deep, Kagaku Togyo) at 50rpm and room temperature, to allow the components to react. The ball-milling time was varied from 1 to 24hr. The reacted slurry was dried to produce a powder, which was thermally treated in air at 700°C for 1hr.

2.2. Analytical Procedure

Each sample prepared under the varying conditions was analyzed by X-ray powder method (Geiger flex, Rigaku Denki), using a carbon monochrometer, and CuKα ray, at 30kV, and 20mA. The samples were also observed by a scanning electron microscope (SEM, Hitachi, SX-5300). The thermal analysis was carried out using a differential thermal analyzer (Shinku Riko, TA7000), where the sample was heated at 10°C/min in air. Average particle size was determined using a grain size analyzer (Shimadzu, SA-CP3), based on the centrifugal sedimentation with a 0.2% sodium pyrophosphate solution as the dispersant. A transmission electron microscope (TEM, JOEL, JEM4000FX) was to observe the image and used to determine the elemental compositions.

3. Results and Discussion

3.1. Products of Mechanochemical Synthesis

Figure 1 presents the powder X-ray diffraction patterns of the dried powder prepared from the slurry with varying quantities of water ball-milled in a pot. The pattern of the sample containing 40wt% water coincided with that of $Mg_3(PO_4)_2 22H_2O$;[7] patterns of samples containing more water corresponded with that of $Mg_3(PO_4)_2 8H_2O$.[8] On the other hand, the sample ball-milled in the absence of water only exhibited the diffraction patterns of starting materials: magnesium hydrogen phosphate trihydrate and magnesium oxide.[9,10] In other words, ball-milling of magnesium hydrogen phosphate and magnesium oxide produced a mere mixture in the absence of water, but produced polyhydrates of trimagnesium phosphate in the presence of water. It is known that both magnesium hydrogen phosphate and magnesium oxide are sparingly soluble in water,[11] and hence

they should not react with each other, only in the presence of water. It has also been reported that magnesium hydrogen phosphate trihydrate is dehydrated when mechanically agitated, eventually reaching the amorphous state.[12] However, the authors observed that it was not dehydrated when mechanically agitated in the presence of water, but rather the so-called mechanochemical effects were observed to proceed gradually. It was also found that $Mg_3(PO_4)_2 22H_2O$ was formed in the presence of an insufficient quantity of water, and that the formation of $Mg_3(PO_4)_2 8H_2O$ predominated as water quantity increased. Beyond a certain quantity of water, $Mg_3(PO_4)_2 8H_2O$, believed to be the most stable among the polyhydrates of trimagnesium phosphate,[13] was preferentially formed. It has been thus demonstrated that the mechanochemical process produces polyhydrates of trimagnesium phosphate relatively easily and in a short period of time, without requiring pH adjustments.

Figure 2 presents SEM photographs of the ball-milling products formed in the presence of (a) 0wt% (b) 40wt%and (c) 90wt% water. The spherical particles were produced when water was not used, and were considered to be magnesium hydrogen phosphate trihydrate. Increasing the quantity of water to 40wt% produced plate-shape crystals, which were considered to be $Mg_3(PO_4)_2 22H_2O$.[14] Further increasing the quantity of water to 90wt% produced rod-shape crystals, which were $Mg_3(PO_4)_2 8H_2O$.[14] Each sample was observed by transmission electron microscope while being supported by a Cu mesh coated with a collodion film, under a voltage of 300kV, to determine its composition by energy
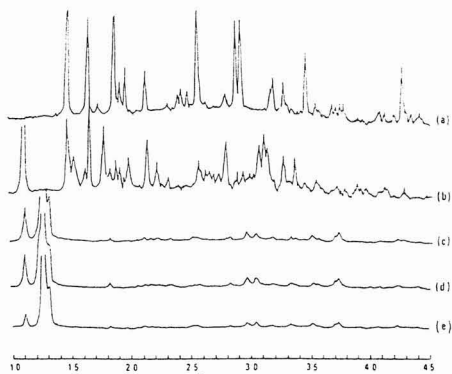
dispersion analysis. Each sample was found to have a Mg/P_2 ratio of 3, suggesting a trimagnesium phosphate compound.

Different ball-milling times produced almost the same products, as long as the quantity of water was the same. Increasing the ball-milling time, however, reduced the average particle size, as shown in **Figure 3(a)**. The slurry pH level stayed between 8 to 9 as shown in **Figure 3(b)**, but tended to decrease as the ball-milling time increased, conceivably resulting from the partial decomposition of phosphate by mechanical agitation and crushing.

3.2. Thermal Analysis of Products

The slurry of polyhydrates of trimagnesium phosphate was dried, and the powder was thermally analyzed. **Figure 4** presents the differential thermal analysis curves of the powdered samples prepared in this study. The samples from the slurries containing 60wt% or more of water had large endothermic peaks between 100° and 200°C and an exother-

Fig. 3. Relationship between stirring time(h) and (a)particle size(μm) (O) or (b) pH (△) of the products obtained by stirring a slurry, a mixture of MgHPO₄3H₂O and MgO in a pot-mill with 90wt% water.

Fig. 1. X-ray diffraction patterns of the products obtained by stirring a slurry, a mixture of MgHPO₄3H₂O and MgO with (a) 0, (b)40, (c)60, (d)80 and (e)90wt% water in a pot-mill for 24h.

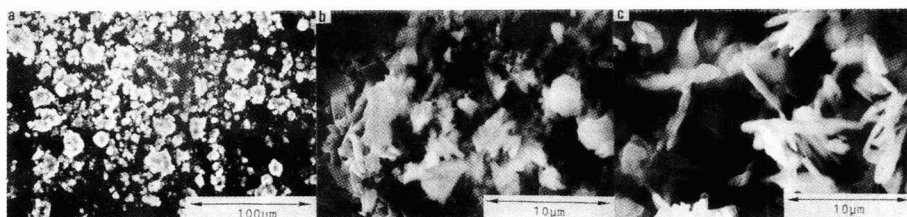**Fig. 2.** Scanning electron micrographs of the products obtained by stirring a slurry, a mixture of MgHPO₄3H₂O and MgO with (a)0, (b)40 and (c)90wt% water for 24h.

Fig. 4. Thermal analysis of the products obtained by stirring a slurry, a mixture of $MgHPO_4 3H_2O$ and MgO with (a) 90, (b) 80, (c) 60 and (d) 40wt% water for 24h.

mic peak between 650° and 700°C. It is known that heating trimagnesium phosphate octahydrate between 50° and 200°C removes the waters of hydration to yield the amorphous state, and between 650° and 700°C, the amorphous phosphate is crystallized, forming a powder of trimagnesium phosphate.   Therefore, the observed DTA peaks resulted from the decomposition of trimagnesium phosphate octahydrate and the crystallization of trimagnesium phosphate, respectively. These results, coupled with the powder X-ray diffraction analysis results, indicated that octahydrate was the sole product from the slurry containing 60wt% or more of water. The DTA curve of the sample produced from the slurry containing 40wt% of water had in addition to the above two peaks a large endothermic peak around 50°C which corresponded to the decomposition of $Mg_3(PO_4)_2 22H_2O$.[13] Powder X-ray diffraction analysis sug-

gested the formation of $Mg_3(PO_4)_2 22H_2O$, but the sample also contained some of the octahydrate, based on the endothermic peak found around 200°C during thermal analysis.

4. Conclusions

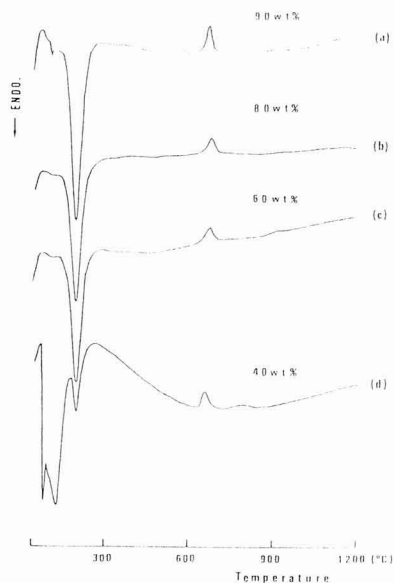It has been shown that a slurry of magnesium hydrogen phosphate trihydrate and magnesium oxide can react by ball-milling to produce polyhydrates of trimagnesium phosphate. $Mg_3(PO_4)_2 8H_2O$ was the product from the slurries containing 60wt% or more of water, and $Mg_3(PO_4)_2 22H_2O$ was the major product from the slurry containing 40wt% of water.

Reference:

1) T. Kanazawa, "Inorganic Phosphor Chemistry," Kodan-sha, (1985), pp.201-204.

2) M. Izuyama, Electrochemistry, 39, 509-516 (1971).

3) A. W. Franzier, J. R. Smith, Am. Mineral., 48, 635-641 (1963)

4) T. Kanazawa, T. Umegaki and E. Wasai, Chem. Lett., 1974, 817-818

5) T. Kanazawa, T. Umegaki and M. Shimizu, Bull. Chem. Soc. Jpn., 52, 3713-3717 (1979)

6) M. Toriyama and M. Kawamura, Yogyo Kyokai-shi, 94, 78-82 (1986).

7) JCPDS # 35-186

8) JCPDS # 16-330

9) JCPDS # 35-780

10) JCPDS # 4-829

11) Kagaku Binran, edited by the Chemical Society of Japan, "Part 3 Properties of Compounds," p.1-80.

12) Y. Arai and M. Yasue, J. of Chemical Society of Japan, 1972, 198-200.

13) T. Kanazawa, T. Umegaki, and M. Iwase, Sekko to Sekkai, 131, 143-148 (1974).

14) T. Kanazawa, T. Umegaki, and E. Wasai, Sekko to Sekkai, 140, 4-8 (1976).

Effect of Grain Size of Quartz on Mechanical Strength of Porcelain Bodies

Kenya Hamano, Yueh-Hong Wu*, Zenbe-e Nakagawa** and Minori Hasegawa**

Department of Applied Chemistry, Faculty of Engineering, Kanagawa University
* Hocheng Pottery Mfg. Co., Ltd., Taiwan, China
** Research Laboratory of Engineering Materials, Tokyo Institute of Technology

The effect of grain size of quartz on mechanical strength of porcelain body was examined. The bending strength of the fired body increased with an increase in interplanar spacing of quartz in the fired body, which indicates that the quartz is under a tensile stress. Consequently, the glassy matrix surrounding the quartz grains is a compressive stress which acts as prestress, improving mechanical properties. The strength of the body depends on the grain size of quartz, and maximum strengths were obtained at 10 to 20, 5 to 10 and 5μm, respectively, fired at 1400, 1350 to 1250 and 1200°C. Smaller and larger quartz grains gave lower strength, probably because of extensive dissolution and crack generation, respectively.

1. Introduction

It is often presumed that manufacturing methods for ceramics are established, leaving no room for further improvements in the mechanical strength of the product; however, by using additives such as alumina advances can be made. Regarding the mechanical strength of porcelain bodies, two theories have been presented: the mullite theory stresses the existence of acicular mullite crystals, and the prestress theory explains that compressive stresses caused in the vitreous phase by the difference in thermal expansion coefficients between the quartz crystal grains and the surrounding vitreous phase produce a prestress effect. We have already reported that although sufficient consideration has not been given to grain size, the prestress effect of quartz grains was more important.[1] Taking into consideration such factor as the content, grain size distribution, and dissolution of quartz during firing, as well as the difference in the thermal expansion coefficients of quartz and the vitreous phase, and the difference between the room temperature and glass transition temperatures, Marzahl[2] derived a formula for the effect of quartz on the strength of porcelain bodies, explaining that at a certain level of quartz grain size, stresses produced in the vitreous phase are maximal and that the larger they are, the higher the porcelain strength. Mattyasovszky-zsolnay[3] suggested that the prestress effect was proportional to the residual quartz content in the porcelain body. If the quartz grains are very fine, they are too highly dissolved. If the grain size is larger than

10 to 30μm, the vitreous phases, and been the quartz grains are cracked due to a phase transition. In both of these cases, the strength of the product is reduced. Stuckert et al.[4] reported that if porcelair body prepared in a standard mixture was fired at SK14, grain sizes of 10 to 25μm provided high strengths, while Kraus[5] found that grain sizes of 14 to 28μm for the case of high-temperature sintering (SK15) and of 2 to 12μm for low-temperature sintering (SK11) resulted in high porcelain strength. Weyl[6] explained that the strength could be increased by pulverizing the quartz and reducing the quartz content. Berens[7] reported that for grain sizes in the range 10 to 30μm, strength was maximized.

On the other hand, Wiedmann[8] reported that high strengths could be obtained from high concentrations of fine quartz grains, and that mullite helped to improve the porcelain strength. Palatzky,[9] however, reported that higher strengths were obtained from lower quartz concentrations and higher mullite contents. Rieke, et al.,[10] and Budnikov[11] suggested that mullite dominates the strength of porcelain bodies, and Masson[12] stated that higher strengths could be obtained by replacing quartz with low-expansion porcelain powder. Thus, there are several supporters of the mullite theory, as well as others who are of the opinion that the very existence of residual strains due to quartz grains is harmful to the porcelain strength.[8]

In short, reports are divided between those that suggest that the mechanical strength of porcelain bodies depends on quartz grains and those that believe that it is dominated by mullite, not by quartz which is rather harmful. If quartz indeed improves the strength, such factors as its optimal grain size and firing conditions should be determined. Recently, demand has been rising for high-strength porcelain bodies, encouraging studies on various porcelain additives. For such studies, it is necessary to know the relationship between quartz as an essential nonplastic component and the strength of the porcelain products. Today, much more is understood regarding the breakdown mechanisms of ceramics. Utilizing this knowledge will be helpful in reaching a definite conclusion to the above problem.

To understand in greater detail, the effect of quartz on the mechanical strength of porcelain bodies, we investigated the relationship between the firing temperature of porcelain, quartz grain size, and the bending strength of the products.

2. Experimental Procedure

Katoh kaolin from Korea, and potassium feldspar from India which were pulverized and the portion with the grain sizes in the range of 10 to 20μm was collected by elutriation,

Table 1. Chemical compositions of raw materials.

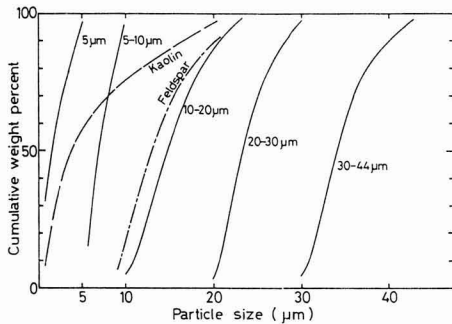|	SiO₂	TiO₂	Al₂O₃	Fe₂O₃	CaO	MgO	K₂O	Na₂O	Ig.loss
Korean kaolin	46.37	0.16	37.42	0.93	0.42	0.26	0.73	0.42	13.00
Indian feldspar	65.66	0.01	18.69	0.08	0.10	0.01	12.32	2.89	0.20
Quartzite	99.74								

Fig. 1. Grain size distribution of raw materials.

and pulverized high-purity quartzite were used as starting materials. The quartzite was sifted into 3 groups: 74 to 149μm, 44 to 74μm, and 44μm or less. The portion containing particles 44μm or less was further divided by elutriation into 5 groups: 30 to 44, 20 to 30, 01 to 20, 5 to 10 and 5μm or less. These 7 groups were used as the quartzite.

The examination of mineral compositions by power X-ray diffraction analysis showed that the Korean kaolin contained mostly metahalloysite, and traces of clay-like mica, quartz and plagioclase. The Indian feldspar contained mainly potassium feldspar with a little soda feldspar as a solid solution; quartz was the only component of the quartzite. **Table 1** shows the results of the chemical analysis of these materials and **Figure1** shows the grain size distributions measured by a sedimentatous method. Grain sizes of 20μm or less constituted 96% or more of the kaolin, and the mean grain size of the feldspar was 13μm. All distribution ranges were small.

The kaolin, feldspar and quartz were mixed in the standard ratio for porcelain bodies: 50 to 25 to 25wt% to produce 7 samples using the 7 groups of powdered quartz. To prevent the quartz grain size from changing, each mixture was heated while being stirred in distilled water, then solidified by evaporation, dried and crushed gently in an agate mortar. Each powder was preliminarily molded into square rods 5×5×40mm in bakelite lined molds under the pressure of 300kgf/cm² (1kgf/cm² = 9.8×10⁴Pa) using a single-shaft hydraulic press, and then hydrostatically molded under a pressure of 800kgf/cm². The compacts were placed in an electric furnace, heated at rate of 6°C/min, and fired at a temperature between 1200° to 1400°C (50°C intervals) for 1h and then cooled.

3. Test Results

3.1. Bulk Density

To determine the solidification due to firing, the bulk densities of the fired specimens were measured by a mercury substitution method. Each final value was the mean of 4 measurements. **Figure 2** shows the results of the bulk density measurements. The higher the firing temperature and the smaller the quartz grain size, the higher the density of the fired specimens. However, at temperatures above 1300°C, densities are lower for grain sizes 5 to 10μm and 5μm or less; at temperatures above 1350°C for grain sizes 10 to 20, 20 to 30 and 30 to 44μm, the densities are low. For grain sizes 44 to 74μm and larger, the density con-
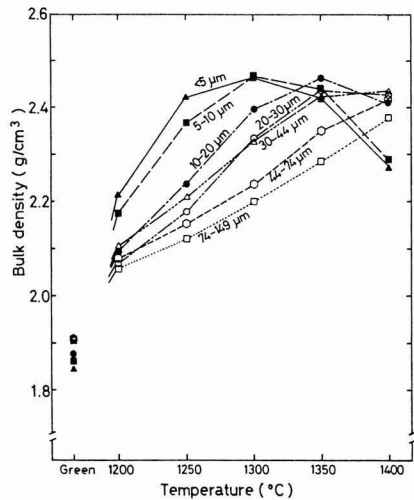

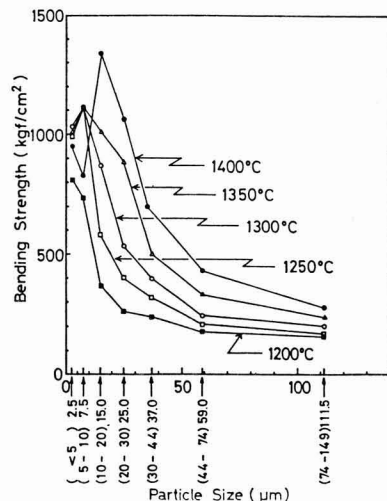**Fig. 2.** Bulk density of green and fired specimens.

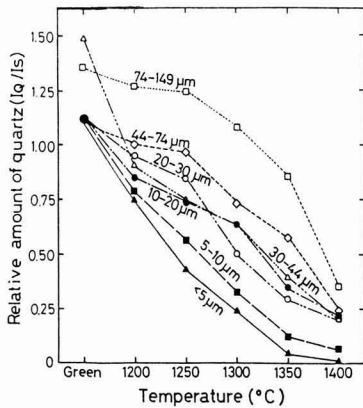**Fig. 3.** Bending strength of fired bodies vs. grain size of quartz.

Fig. 4. Relative amount of quartz in fired body vs. firing temperature.
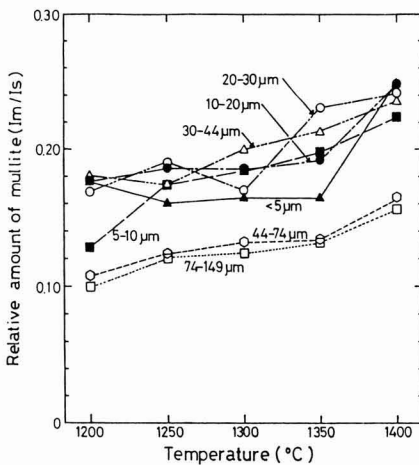

Fig. 5. Relative amount of mullite in fired body vs. firing temperature.

tinuously increases with increasing temperature up to 1400°C. The maximum bulk density slightly declines as the grain size of the sample group increases, but differences are very small.

3.2. Bending Strength

The bending strength of each specimen was measured using a 3-point loading method with a span of 20mm and a crosshead speed of 0.1mm/min. **Figure 3** shows the mean values of 10 measurements. Generally, the higher the firing temperature, the higher the bending strength. Due to the effect of the quartz grain size, the bending strengths, after the maxima, decease rapidly as the grain size increases. The higher the firing temperature, the larger the grain size at which the bending strength reaches a maximum. The samples 10 to 20μm fired at 1400°C, 5 to 10μm fired between 1250° and 1350°C, and 5μm or less fired at 1200°C exhibited maximum strengths. The maximum mean strength obtained in the present test was 1350kgf/cm² for the sample with a grain size of 10 to 20μm, fired at 1400°C.

3.3. Microstructure of Fired Specimens

To study the microstructures of the fired specimens, we investigated the relative changes in the component crystal phases using powder X-ray diffraction analysis. Using metallic silicon as an internal standard in the powdered samples, the relative intensities of the diffraction lines of quartz (100) and mullite (110) were calculated against the reference diffraction line of silicon (111). The results are shown in **Figures4** and **5**. The higher the firing temperature and the smaller the quartz grain size, the lower was the residual quartz content in the specimens. For specimens with a grain size of 10μm or less, and fired at 1400°C for 1h, almost no traces of the quartz remained. As the firing temperature increases, the amount of mullite produced increased. The mullite formation was also related to the quartz grain size: As the quartz grain size increased, the mullite formation at first increased, but then deceased for quartz grain size ranges larger than 44μm.

The determine the residual strains of quartz grains in the specimens, we examined the surfaces of the fired specimens and calculated the lattice distance of quartz (211) using the diffraction line of metallic silicon (311) as an internal standard, via the method previously reported.[1] The results are shown in **Figure6**. The $d_{(211)}$ values were larger than the normal value 1.541A. For quartz grain sizes below 5μm, the d values scarcely varied with the firing temperature. Maximum d values were observed in the specimens with grain sizes of 5 to 10μm fired at 1250°C, and 10 to 20μm fired at 1350°C; in the other specimens, d values increased as the firing temperature rose to 1400°C. In the temperature range below 1300°C, the specimens with grain sizes 5μm or less and 5 to 10μm exhibited maxima. Generally, the smaller the quartz grain size, the larger the $d_{(211)}$ value. Thus, the residual tensile strains of the quartz particles, and ultimately the level of the compressive stresses acting on the surrounding vitreous phase, depend on the size of the quartz grains and the firing temperatures.

We observed thin section of the fired specimens under a polarization microscope as well as the polished and HF etched surfaces of the samples using an SEM. Feldspar
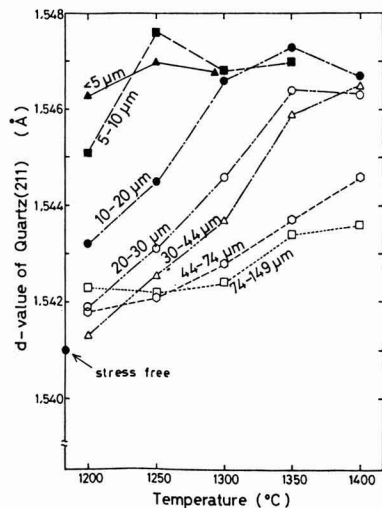

Fig. 6. $d_{(211)}$ of quartz in fired bodies vs. firing temperature.

completely melted during firing at 1300°C, and the produced glass spread throughout the matrix. The quartz grains were rounded due to corner melting. At 1400°C, most of the quartz grains 10μm or less melted, and the specimens exhibited large pores. In the specimens containing coarse quartz grains, areas around and through the quartz grains were cracked as shown in **Figure7**.

4. Discussion

Let's review the results obtained above in relation to the strength of the fired products. The relationship between the bulk densities and the mean bending strengths of the fired specimens are shown in **Figure8**. Almost no regularities were observed as would ordinarily be true with porcelain bodies.[13] However, if the data is divided into the different quartz grain size groups, it is evident that as the bulk density increases, the strength also increases. At the same density, the smaller the grain size, the higher the strength, and as the density increases, the more prominently the strength increases. As just mentioned, the higher the bulk density, the higher the strength of the fired product; however the effect of the quartz grain size on strength is greater. With coarse grains, the strength increase is only moderate as the density

increases because the samples are cracked in and around the quartz particles as observed microscopically. With grain sizes below 10μm, the strength ceases to increase as the bulk density rises over 2.4g/cm³. This is related to the melting of most of the quartz particles.

Figures 9 and **10** show the relationships between the bending strength and the residual quartz content and the quantity of produced mullite. As mentioned earlier, there was no regular relationship between the residual quartz content and the strength. However, if the data is divided into groups by grain size, one sees that the higher the content of residual quartz particles 10μm or larger, the lower the strength. Also, the larger the grain size, the lower the strength. With grain sizes below 10μm, the effect of the quartz content is small, but the strength relationship does exhibit a maximum at an identifiable level of the residual quartz content. This indicates that although the strength is decreased by cracks when the concentration of coarse particles is high, a concentration of quartz with suitable grain sizes exists which results in a favorable prestress effect which is effective in increasing the strength of specimens.

No regular relationships were found between the strength and the level of produced mullite, but if the data are classified according to quartz grain sizes, it was roughly ob-
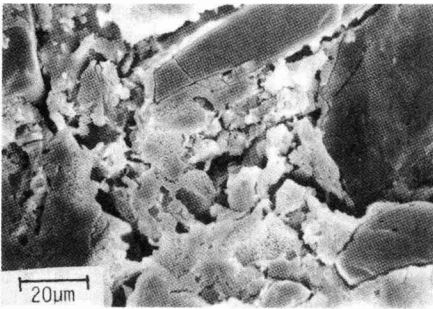

Fig. 7. A scanning electromicrograph of specimen added with coarse quartz grain and fired at 1300°C.
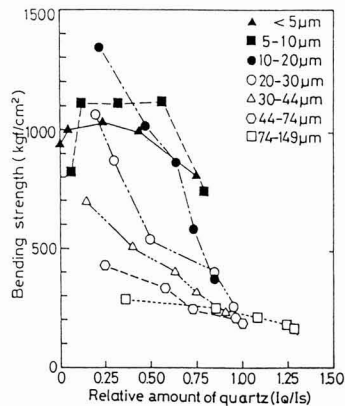

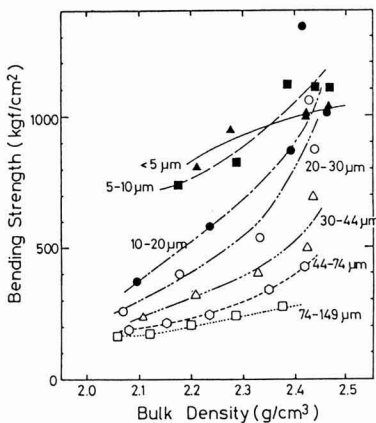**Fig. 9.** Relation between bending strength and amount of residual quartz in fired body.

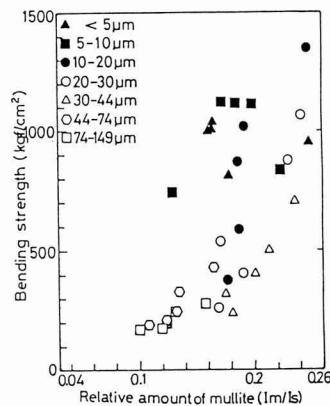**Fig. 8.** Relation between bending strength and bulk density of fired body.

Fig. 10. Relation between bending strength and mullite content in fired body.
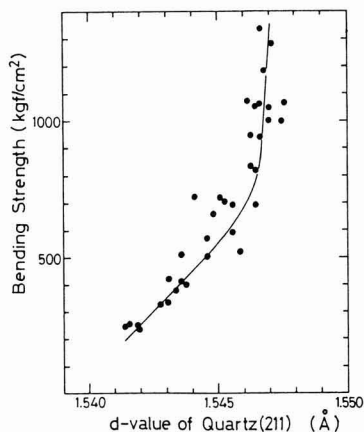
Fig. 11. Relation between bending strength and $d_{(211)}$ of quartz in fired body.

served that the higher the mullite concentration, the higher the strength. However, since a small quartz grain size implies a higher strength, it could be concluded that the effect of the mullite level was also influenced by the quartz grain size.

As described earlier, the lattice distances of the residual quartz particles in the specimens were larger than the normal values, and the residual quartz particles were subjected to a tensile strength. **Figure 11** shows the relationship between the lattice distance $d_{(211)}$ of quartz and the bending strength. Similar to the results previously reported, the lattice distances were large and, the higher the compressive stresses acting on the vitreous phase around the quartz particles, the higher the mechanical strength. The mechanical strength peak at around 1.547A, at which point the strength seems to be greatly affected by other factors.

The above results indicated that, although it was somewhat effected by mullite content, the strength of porcelain bodies was mainly governed by the level of compressive prestresses caused in the vitreous phase around the quartz particles, which are believed to be effected by the grain size of the added quartz and the firing conditions. Marzahl proposed a formula to describe the relationship between the strength of porcelain bodies and the grain size of the quartz, however it is difficult to apply to porcelain bodies in which the particle shapes and the vitreous phase are not even. However, his results indicated that there is an optimal grain size range, which we confirmed. If the grain size of the added quartz was too large, the nitreous phase were cracked. If the grain size was too small, the quartz particles melt too easily. In both cases, the strength of bodies was reduced. Thus, there should be a grain size range which permits a maximum strength to be attained, and it will depend on the firing temperature. We found that the optimal grain size ranges were 10 to 20μm at 1400°C, 5 to 10μm at 1350° to 1250°C, and 5μm or below at 1200°C firing.

5. Conclusion

Using 7 grainsized quartz particles with narrow grain size

distributions, we prepared kaolin-based standard-composition porcelain bodies, and fired them at temperatures 1200° to 1400°C for 1h. We measured the bulk densities, the contents of constituent phases, and changes in the lattice distances of the quartz in the fired bodies, and observed the microstructures in order to study the effects of these factors on the bending strengths of the products.

Generally, the higher the bulk density of the fired products, the higher the strength, but the grain size of the added quartz was influential. For specimens containing coarse quartz particles, areas in and around the quartz particles in the bodies were cracked, and the strength of the bodies increased only slightly as the bulk density increased. For such specimens, the higher the residual quartz content after firing, the lower the strength.

The higher the tensile strains of the residual quartz in the fired bodies, and the higher the compressive stresses in the vitreous phase around the quartz particles, the higher the mechanical strength of the bodies. To effect suitable compressive prestresses to the vitreous phase, the added quartz particles should not be too fine or too coarse, but within a certain size range relative to the firing temperature. In the present test, such ranges were 10 to 20μm for a firing temperature of 1400°C, 5 to 10μm at 1350° to 1250°C, and 5μm or less at 1200°C. If the grain size of the quartz was within a suitable range to result in a favorable prestress effect, the remaining quartz contributed to increases strength of the bodies. There might be some tendency that the higher the mullite content, the higher the strength, but this effect was also influenced by the grain size of the added quartz.

(This paper represents results reported to the annual meeting in May, 1984 and additional new work.)

References:
1) K. Hamano and E.S. Lee, Mechanical Behavior of Materials, Proceedings of the 1971 International Conference on Mechanical Behavior of Materials, The Society of Materials Science, Japan, Vol.IV, 475-483 (1972).
2) H. Marzahl, Ber. Deut. Keram. Ges., 32, 203-11 (1955).
3) L. Mattyasovszky-zsolnay, J. Am. Ceram. Soc., 40, 299-306 (1957).
4) L. Stuckert and O. Paul, Ber. Deut. Keram. Ges., 21, 150-67; 171-200 (1940).
5) O. Krause, Sprech., 75, [23/24, 25/26, 27/28] (1942).
6) D. Weyl, Ber. Deut. Keram. Ges., 36, 319-24 (1959).
7) L. Berens, Tonindustr. ztg., 85, 54 (1961).
8) T. Wiedmann, Sprech., 92, 2-5 (1959).
9) A. Palatzky, Silikattechnik, 9, 68-73 (1958).
10) R. Rieke and W. Schade, Ber. Deut. Keram. Ges., 11, 427-42 (1930).
11) P.P. Budnikov, "Technologie der Keramischen Erzeugnisse ein Schlietzlich der feuerfesten Baustoffe". VEB. Verlag Technik, Berlin, (1953).
12) R. Masson, Keram. Z., 9, 110-12 (1957).
13) K. Hamano and E.S. Lee, Bull. Tokyo Inst. Tech., 108, 95-1211 (1972).

Ferroelectric Pb(Mg, Nb)O₃ Ceramics with Various Mg/Nb Ratios

Shigeru Tanaka, Yasuo Matsushita and Kunihiro Maeda

Hitachi Research Laboratory, Hitachi Ltd.,

3-1-1, Saiwai-cho, Hitachi-shi 317, Japan

The dielectric properties of Pb(Mg, Nb)O₃ ceramics with various B-site ratios (Mg/Nb = M/N ratio) were investigated. With changing M/N ratio from 0.30 to 1.00 (stoichiometric ratio = 0.50), the dielectric constant changed largely. Particularly, it showed the maximum of 20000 at Tc at a non-stoichiometric ratio (M/N) of 0.66. The resistivity ρ, tan δ and Tc were a most independent of the M/N ratio.

Crystal phase analysis, in the case of small M/N ratio (0.3) showed that the main phase was pyrochlore with low dielectric constant. Samples with M/N ratios higher than the stoichiometric one had a perovskite phase. Moreover, it was observed that the lattice constant at M/N ratio = 0.66 was larger than that of the stoichiometric one. The change of dielectric constant seems to be associated with the crystal structure and the lattice constant.

1. Introduction

Recently, electronic devices have become markedly more compact and more functional; these trends also include common electronic parts, such as condensers. In particular, high-capacity ceramic condensers are increasingly in demand, being more functional than characteristics, such as non-polarity and high weather resistance. Lead-base perovskite oxides (ABO₃ relaxor type) have been attracting attention over BaTiO₃ type ferroelectrics, for various reasons; e.g., they are sinterable at low temperatures (around 1000°C) lowering costs, and their Curie temperature shift and the temperature characteristics of their dielectric constants can be controlled by changing the combinations of B-site ion species.[1]

Pb(Mg₁/₃Nb₂/₃)₃(hereinafter referred to as PMN) is a representative lead-base ferroelectric, which has already been commercialized in the form of solid solutions with PbTiO₃, Pb(Zn₁/₃Nb₂/₃)O₃ or Pb(Mg₁/₂W₁/₂)O₃. The divalent Mg and pentavalent Nb in these compounds make the B-site tetravalent and electrically neutral when they are mixed in a Mg/Nb atomic ratio of 0.5. The B-site has been generally limited to the stoichiometric ratios that satisfy the electrically neutral condition, as mentioned above.

Wheeler,[2] however, proposed several new types of relaxors based on PMN structures with nonstoichiometric compositions Pb (Mg₁/₂ Nb₁/₂) O₃₋δ suggesting new composi-

tional possibilities. They attract attention in that non-stoichiometric compositions have not been investigated in detail. Their structures and properties, however, are still largely unknown. On the other hand, Furukawa et al.[3] have discussed the effects of MgO added excessively to control the formation of the pyrochlore phase during the PMN sintering process, and thereby to improve the dielectric properties of the sintering body. In this study, the ratio of Mg²⁺ to Nb⁵⁺ present in the B-site was varied to investigate their effects on the electrical properties and structures of these materials.

2. Experimental Procedure

2.1. Sample Preparation

Figure 1 illustrates the flow diagram of the sample preparation procedure. Starting materials were the oxide reagents (purity: 3N or higher, Rare Metallic). The ferroelectric powder was prepared by the Columbite method proposed by Swartz et al.[4,5] Specified quantities of MgO and Nb₂O₅ in the presence of ion-exchanged water were milled using resin balls for 16h; the mixed powder was then dried and calcined at 1000°C for 4h to produce magnesium niobate. A given quantity of PbO was added to the magnesium niobate powder and the mixture was ball-milled in the same manner as before, then dried. This mixed powder was placed into a MgO crucible equipped with a cap, and calcined in an electric oven (Siliconit Konetsu Kogyo), at 850°C for 4h, then crushed with ZrO₂ balls, to produce a powder of 1 to 3μm in particle size. An excessive quantity of PbO was added to the powder as the sintering aid.[6] The
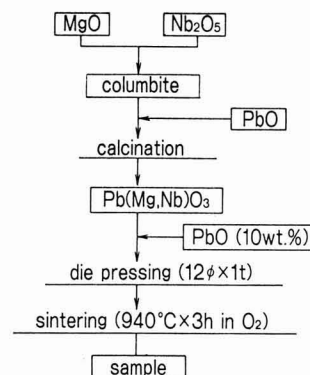
Fig. 1. Experimental Procedure

powder thus prepared was granulated and formed into a shape, which was embedded in a powder containing ZrO_2 as the major ingredient, and sintered in a flow of oxygen gas (300ml/min). Use of the oxygen atmosphere was to keep oxygen partial pressure in the atmosphere gas, to control variations in valence of the constituent ions and thereby prevent fluctuations in the sample characteristics. The electric oven used for this sintering process was supplied by Nishimura Kogyo (T-61310). The disc-shape sintering body thus prepared was polished and then sputtered with Au-Pd to provide electrodes on the surfaces. The ohmic connection between the ceramic and the electrodes was confirmed by measuring the V-I characteristics.

2.2. Characterization

2.2.1. Quantitative Analysis

The synthesized compositions were quantitatively analyzed for Mg, Nb, and Pb by the ICP luminescence method.

2.2.2. Resistivity

A DC voltage of 50V was applied between the electrodes on the sample to measure insulating resistance R from the amperage detected after 2 min; the insulating resistivity ρ was determined from the resistance R, the electrode area and the sample thickness. The measurement conditions were $24\pm2°C$ and $50\pm5\%$ RH.

2.2.3. Dielectric Constant and Dielectric Loss

An impedance analyzer (YHP, 4192A) was used to determine the capacitance, C and the dielectric loss, tan-δ of the sample, at a measurement frequency of 1kHz. The dielectric constant, ε, was calculated from the following relationship:

$$\varepsilon = C \cdot d / (\varepsilon_0 \cdot S) \quad \ldots \ldots \ldots \ldots \ldots \ldots (1)$$

where,

S: electrode area

d: the sample thickness (distance between the electrodes)

ε_0: the dielectric constant under vacuum

Furthermore, each sample was placed in a constant-temperature bath (Daiwa Giken, DC-202), to measure the temperature-characteristics of the dielectric constant and the dielectric loss in a range between $-40°$ and $120°C$.

2.2.4. Identification and Analysis of Crystalline Phases

The produced crystalline phases were identified by X-ray diffraction analysis. The sample was crushed to 10μm or less and attached to a glass holder. The X-ray diffrac-

tometer (Rigaku Denki RU-200), with a Cu target, was operated at 40kV and 100mA. In addition, a scanning electron microscope (SEM, Hitachi, E-102) and an energy dispersion type X-ray analyzer (EDX, Horiba Seisakusho, EMAX-2200) were used to observe and conduct the elemental analysis of the samples.

3. Results and Discussion

3.1. Electrical Properties

The prepared sample was chemically analyzed to determine its composition prior to its electrical properties being measured. The results are given in **Table 1**, where each molecular formula shown in the table was estimated from the quantitative analysis results of the constituent elements, assuming that sum of the B-site elements was unity. This assumption was based on the properties of MgO and Nb_2O_5: They melt at sufficiently high temperatures (MgO: $2800°C$, Nb_2O_5: $1510°C$) and so rarely evaporate during the production process; in addition, it is difficult for them to go into A-sites while maintaining the perovskite structure, because their ionic radii (about 0.7Å) are roughly half that of Pb. M/N in the table represents the Mg/Nb ratio in each formula. It is difficult to accurately judge whether Samples No.2 and 3 were stoichiometric compositions or not, due to their deficiency in Pb. However, the other samples were certainly non-stoichiometric, given that the stoichiometric B-site is represented by an M/N ratio of 0.5. Evaporation of Pb could be controlled by adequately devising the process system. The observed stoichiometric ratio of M/N = 0.5 was in good agreement with the literature value, as will be discussed later; thus, the B-site will primarily be discussed in this study.

Figure 2 shows the effects of the M/N ratio on the dielectric constant of each sample at room temperature. The dielectric constant, ε, varied with the M/N ratio, rapidly decreasing below 2000 when the M/N ratio was below the stoichiometric level. A dielectric constant of 14000 at M/N = 0.5 was in agreement with that previously reported.[7] It attained a maximum at M/N = 0.66, higher by roughly 2000 than the value at the stoichiometric composition (M/N = 0.5). Increasing the M/N ratio further decreased the

Table 1. The Results of Quantitative Analysis of $Pb(Mg, Nb)O_3$ samples.

sample No.	element (wt.%)			estimated formula	M/N
	Pb	Mg	Nb		
1	63.0	1.5	19.4	$Pb_{1.13} (Mg_{0.23}Nb_{0.77}) O_{3.29}$	0.3
2	60.0	2.7	20.8	$Pb_{0.86} (Mg_{0.33}Nb_{0.67}) O_{2.84}$	0.5
3	61.0	3.3	19.2	$Pb_{0.87} (Mg_{0.4} Nb_{0.6}) O_{2.77}$	0.66
4	59.6	4.9	18.5	$Pb_{0.72} (Mg_{0.5} Nb_{0.5}) O_{2.5}$	1.0
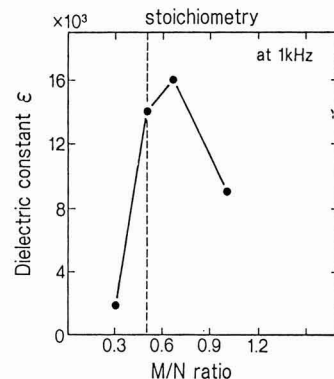
Fig. 2. Dielectric constant of $Pb(Mg, Nb)O_3$ ceramics for various M/N ratio (at R.T)

dielectric constant. **Figure 3** shows the effects of tempera-
ture on the dielectric constant and the dielectric loss, tan δ.
The dielectric constant at the non-stoichiometric M/N ratio
of 0.66 was higher than that at the stoichiometric ratio over
the entire range of temperatures tested. The samples with
an M/N ratio of 0.5 or more had an almost constant Curie
temperature of 0°C. The tan δ level was substantially dif-
ferent above and below the Curie temperature; 8 to 10% for
temperatures below the Curie temperature, and 0.2 to 0.3%
above the Curie temperature. This trend was common to
the three samples with different M/N ratios (0.66, 0.5 and
1.0). The dielectric constant of the sample with M/N = 0.33
was much lower than that of any of the above three samples,
and its tan δ was also different ranging between 2 to 6%.

Figure 4 shows the effects of the M/N ratio on the resis-

tivity ρ. As shown, the resistivity was essentially constant
at $1 \times 10^{11} \Omega\tilde{A}m$, irrespective of the M/N ratio. It had been
anticipated that by varying the M/N ratio, the electrically
neutral conditions would collapse to decrease the resistivity
by traps being formed in the crystal; however, such a trend
was not observed. This conceivably resulted from balanced
positive and negative charges - cations vs anions, to keep
the resistivity high. Of the samples prepared in this study,
the one having an M/N ratio of 0.66 (higher than the
stoichiometric ratio of 0.5) had a high dielectric constant, a
low dielectric loss, and a high insulation resistivity; thus it
was best suited as a material for ceramic condensers.

As discussed above, a PMN composition with good
electrical properties has been found, which is different from
the conventional composition in that it has an non-
stoichiometric M/N ratio. Its structure was investigated to
correlate it with its electrical properties.

3.2. Investigation of Structures

Figure 5 shows the X-ray diffraction analysis results.
The sample with M/N = 0.3 had a low perovskite phase
intensity, and the pyrochlore phase predominated in the
structure. The perovskite phase formation rate, R_{pero}, was
estimated from the following relationship, using the peak
intensity I of the most intensive peak of each phase for
convenience:

$$R_{pero} = I_{pero}/(I_{pero} + I_{pyro}) \times 100(\%) \quad \ldots \ldots (2)$$

The calculated formation rate was around 10%. The
pyrochlore phase generally has adverse effects on the
dielectric properties of perovskite type ferroelectrics, and
the low dielectric constant levels for M/N=0.3 shown in
Fig.2 and 3 were considered to result from the formation of
the pyrochlore phase. The columbite synthesis method,
used in this study, depended on the following reactions:[3]

$$MgO + Nb_2O_5 \rightarrow MgNb_2O_6 \quad \ldots \ldots \ldots (a)$$

$$3PbO + MgNb_2O_6 \rightarrow 3Pb(Mg_{1/3}Nb_{2/3})O_3 \quad \ldots (b)$$
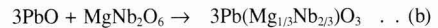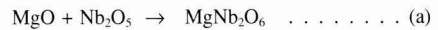
The above reactions are for the formation of the
stoichiometric composition. For the composition with M/N
= 0.3, excessive Nb_2O_5 was present in step (a), with the
result that it reacted preferentially with PbO in step (b) to
produce lead niobate, which served as the nucleus for for-
mation of the pyrochlore phase. This accounted for the
presence of a large quantity of the pyrochlore phase in the

Fig. 3. Dielectric constant and loss vs temperature for Pb(Mg, Nb)O₃ ceramics

Fig. 4. Resistivity of Pb(Mg, Nb)O₃ ceramics for various M/N ratio (measured at 2min after applying DC 50V)

Fig. 5. X-ray diffraction patterns of Pb(Mg, Nb)O₃ ceramics

sintered sample. Sample No.1 had a larger quantity of Pb than the others, as shown in Table 1; this conceivably resulted from the formation of lead niobate at 500° to 700°C which prevented the removal of Pb.[5]

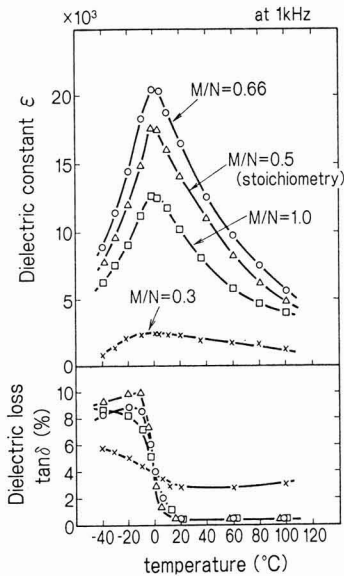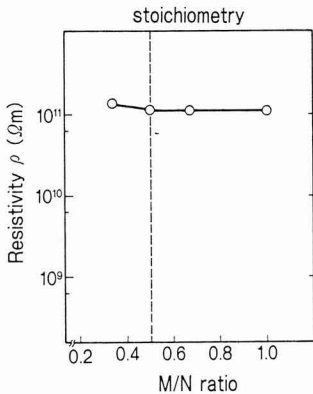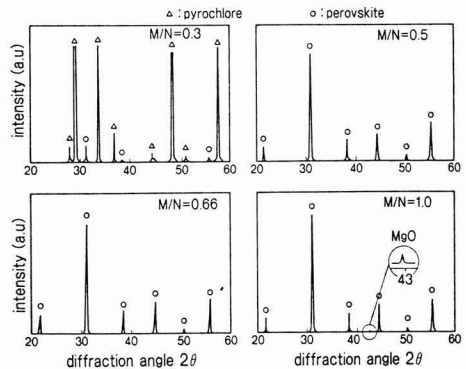On the other hand, the samples having a stoichiometric or higher M/N ratio consisted of the perovskite phase only; no pyrochlore phase was detected. The sample with M/N = 1.0, however, exhibited a peak around $2\theta=43°$ indicating the presence of MgO (with a low dielectric constant of = 3).

Figure 6 presents the SEM photographs of the fractured faces. The sample with M/N = 0.3, having the main phase of pyrochlore consisted of fine particles around 1μm in size, with essentially no grain growth observed. On the other hand, particles grew to 5μm or more in samples with M/N = 0.5 and 0.66. Furthermore, the sample with M/N = 1.0 was characterized by an uneven structure, with fine grains of 1 to 2μm (B) separating out inside the main grains (A) and at their grain boundaries. **Figure 7** shows the compositions of the main and small grains, point-analyzed by EDX. Each grain consisted of Pb, Nb, and Mg, the patterns of which greatly differed in the main and small grains; the latter grain was characterized by the Mg-rich composition. Significantly changing the M/N ratio from the stoichiometric ratio in such a way as to reduce the quantity of Nb, caused Mg, which took no part in the perovskite formation process, to be left in the system. The presence of this Mg-rich phase might be one of the reasons for the decrease in the dielectric constant. The sample with M/N = 0.66 was similar in structure and X-ray intensity, to the sample with M/N = 0.5 (stoichiometric ratio), thus the maximum dielectric constant exhibited by the M/N = 0.66 sample could not be explained by differences in the crystalline phase or structure of sintering body.

The length of the unit lattice as a function of the M/N ratio was investigated in an attempt to explain the presence of the maximum dielectric constant. **Figure 8** shows the unit lattice length (lattice constant,Å for each sample, based on X-ray diffraction results of each sample (M/N ≥ 0.5) processed by the leastsquare method. A length of 4.04 for the stoichiometric ratio (M/N = 0.5) was in good agreement with the literature level of 4.041.[7] The sample with M/N = 0.66 was characterized by a larger lattice constant than that of the sample with the stoichiometric M/N ratio, indicating an expansion of the lattice as a whole. This conceivably resulted from a changed B-site composition. From the chemical formulae shown in Table 1, the estimated valence of the B-site was +3.8 at M/N = 0.66, versus +4.0 at M/N = 0.5, given that the valences of Mg and Nb are +2 and +5, respectively. On the other hand, the quantities of Pb were almost the same in the A-sites of these samples, but the quantity of oxygen ions was smaller in the sample with M/N=0.66. Therefore, it is believed that the reduced quantity of charges in the B-sites of the sample with M/N = 0.66 reduced the electronic attraction for oxygen ions, thereby expanding its atomic distance, with the result that the lattice became more polarized increasing the dielectric constant of the sample. As discussed above, there seems to be a correlation between the length of the perovskite unit lattice and the electrical properties of the material. The sample with M/N = 1.0 had an even smaller B-site valence, but the quantity of Pb ions in its A-sites was also reduced, such that the expansion of the lattice was controlled, resulting in a unit lattice shorter than that for the sample with M/N = 0.66. Moreover, the above-mentioned Mg-rich phase was formed in this sample, resulting in a dielectric constant lower than that for the stoichiometric composition.

main grain (A)   small grain (B)

Fig. 7. Result of EDX analysis for Pb(Mg, Nb)O₃ (M/N = 1.0)

M/N=0.33   M/N=0.5

M/N=0.66   M/N=1.0

Fig. 6. SEM micrographs of fractured surface of Pb(Mg, Nb)O₃ ceramics
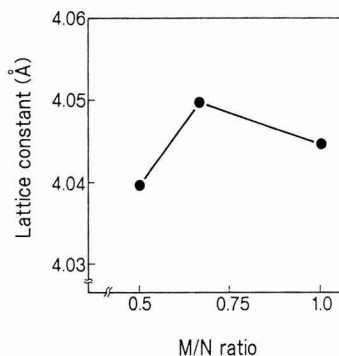
Fig. 8. Lattice constant of Pb(Mg, Nb)O₃ for various M/N ratio

4. Conclusions

1) A new Pb(Mg, Nb)O$_3$-based ferroelectric ceramic has been developed by changing the B-site composition from the conventional stoichiometric Mg^{2+}/Nb^{5+}(M/N) ratio of 0.5.
2) The dielectric constant of the nonstoichiometric composition changed with M/N ratio, and the composition with M/N = 0.66 exhibited a dielectric constant of 20000, which was higher than that of the stoichiometric composition (M/N = 0.5). It was, in fact, the maximum dielectric constant; the dielectric constants of the other compositions were below the above level.
3) When M/N was above the stoichiometric ratio of 0.5, the composition consisted essentially of the perovskite phase, although in the composition with M/N=1.0, the formation of Mg-rich phase was observed. The pyrochlore phase predominated, instead of the perovskite phase, when the M/N ratio was below the stoichiometric ratio.
4) It was concluded that the ferroelectric properties of the Pb(Mg, Nb)O$_3$ composition were affected not only by the crystalline phase but also by the length of the perovskite unit lattice.

(These results were presented to the Ceramic Basic Seminar, held in January, 1990)

References:
1) M. Harada, J. Electronic Information Communications Society of Japan, 70, No.1, 109-112, (1987).
2) J. M. Wheeler, U.S. Patent 4,525,768.
3) K. Furukawa, S. Fujiwara, and T. Ogasawara, The Japan-U.S. Study Seminar on Dielectric and Piezoelectric Ceramics, T-4, 1-5, (1982).
4) S. L. Swartz, T. R. Shrout, W. A. Schulze, and L. E. Cross, J. Am. Ceram. Soc., 67, 311-315, (1984).
5) S. L. Swartz and T. R. Shrout, Mat. Res. Bull., Vol.17, 1245-1250, (1982).
6) M. S. Chu and C. E. Hodgkins, Extended Abstracts American Ceramic Society 87th Annual Meeting, 111, May, (1985).
7) Landolt-Bornstein, "Ferroelectrics and Related Substances," Vol.16, Springer-Verlag Berlin Heidelberg New York (1981).

Complex-Impedance Analysis of Unusual Dielectric Properties in (Pb, La)TiO$_3$ Ceramics

Koji Goda and Makoto Kuwabara

Department of Applied Chemistry, Faculty of Engineering, Kyushu Institute of Technology
1-1, Sensui-cho, Tobata-ku, Kitakyushu-shi 804 Japan

Both an anomalous broad dielectric peak above the Curie temperature and a normal sharp dielectric peak at the Curie temperature were observed in Pb$_{1-x}$La$_{2x/3}$TiO$_3$ (X=0.05 to 0.20) ceramics. The broad dielectric peak shifted toward higher temperatures with increasing frequency, associated with a decrease in its peak value. The complex impedance loci consisting of two semicircles were found for the materials above the Curie temperature indicating that the dielectric property can be analyzed using an equivalent circuit with a series connection of two RC parallel circuits. The origin of the broad peak has been tentatively interpreted to be an interfacial polarization at the grain boundaries.
[Received October 18, 1990, Accepted October 26, 1990]

1. Introduction

PbTiO$_3$ ceramics exhibit a high anisotropy of electromechanical coupling factors and a low permittivity, which make them useful as piezoelectric and pyroelectric materials. Having a high Curie point, about 490˚C, pure PbTiO$_3$ is a possible candidate for high-temperature use. In this regard, we have been studying the relationship between the dielectric and piezoelectric properties and the microstructures of ceramics composed of (Pb, La)TiO$_3$ mixed with MnO$_2$ (hereinafter referred to as "PLT ceramics").[1] We recently reported that in the temperature dependence of the dielectric constant, a broad dielectric peak, which showed a relaxed dispersion highly frequency dependent, was observed above the Curie temperature besides a normal sharp peak due to a tetragonal-cubic phase transition at the Curie temperature[2].

These broad dielectric peaks exhibiting relaxed dispersions are observed in most perovskite oxides. Near the phase transition, the dielectric constants of BaTiO$_3$-BaSnO$_3$ solid solutions and of irregularly oriented complex perovskites (such as Pb(Mg$_{1/3}$Nb$_{2/3}$)O$_3$) are highly frequency dependent.[3] This trend is ascribed to composition changes, secondary and further phase transitions or thermal agitation of spontaneous dipole polarization in the region of micropolarization.[4-6] Similar dielectric peaks showing large frequency dispersions are also occasionally observed in irregularly oriented perovskites lacking dielectric peaks due to phase transitions (such as (K$_{3/4}$ Bi$_{1/4}$)(Zn$_{1/5}$ Nb$_{5/6}$)O$_3$); this is ascribed to minimum potential points caused in each perovskite cell by low symmetric strains due to irregular ion orientation.[7] It has also been reported that the dielectric

constants of such oxides as ZrO$_2$,[8] Y$_2$O$_3$,[9] and ferrite,[10] which differ in crystal structure from the perovskites, show a prominent frequency dependence which can be explained by interfacial polarization.

The temperature dependence of the dielectric properties of PbTiO$_3$ ceramics (including PLT) have been studied;[11,12] However, there have been no reports on dielectric peaks which show relaxed dispersions as observed in the present study. To discover the causes of this phenomenon, we investigated the frequency dependence of the dielectric constant-temperature properties of the PLT ceramics and analyzed the complex-impedance characteristics in detail.

2. Experimental Procedure

We obtained sintered discs of 0.99Pb$_{1-x}$ La$_{2x/3}$ TiO$_3$ + 0.01 MnO$_2$, where X = 0.05(PLT5), 0.10(PLT10), 0.15(PLT15), or 0.20(PLT20), by using a conventional method of solid-state reaction as follows:

As starting materials, we used PbTiO(C$_2$O$_4$)$_2$ 4H$_2$O, (purity;$^+$99.9%, Central Glass Co., Ltd.) and La$_2$O$_3$, TiO$_2$, MnO$_2$ (Kojundo Kagaku Co., Ltd.) Required quantities of these materials were accurately, weighed, and the mixture was wet milled and kneaded both for 48hr in ethanol using zirconia balls in a polyethylene container. The products were then calcined at 800˚C for 3hr, wet ball milled again for 48hr in the same way, dried and sieved under 75μm. The powders thus obtained were molded in a rubber press under 5000kg/cm^2 and sintered at 1225˚C for 10hr.

The sintered products were cut into disks about 7mm in diameter and about 0.7mm thick; silver paste electrodes were painted and fired on both sides of them and the dielectric constants, the dissipation factors and the complex impedance were measured within a temperature range from room temperature to 600˚C using an infrared image furnace and a vector impedance meter (YHP - 4192A).

To examine the microstructure of the sintered products, we observed the fracture surfaces of the samples under an SEM.

Lattice constants were determined via the Cohen method from the measured CuKα diffraction lines of the (101), (110), (111), (002), (200), (211), (202), (220) planes of the polished samples.[13]

3. Results and Discussion

Table 1 shows the relative densities and lattice constants of the samples; when the La content exceeded 10mol%(x=0.10), the relative densities rapidly decreased

Table 1. Specifications of samples prepared in this study.

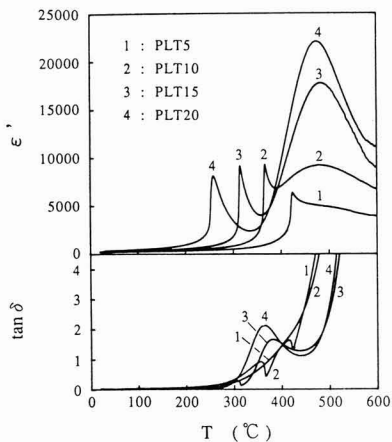| Sample	Relative sintered density (%)	Lattice constant (Å)	
		a	c
PLT5	98.5	3.910	4.081
PLT10	95.8	3.914	4.057
PLT15	92.3	3.916	4.030
PLT20	93.3	3.919	4.005

Fig. 1. Plots of dielectric constant (ε') and dissipation factor (tan δ) measured at 1kHz as functions of temperature.

resulting in relative densities for PLT15 and PLT20 of about 92 to 93%. As the La content increased, the lattice constant a slightly increased and the lattice constant c significantly decreased. Lattice constants a and c were observed to change linearly with the La content, which agreed with the results of Ito, et al.[14] The X-ray powder diffraction analysis showed that the samples were composed of a single perovskite phase, and the results of the lattice constant measurement suggested that La was substituted in PbTiO₃.

Figure 1 shows the temperature characteristics of the dielectric constant and the dissipation factors measured at 1kHz for PLT5, PLT10, PLT15, and PLT20. All samples showed broad peaks (BP) above the Curie temperature in addition to the sharp normal peaks (NP) observed at the Curie temperature due to the tetragonal-cubic phase transformation. While the peak valves of NP showed little or no La concentration dependence, the peak valves of BP prominently increased with La content.

Figure 2 shows the temperature characteristics of the dielectric constant measured at 0.1, 1, 10, 100 and 1000kHz for PLT5 and PLT20. The peak temperature of NP showed little frequency dependence and the peak value slightly decreased with increasing in frequency. The peak temperature of BP, on the other hand, shifted toward highly temperature with frequency, associated with a decrease in its peak value. At measurement frequencies of 1MHz or above, no BPs were observed in the temperature range from R.T. to 600°C.

We measured the complex impedances of PLT5 and PLT20 at 500°C (corresponding to the large BP), and **Figure 3** shows the Cole-Cole plots indicated by solid lines. For

both PLT5 and PLT20, each plotted line was composed of two semicircles. This implied that the equivalent electrical circuit of each sample could be represented by a circuit composed of two parallel RC circuits coupled in series as shown in **Figure 4**.[5] If $\tau_1(=R_1C_1) < \tau_2(=R_2C_2)$, the R_1C_1 and R_2C_2 components make semicircles on the high and low frequency sides respectively. Using values of $R_1 = 3.70 \times 10^3\Omega$, $C_1 = 9.86 \times 10^{-10}$F, $R_2 = 5.95 \times 10^3\Omega$ and $C_2 = 5.19 \times 10^{-9}$F for PLT5, and $R_1 = 1.59 \times 10^3\Omega$, $C_1 = 3.01 \times 10^{-10}$F, $R_2 = 3.90 \times 10^3\Omega$ and $C_2 = 1.82 \times 10^{-8}$F for PLT20, we calculated the complex impedances of the circuit in Fig.4 and Fig. 3 shows the Cole-Cole plots of the calculated results indicated by dotted line. For both PLT5 and PLT20, the measured values (solid lines) were in good agreement with the calculated results (dotted lines). For both PLT5 and PLT20, the semicircles (R_1C_1) and (R_2C_2) on the high and low frequency sides respectively, showed multi-relaxation below the Curie temperature, preventing us from simulating the measured values of complex impedance by the equivalent electrical circuit. For PLT15 and PLT20, on the other hand, the Curie points were so low that R_1 and R_2 in
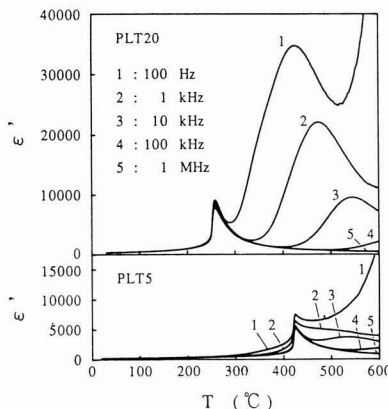

Fig. 2. Temperature dependence of dielectric constant (ε') at various frequencies for samples PLT5 and PLT20.
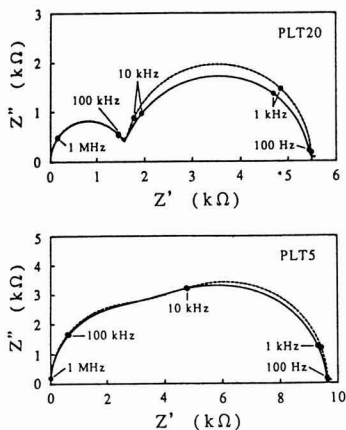

Fig. 3. Impedance plots observed (solid lines) and calculated (dotted lines) from equation (1) using the data given by equations (5) to (8) for samples PLT5 (at 502.7°C) and PLT20 (at 503.0°C).
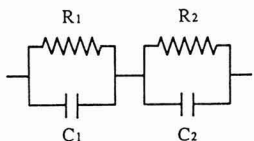
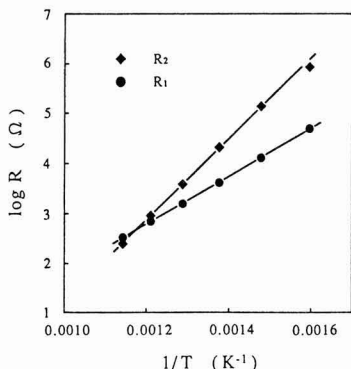**Fig. 4.** An equivalent circuit used for the complex impedance analysis.

Fig. 5. Plots of equivalent resistances R_1 and R_2 (in Fig.4) as functions of temperature for sample PLT20.

the ranges below the Curie temperature were extremely large, preventing us from obtaining two semicircles of complex impedance within the measurement frequency range. A more detailed analysis of complex impedance below the Curie temperature will be left for future discussion. For PLT20, which showed a large BP, we measured the complex impedances at temperatures 350° to 600°C, and obtained R_1, C_1, R_2 and C_2 values for circuit in Fig.4 in the same manner. The results are shown in **Figures5** and **6**. Between R_1 and R_2 and temperature T(K), we observed the same relations as for ordinary insulating and semiconducting ceramics: $\log R_1 \propto 1/T$ and $\log R_2 \propto 1/T$. C_1 conformed to Curie-Weiss' law: $1/C_1$, increased in proportion to temperature T. The relationship between C_2 and temperature, however, was not quite as definite, with C_2 deceasing as the temperature increased.

Figure 6 shows, along with C_1, the parallel capacitance C_p for the sample at 1MHz where BP didn't observed. C_p agreed completely with C_1. Since C_p of the sample measured at 1MHz exhibited thermal variations in capacitance (or dielectric constant) due to the tetragonal-cubic phase transformation at the Curie point, it was assumed that the R_1C_1 component shown in Fig.4 caused an NP representing the bulk electrical properties of the sample. It was, therefore, considered that the BP which showed relaxed dispersions were caused by the R_2C_2 component. In the Cole-Cole plot at 503.0°C for PLT20 shown in Fig.3, the measured points in the low-frequency range were on the semicircle represented by the R_2C_2 component (or more exactly, R_1 and R_2C_2 component coupled in series, i.e., the circuit excluding C_1 in Fig.4). As the frequency exceeded 100kHz, the data points lay on the semicircle represented by the R_1C_1 component. This implies that at 500°C, for frequencies above 100kHz, the R_2C_2 component is negligible, and corresponds to the absence of BP showing relaxed

dispersion, in the temperature characteristics of the dielectric constant above 100kHz for PLT20 shown in Fig. 2.

The complex impedance of the equivalent circuit in Fig.4 is given by

$$Z = \frac{R_1}{1 + \tau_1^2\omega^2} + \frac{R_2}{1 + \tau_2^2\omega^2} - j\left[\frac{R_1\tau_1\omega}{1 + \tau_1^2\omega^2} + \frac{R_2\tau_2\omega}{1 + \tau_2^2\omega^2}\right] \quad (1)$$

where $\omega(=2\pi f)$ is an angular frequency, with $\tau < \tau_2$. In a sufficiently low frequency range: $\tau_1\omega \sim 0$ (on the right hand semicircle in Fig.3), Equation (1) can be approximated as

$$Z = R_1 + \frac{R_2}{1 + \tau_2^2\omega^2} - j\frac{R_2\tau_2\omega}{1 + \tau_2^2\omega^2} \quad \cdots \cdots (2)$$

In other words, the locus of the semicircle on the right of the Cole-Cole plots in Fig.3 can be represented by Equation (2). If this is reexpressed as $Z = Z' - jZ''$, the measured parallel capacitance C_p for the sample becomes

$$C_p = \frac{Z''}{(Z'^2 + Z''^2)\omega} \quad \cdots \cdots \cdots (3)$$

Replacing Z' and Z'' with the real and the imaginary part of Equation (2), respectively, gives

$$C_p = \frac{C_2}{(R_2/R_2 + 1)^2 + (R_2C_2\omega)^2} \quad \cdots \cdots (4)$$

From Figs.5 and 6, the temperature T(K) dependence of $R_1(\Omega)$, $C_1(F)$, $R_2(\Omega)$, $C_2(F)$ for PLT20 are given by

$$\log R_1 = 4.79 \times 10^3 (1/T) - 2.97 \quad \cdots \cdots (5)$$

$$\log R_2 = 7.86 \times 10^3 (1/T) - 6.55 \quad \cdots \cdots (6)$$

$$1/C_1 = 1.37 \times 10^7 T - 7.08 \times 10^9 \quad \cdots \cdots (7)$$

$$C_2 = -2.01 \times 10^{-11} T + 3.43 \times 10^{-8} \quad \cdots \cdots (8)$$

We can obtain the dielectric constant-temperature characteristics calculated from Equation (4) using the data given by Equation (5) to (8) at 0.1, 1, 10, 100 and 1000kHz for PLT20 shown in **Figure7**. This is very similar to the BP portion of the dielectric constant-temperature characteristics for PLT20 shown in Fig.2, proving that the dispersion type BP observed with the PLT ceramics prepared in the present study can be explained by Equation (4). In other words, as
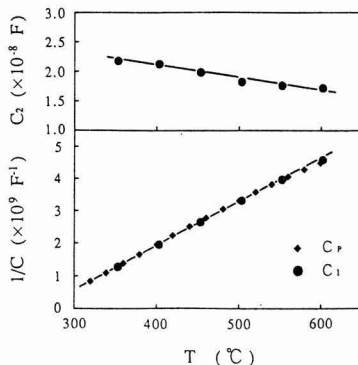
Fig. 6. Plots of equivalent capacitances C_1 and C_2 (in Fig.4) and the parallel capacitance (C_p) of sample PLT20 as functions of temperature measured at 1MHz.

evident from Equation (4) and Figs.5 and 6, we can conclude that since C_2 is larger than the bulk capacitance C_1, and R_2 is comparable to the bulk resistance R_1, any decrease in R_1 at high temperatures results in the C_2 effect in the low frequency range, causing the appearance of BP showing relaxed dispersions separate from the ordinary dielectric peak (NP) at the Curie temperature. Since $(R_1/R_2 + 1)^2 \ll (R_1C_2\omega)^2$ below the peak temperature of the BP, the level of C_p (or dielectric constant) in Equation (4) depends on the term $R_1C_2\omega$ (mainly R_1), and the dielectric constant increases as R_1 decreases. On the other hand, since $(R_1/R_2 + 1)^2 \gg (R_1C_2\omega)^2$ above the peak temperature of the BP, the level of C_p depends on the term $R_1/R_2 + 1$, and the dielectric constant decreases as R_1/R_2 increases.

Figure 8 also shows the temperature dependence of R_1,

R_2, and C_2 obtained from the same complex impedance analysis, for PLT5 and PLT20. To eliminate the effect due to the sample size, R and C are expressed in units of $\Omega \cdot$ cm (resistance × sample cross section/thickness) and F/cm (capacitance × sample thickness/cross section), respectively. In the temperature range 450° to 500°C where there is a prominent BP at 1kHz (see Fig.7), since R_1 was smaller, C_2 was larger and R_2 was nearly the same when comparing PLT20 to PLT5, the difference in BP level would be caused by the differences of R_1 and C_2 considering from Equation (4).

Based on the equivalent electrical circuit shown in Fig.4,

Fig. 7. Temperature dependence of the dielectric constant (ε') calculated from equation (4) using the data given by equations (5) to (8) at various frequencies for sample PLT20.
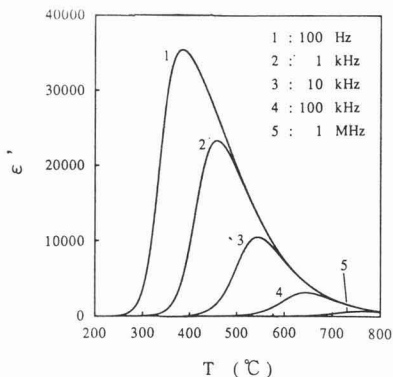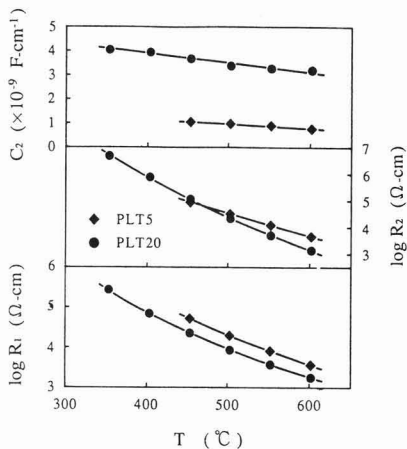

Fig. 8. Plots of equivalent resistances R_1 and R_2 and equivalent capacitance C_2 (in Fig.4) as functions of temperature for samples PLT5 and PLT20.
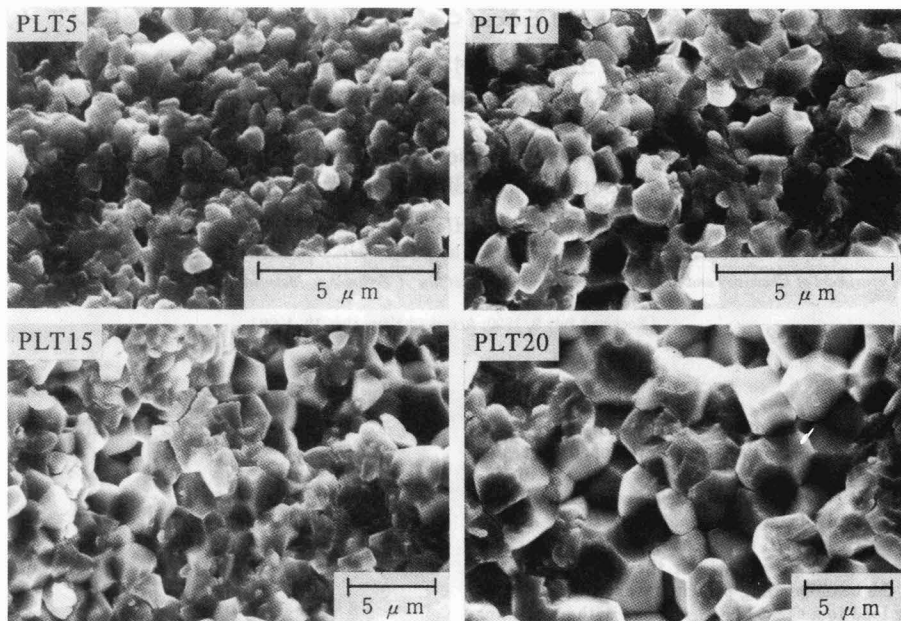

Fig. 9. SEM fracture surfaces of the present samples (bars = 5μm).

it can be concluded that the origins of R_2 and C_2 were the grain boundaries coupled in series with the bulk (R_1, C_1). In other words, as in the case of ZrO_2, Y_2O_3, and ferrite, it is highly probable that the cause of the relaxed dielectric dispersion in this material would be the interfacial polarization. **Figure 9** exhibits SEM photographs of fracture surfaces of the samples. No secondary phases could be detected at the grain boundaries by SEM observation, nor could a segregated layer be detected at the fractured grain boundaries by EPMA of the fracture surfaces. However, the higher the La content in a sample exhibiting a large BP, the higher the frequency of grain boundary fractures (shown in Fig.9), suggesting that very thin segregated layers were formed at the grain boundaries.

In the ceramic samples prepared in the present study, grain sizes and porosities were not constant. If the grain boundaries play an important role in the appearance of BP, then the grain size and porosity could have an effect on the difference in the total area of the grain boundaries or on the difference in the oxidized or reduced condition of the grain boundaries. These aspects, including analysis of complex impedance in temperature ranges below the Curie point, must be studied in more detail.

4. Conclusion

We investigated the temperature characteristics of the dielectric constant and complex impedance of PLT ceramics. The results obtained can be summarized as follows:

1) When measuring the dielectric constant-temperature characteristics, we observed in the temperature regions above the Curie point a broad dielectric peak which showed a relaxed dispersion highly frequency dependent in addition to observing an ordinary sharp dielectric peak at the Curie point.

2) The equivalent electrical circuit of the samples could be represented by a circuit of two RC components simply coupled in series. If $\tau_1 < \tau_2$, with $\tau_1 = R_1C_1$ and $\tau_2 = R_2C_2$, we discovered that the R_1C_1 component represented the bulk electrical characteristics, and the R_2C_2 component resulted in a dielectric peak which showed a relaxed dispersion. This suggested that the presence of the large R_2 and C_2 was the direct cause of the appearance of the broad dielectric peak which showed relaxed dispersion.

3) The large R_2 and C_2 could possibly be formed at grain boundaries, and may have produced interfacial polarization, causing the appearance of the dielectric peak showing relaxed dispersion.

References:
1) K. Goda and M. Kuwabara, Transaction of Ceramics, 98, 864-69 (1990).
2) M. Kuwabara, K. Goda and K. Oshima, Phys. Rev. B, in press.
3) G. A. Smolensky, J. Phys. Soc. Jpn.,28, Suppl., 26-37 (1970).
4) G. A. Smolensky, V. A. Isupov, A. I. Agranovskaya and S. N. Popov, Sov. Phys. - Solid State 2, 2584-94 (1961).
5) G. Goodman, J. Am. Ceram. Soc., 43, 105-13 (1960).
6) C. A. Ranadall, A. S. Bhalla, T. R. Shrout and L. E. Cross, J. Mater. Res., 5, 829-34 (1990).
7) S. Nomura and F. Kojima, Jpn. J. Appl. Phys.,12, 205-14 (1973).
8) M. Weller and H. Schubert, J. Am. Ceram. Soc.,69, 573-77 (1986).
9) G. R. Hyde, ibid., 54, 535-38 (1971).
10) C. G. Koops, Phys. Rev.,83, 121-24 (1951).
11) I. Ueda, Jpn. J. Appl. Phys.,11, 450-62 (1972).
12) K. Keizer and A. J. Burggraaf, Phys. Stat. Sol. (a),26, 561-69 (1974).
13) B. D. Cullity, Elements of X-ray Diffraction, New Edition, translated by G. Matsumura, Agune (1980) pp.320-37.
14) Y. Ito, K. Nagatsuma, H. Takeuchi and S. Jyomura, J. Appl. Phys.,52, 4479-86 (1981).
15) K. Okazaki, Ceramic Dielectric Engineering, 3rd edition, Gakuken-sha (1983) pp.176-80.

High and Medium Range Viscometers and Their Test with Some Alkali Silicate Glasses

Rikuo Ota, Fumiaki Tsuchiya, Kazuhisa Kawamura, Shogo Nakanishi and Jiro Fukunaga

Dept. of Chemistry and Materials Technology, Kyoto Institute of Technology

Matsugasaki, Sakyo-ku, Kyoto-shi 606, Japan

Viscometers capable of measuring a wide range of viscosity covering 1 to 10^{12}Pa·s were developed and tested for some alkali silicate glasses. For the range of 10^3 to 10^8 Pa·s, a conventional viscometer was used with a 5mm wide and 10mm long penetration tip of alumina tube, which lowered the measurable viscosity range maintaining the precision. For the range of 10^8 to 10^{12}Pa·s, the beam-bending principle was utilized. By applying load to a sheet glass specimen with an alumina tube, and by heating at 3°C/min, viscosities in the range of 10^8 to 10^{12}Pa·s were measured in a single run. It was shown that these viscometers can be applied to Li_2O-Na_2O-$2SiO_2$ glasses. It was demonstrated that glass transition temperature Tg agrees well with the temperature at which a viscosity of 10^{12}Pa·s was attained. It was also found that the viscosity vs. temperature relationship can be described by the Fulcher's type equation over the wide range temperature with good accuracy.

1. Introduction

It is well established that the viscosity of a glass changes widely, depending on the temperature at which it is measured, making it necessary to use different testing methods at different temperatures. Normal testing methods involve: (1) rotating viscometers to measure viscosities around 10^{-1}Pa·s and lower, (2) a method in which a platinum sphere is pulled up through the molten glass, or rotating viscometers for low-to-medium viscosities of 10^{-1} to 10^3Pa·s,[1] (3) only inadequate methods for the range of medium viscosities from 10^3 to 10^8Pa·s, (4) penetration type viscometers for high viscosities of 10^5 to 10^9Pa·s,[2-6] and (5) the fiber elongation or beam bending method for high viscosities of 10^8 to 10^{12}Pa·s.[7,8] In general, glass viscosities must be measured at high temperatures requiring special devices such as specific fibers for the fiber elongation method.

As mentioned above, there are, to date, no adequate methods or apparatus for measuring viscosities between 10^3 to 10^8Pa·s for several reasons. The method which involves drawing a platinum sphere through the molten glass, when applied to the measurement of viscosities in the order of 10^3Pa·s, takes a very long time, due to the extremely slow rate at which the sphere is pulled. Increasing the load to 100g or more, speeds up the sphere pulling-up rate, but does not accelerate the sphere free-falling rate.

The measurement of viscosities of 10^5Pa·s or less using conventional penetration-type viscometers is difficult due to the excessive penetration rate. Decreasing the load to 2g or less to reduce the lower limit of the penetration rate is undesirable, however, because it lowers the measurement accuracy due to the excessive friction over the penetration rod. In this study, the authors attempted to reevaluate whether the penetration principle is applicable to the viscosity range (3). In an attempt to secure a sufficient accuracy, the cross-sectional area of the of the penetration tip was increased to reduce the penetration rate in measuring viscosities on the order of 10^3Pa·s. The tip of the conventional penetration type viscometer is generally stainless steel, 1 to 5mm in diameter, and 3mm in length,[2] which limits its operable temperature to the range 750° to 800°C. This is another area to be improved.

In measuring viscosities in the order of 10^9Pa·s, i.e., near the upper limit of range (4), conventional penetration type viscometers have the disadvantage of penetration rates that are too low, even at a maximum load of 2kg with a 1mm-diameter tip. It is thus judged that the penetration method is inadequate for the measurement of viscosities of 10^9Pa·s or higher. The fiber elongation method is an alternative means of measurement; however, it is difficult to draw a constant diameter fiber from a highly viscous fluid, such as molten, high-silica glass compositions. Therefore, in this study, beam-bending was considered, instead of the penetration or fiber elongation methods, based on its usefulness in measuring the viscosity of plate-shape specimens. In addition, attempts were made to develop a new type of viscometer, where a penetration type viscometer was used to apply a load to the specimen and to detect displacement.

2. Objectives

In this study, attempts were made to develop a new type of viscometer capable of covering a wide range of viscosities from 10^3 to 10^{12}Pa·s, in which the modified penetration and beam-bending principles were combined. Its applicability was tested on several types of alkali silicate glasses (Li_2O-Na_2O-$2SiO_2$). The glass transition temperature Tg, determined from thermal expansion data, was compared with that estimated from the viscosity measurements, and the validity of the Fulcher equation used to approximate the viscosity-temperature relationship.
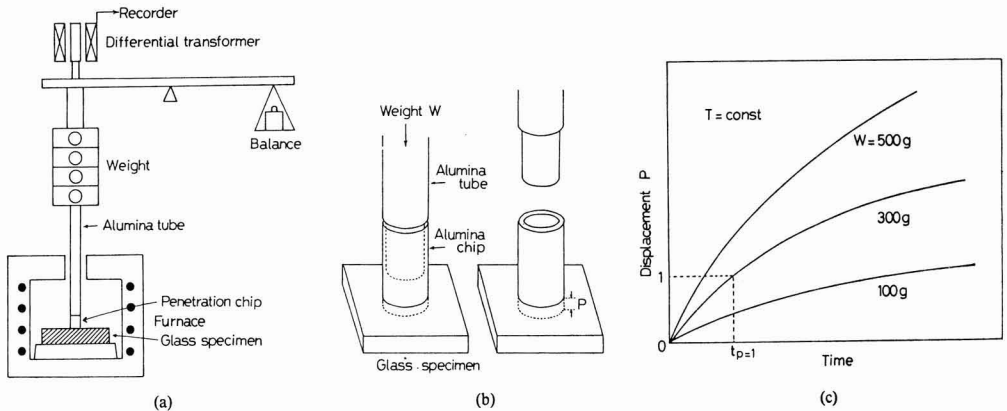
Fig. 1. Schematic view of a penetration viscometer for a medium viscosity range (a). (b) indicates a close-up of the penetration chip, and (c) represents P-t curves for different weights at a fixed temperature.

3. Procedure

3.1. Modified Penetration Type Viscometer

For viscosities in the medium range (3), from 10^3 to 10^8Pa·s, the penetration principle was used, with the cross-sectional area of the penetration tip increased to cover the above range.

Figure 1 illustrates the penetration type viscometer for measurement of the medium range viscosities; (a) is an overview of the viscometer, and (b) shows the penetration tip. The viscometer depends on the balance mechanism, where displacement is detected by a differential transformer. The penetration tip (b) was an alumina tube (trade name: SSA), 5mm in outer diameter and 4mm in inner diameter, cut to a length of approximately 10mm, and polished where it contacts the glass. It was inserted into a 4mm diameter alumina rod along with a platinum wire, in such a way that the tip remained in the glass sample when the alumina rod was pulled up. The tip was replaced for each test run. A glass sample with smooth surfaces, several millimeters thick, was required. When the viscosity is in the vicinity of 10^3Pa·s, the glass will be fluid; hence the glass sample was remelted in an alumina crucible cap (5cm diameter, 5mm deep) and cooled into a disc with smooth surfaces. It was heated in an electric furnace to a specified temperature T, at which it was held for approximately 20min; then the tip with its load was perpendicularly inserted into the sample slowly. The exact time at which the tip touched the sample surface could be judged from the recorded displacement-time chart, and was designated t=0.

Figure 1(c) shows the general relationship between the displacement P and the time t at a constant temperature T and load W. Theoretically, the following equation holds:[2]

$$Wt/\eta = AP^2 + BP \quad \cdots \cdots \cdots \cdots (1)$$

where, η is the viscosity, and A and B are constants. A log t - log η calibration chart was established for the standard sample, by measuring the time t (min) required for the tip with load W to attain a depth P=1mm. **Figure 2** shows the log t - log η relationship under the conditions of W=10 to 500g and $\eta=10^3$ to 10^8Pa·s for the standard B_2O_3 glass sample.[9,10] The measured value of around $\eta=10^3$Pa·s was
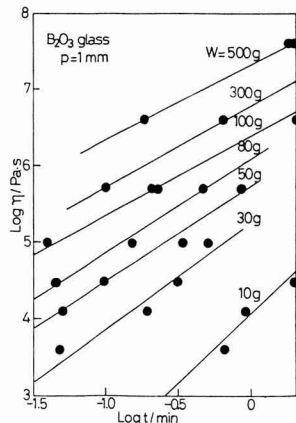
Fig. 2. Calibration curves for the penetration viscometer of a middle viscosity range.

considered to be reasonably accurate ($\Delta\log \eta = \pm0.1$), because the load used (W=10g) was sufficiently larger than the friction generated across the penetration rod supporting hole.

3.2. Beam-Bending Type Viscometer

In this study, the beam-bending principle was used, where the upper limit of the viscosity range was extended to 1012Pas, and special consideration was given to selection of the tip material so that it could withstand temperatures of 1500°C or more. **Figure 3(a)** illustrates the viscometer, which utilized the beam-bending principle, used to measure viscosities in the high viscosity range. The apparatus for a penetration viscometer was used for this system. **Figure 3(b)** illustrates the arrangement of the specimen and the loading rod. The specimen was a glass plate with a width a of approximately 10mm, length of around 50mm, and thickness b of around 2mm, supported by two alumina tubes (3mm in diameter) approximately 40mm apart from each other (span s=40mm). The specimen was supported on a base of refractory bricks (trade name: CPM). An alumina tube (SSA, 6mm diameter, 30cm long) was placed perpen-
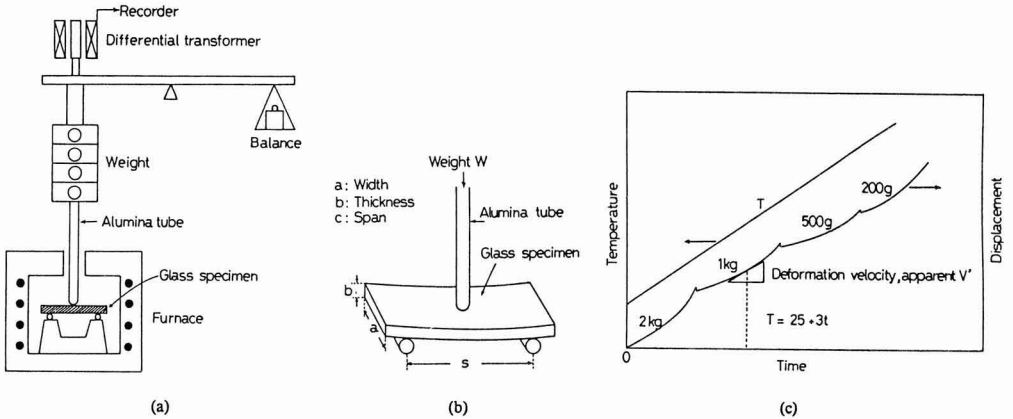
Fig. 3. Schematic view of a beam-bending viscometer for a high viscosity range (a). The close-up of the loading alumina tip is shown in (b), and a schematic representation of P-t curve with varying weight on heating the sample is shown in (c).

dicular to the glass specimen, with its round edge contacting the glass where it could deform the specimen by its load. The load W applied to the alumina sheath could be varied up to 2kg using a variable loading device.

In general, a glass specimen having a viscosity of η will be deformed at a rate of V, when pressed by a load W according to the following relationship:

$$V = k\,(s^3/ab^3)\,(W/\eta) \ldots \ldots \ldots \ldots (2)$$

where, k is a constant depending on the specimen size. It is also expected that k will varies with temperature, because elasticity is involved in the deformation of a highly viscous material. An attempt was made, therefore, to establish a calibration line to represent the relationship between η and $(s^3/ab^3)\times(W/V)$, while heating a standard quartz glass specimen at 3°C/min.

Test Procedure: The specimen was set on the supporting base after measuring its dimensions (a and b) with slide calipers. The alumina tube, with a load of W (max. = 2kg), was placed upright at the central part of the glass specimen with its round edge contacting the specimen. The specimen was heated at 3°C/min, and the displacement of the loading rod, detected by the differential transformer was recorded. The glass specimen was a flat plate and the alumina rod made a point-contact with it; however, the glass plate was deformed in such a way that it was bent at the center. It has been confirmed that the error in the contacting point position does not significantly affect the measurement accuracy. Since the deformation rate increases as the temperature increases, the load was reduced stepwise from 2kg to 1kg as the temperature increased from 5° to 10°C, and then further reduced to 500g with another temperature increment of 5° to 10°C. The deformation rate was controlled in such a way as to keep the total displacement within 3mm before viscosity reaches the lower limit of the measurable range, i.e., around 10^8Pa·s.

Figure 3(c) shows the relationships between temperature T (°C) - time t (min) and displacement P (mm) - time t. A decrease in the displacement observed as soon as load reduced would indicate that the deformation elastic. The apparent displacement rate V' for each temperature from the t-P relationship was determined. The intrinsic deformation **rate** V, was also determined taking into account thermal
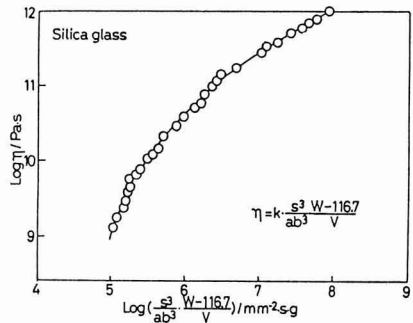
Fig. 4. Calibration curve for the beam-bending viscometer obtained by use of a silica glass.

expansion coefficient α and length of the heated section L, using the following equation:

$$V = V' + \alpha L \ldots \ldots \ldots \ldots \ldots \ldots (3)$$

The αL-temperature relationship can be predetermined from a blank test. Viscosity η at each temperature may be known from the calibration curve (**Fig.4**) with a given reciprocal displacement rate normalized by the dimensions $(s^3/ab^3)(W/V)$.

The axis of abscissa of Fig.4 represents true load W-116.7 (W: weight of the counterweight, and the numeral 116.7 is a correction for the balance). Non-linearity of the log-log plot results conceivably from contribution of elasticity to deformation rate varying with temperature.

3.3. Measurement of Viscosity for Alkali Silicate Glass

Viscosity of several types of mixed alkali silicate glass of the $(1-x)Li_2O\cdot(x)Na_2O \cdot 2SiO_2$ (x=0 to 1) composition was measured, in order to confirm validity of the viscometer. Each glass sample was prepared from the reagent grade SiO_2 powder and anhydrous alkali carbonate as the starting materials, which were treated at 1100° to 1400°C in a platinum crucible for 0.5 to 1h to melt the mixture. The quenched glass was formed into a plate, which was polished to pre-specified dimensions, prior to being measured by the beam-bending type viscometer. For the measurement of

viscosities in a medium-to-high viscosity range by the penetration type viscometer, the glass specimen was remelted and remolded. The viscosity of these specimens were measured by pulling-up a platinum sphere through the glass, as well as by the modified penetration-type and beam-bending type viscometers. For the beam-bending test, each specimen was heated at 3°C/min. The glass transition temperature Tg, determined from thermal expansion data, was compared with that obtained from viscosity measurements, and the validity of the Fulcher equation was investigated.
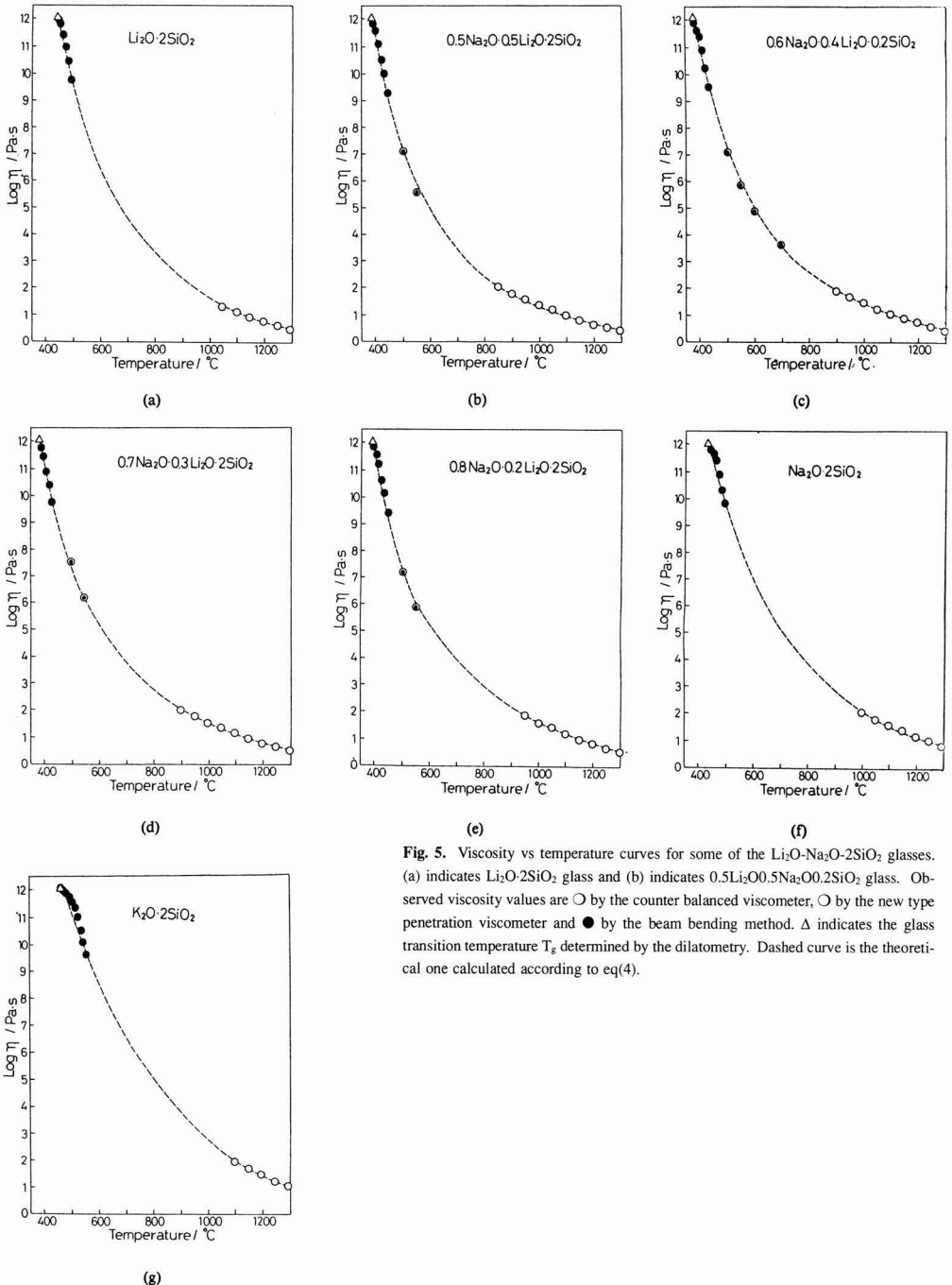
Fig. 5. Viscosity vs temperature curves for some of the Li_2O-Na_2O-$2SiO_2$ glasses. (a) indicates $Li_2O\cdot2SiO_2$ glass and (b) indicates $0.5Li_2O0.5Na_2O0.2SiO_2$ glass. Observed viscosity values are $\bigcirc$ by the counter balanced viscometer, $\bigcirc$ by the new type penetration viscometer and $\bullet$ by the beam bending method. Δ indicates the glass transition temperature T_g determined by the dilatometry. Dashed curve is the theoretical one calculated according to eq(4).

Table 1. Glass transition temperature T_g for the $(1-x)Li_2O\cdot(x)Na_2O\cdot 2SiO_2$ glasses, (x = 0 to 1.0), determined by thermal delatometry.

Composition x of $(1-x)Li_2O\cdot(x)Na_2O\cdot 2SiO_2$ glass										
0.0	0.1	0.2	0.3	0.4	0.5	0.6	0.7	0.8	0.9	1.0
437	413	405	390	387	383	383	382	384	401	435

(Tg/°C row label at left)

Composition y of $(1-y)(0.4Li_2O\cdot 0.6Na_2O)\cdot(y)K_2O\cdot 2SiO_2$ glass										
0.0	0.1	0.2	0.3	0.4	0.5	0.6	0.7	0.8	0.9	1.0
383	375	380	380	380	385	384	398	386	430	484

(Tg/°C row label at left)

4. Results and Discussion

4.1. Measurement of Viscosity of Alkali Silicate Glasses

Figures 5(a) ~ (g) show the test results for the $(1-x)LiO_2\cdot(x)Na_2O\cdot 2SiO_2$ compositions, for (a) x=0, (b) x=0.5, (c) x=0.6, (d) x=0.7, (e) x=0.8 and (f) x=1. Compositions with x=0 and x=1 and similar ones were devitrified by heating; thus their viscosities in a medium-to-high range could not be measured. The results for the other compositions are not reported here. Based on the calibration curve, the accuracy of measurement was determined to be within $\Delta \log \eta = \pm 0.1$. The point marked with a $\triangle$ represents the glass transition temperature Tg determined from the thermal dilatometry data in **Table 1**. As shown, this Tg was in good agreement with the temperature that gives a viscosity $\eta = 10^{12}$Pa·s. This viscosity-temperature relationship, however, was considerably different from the one for Bi-Ca-Sr-Cu-O glass which exhibited a viscosity of 10^{12}Pa·s or less at its Tg.[11] Confirmation of this kind would be one of the importance to measure medium-to-high range viscosities.

The broken line represents the Fulcher correlation (Equation (4)), based on the measured Tg and high-temperature viscosities:

$$\log \eta = A + B/(T - T_o) \quad \ldots \ldots \ldots \ldots (4)$$

As shown in Fig.5(b), the differential between the observed and calculated viscosities was $\Delta \log \eta < 0.2$ in the medium-to-high range. It has been thus demonstrated, viewed from the measurement accuracy, that the Fulcher equation predicts viscosity, measured by the three methods, reasonably well.

4.2. Problems involved in Measurement of Viscosity in Medium-to-High Range

The modified penetration-type viscometer allowed easy replacement of the penetration tip and enabled the measurement of low-range viscosities. These advantages were a result of the wider cross-sectional area of the tip. This, however, also produced one disadvantage in that it was difficult to establish good contact between the tip and the glass specimen surface. It is recommended that the measurement be carried several times at the same temperature level, to increase accuracy.

The beam-bending type viscometer measured viscosity of the specimen being heated, and the deformation rate of the specimen naturally depended on the temperature to which it was exposed. Heating the specimen, however, was unavoidable, because keeping the specimen at a constant temperature caused the sample to deform by its own weight. It is assumed that the relationship between the deformation rate and the viscosity of the specimen tested was the same as that of the standard specimen, and it is essential to use

the same heating rate as that used for establishing the calibration curve.

Measurement of medium-to-high viscosities is impossible when the specimen is crystallized while being heated. It should be noted, therefore, that measurement of viscosity in this range may be impossible, unless the specimen has a composition highly resistant to crystallization, such as a mixed alkaline glass.

5. Conclusions

1) It has been demonstrated that the conventional penetration-type viscometer is applicable to viscosity measurements in a range from 10^3 to 10^8Pa·s, if the penetration tip is changed in material (to alumina) and shape.
2) A new type of viscometer, capable of measuring viscosities in a range from 10^8 to 10^{12}Pa·s, has been developed, based on the beam-bending principle.
3) Applicability of these viscometers were investigated with glasses of Li_2O-Na_2O-$2SiO_2$ compositions. The platinum sphere pulling-up method was also used.
4) For each composition, the temperature at a viscosity of 10^{12}Pa·s was in good agreement with glass transition temperature Tg determined from the thermal dilatometry chart.
5) It has been confirmed that the viscosity of these compositions can be predicted by the Fulcher equation reasonably well.

References:
1) R. Ota, "Ceramics Experiment Manual," edited by the Dept. of Inorganic Materials Engineering, Kyoto Institute of Technology, Nikkan Kogyo Simbun, (1989) pp.174-177.
2) M. Kunugi, R. Ota, and Y. Yamate, Zairyo, 15, 567-571 (1966).
3) M. Kunugi, R. Ota, and M. Suzuki, ibid., 19, 145-150 (1970).
4) K. Matusita, S. Sakka, J. Non-Cryst. Solids, 17, 436-439 (1975).
5) S. Sakka, K. Kamiya, K. Matusita, Res. Rep. Fac. Eng. Mie Univ., 1, 47-58 (1976).
6) K. Matusita, T. Watanabe, K. Kamiya, S. Sakka, Phys. Chem. Glasses, 21, 78-84 (1980).
7) H.E. Hagy, J. Am. Cer. Soc., 46, 93-97 (1963).
8) K. Kobayashi and R. Yokota, Yogyo Kyokai-shi, 76, 218-223 (1968).
9) A. Napolitano, P.B. Macedo, E.G. Hawkins, J. Amer. Cer. Soc., 48, 613-616, (1965).
10) J. Boow, Phys. Chem. Glasses, 8, 45-55 (1967).
11) M. Tatsumisago, C.A. Angell, S. Tuboi, Y. Akamatu, T. Thoge, T. Minami, Appl. Phys. Lett., 54, 2268-2270 (1989).

Quantitative Analysis of o'-phase in β'-o' Sialon Ceramics by Image-Analysis Technique

Kazuya Yabuta, Hiroaki Nishio and Keizo Uematsu*

Advanced Technology Research Center, NKK Corporation, Kawasaki-ku, Kawasaki-shi 210, Japan

* Department of Chemistry, Nagaoka University of Technology, Kamitomioka-cho, Nagaoka-shi, 940-21 Japan

To determine the content of o'-phase in β'-o' sialon ceramics, green compacts of a Si_3N_4 powder and boehmite sol were oxidized at 900 to 1050°C, followed by sintering and HIPing. The ratios of O/N in the prepared sialons were changed at a fixed ratio of Si/Al. X-ray diffractometry, optical and scanning electron microscopy, electron-probe microanalysis were used for examination. Optical and electromicrographs coupled with image analysis showed that, with increasing oxidation temperature, the amount of o'-phase increased and its grain size decreased. The o'-phase contents determined were well correlated to that calculated from the XRD results. These results explained the densities of sialon ceramics.

1. Introduction

Sialon, having a substantial high temperature strength and a high resistance to oxidation, is being considered as a possible ceramic material for engines.[1-5] To improve its performance, the authors have developed a new type of material having a β'-phase ($Si_{6-z}Al_zO_zN_{8-z}$) and an o'-phase ($Si_{2-x}Al_xO_{1+x}N_{2-x}$) by sintering a mixture of silicon nitride and alumina.[6-11] We have also attempted to control the material properties by varying its phase ratio, composition, dimensions, shape and distribution.

As the first step of this study, we will discuss the quantification of the o'-phase. In determining the bulk density of a multiphase system such as sialon, the theoretical density of the material must first be obtained, by quantifying the ratio between phases. Without this ratio, it is impossible to verify the relationship between the process and the bulk density or other properties, which is common in the study of materials. For the present material, no quantifying methods, either high accuracy or semiquantitative, have been established, and has been a huge obstacle to further research. The difficulty in establishing a quantification method for this material lies in the fact that the ratio of the o'-phase is complexly altered by the oxygen contained in the starting silicon nitride powder. Furthermore, and the slight oxidation of the powder during mixing and degreasing prohibits the manufacture of that standard samples with well-controlled phase ratios.

Using an image analysis method in the present study, the authors have examined the ratio between existing phases. For evaluation, we prepared compacted sialon samples with the O/N ratio varied against a constant Si/Al ratio by thermally oxidizing molded mixtures in air.

2. Test Method

Sialon samples with different o'-phase ratios were manufactured as follows: Alumina sol (made by Nissan Chemicals) was fired at 1200°C to determine the alumina content and was added, in a quantity such that the Al_2O_3 residual was 9wt%, to the α-Si_3N_4 powder (made by Ube Kosan) with oxygen content 1.1wt% manufactured via imid pyrolosis. The product was mixed with water in a ball mill for 20h. It was then dried by atomizing and calcining in air at 500°C for 15h, resulting in a powdered material. This powder was temporarily molded in a 25×80mm mold under 30MPa and the moldings were CIPped under 300MPa into compacted powder blocks. The blocks were heat treated in air for 2h at 900°, 950°, 1000°, and 1050°C to yield samples with different oxygen contents. The heat treated samples and others not heat treated were sintered at 1900°C, in N_2(1MPa), for 10h, and then HIPped at 1900°C, in Ar-N_2 mixed gas, 190MPa (N_2 pressure 20MPa) for 2h. Thus the β'-o' sialon samples, about 20×15×65mm, were prepared. Densities were measured by Archimedes' method. To evaluate the o'-phase, the samples were cut into small blocks about 20×15×10mm, and one face of each sample was mirror polished. The polished surfaces were observed under a reflection microscope and by EPMA. To quantify the o'-sialon, X-ray and image analysis methods were used. In the X-ray analysis, the mirror polished surfaces were exposed directly to X-rays and the ratio of the o'-phase was obtained from the integrated intensities of the diffraction peaks of the (101) and (210) faces of β-Si_3N_4 and the (110) and (020) faces of Si_2N_2O using the following equation:

$$(o'\text{Phase ratio}) = \frac{I_{o'_{110}} + I_{o'_{020}}}{I_{o'_{110}} + I_{o'_{020}} + I_{β'_{101}} + I_{β'_{200}}} \times 100$$

To examine o'-phase patterns, the polished surfaces were etched with a 1:1 solution of nitric and hydrofluoric acids and observed under an SEM. To measure the lattice constants, the β'-o' sialon samples were crushed and metallic Si was used as the internal standard in X-ray diffraction analysis.

3. Results

Figure 1 shows the density of the HIPped samples in relation to oxidation temperature. The density decreased nearly linearly as the oxidation temperature increased.

While the density of the sample not heat treated was $3.109 g/cm^3$, that of the sample treated at 1050°C was $3.054 g/cm^3$.
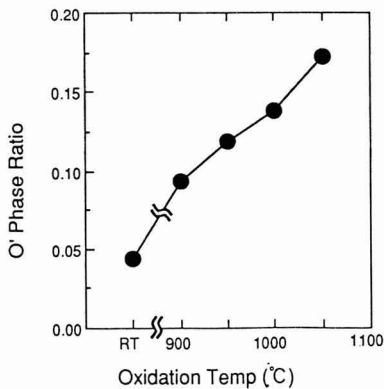
Fig. 1. Relationship between oxidation temperature and density of HIPped β'-o' sialons.

Figure 2 shows typical optical reflection micrographs of an untreated sample and samples treated at 900° and 1050°C. The polished surfaces showed no pores, suggesting that the samples were densified almost completely. The microstructures of all samples were composed of dark bar-shaped precipitates scattered in bright matrices having a high reflection factor. By raising the oxidation temperature, the number of precipitates increased, but their sizes decreased. With all samples, there was no prominent difference between the microstructure at the surface and in the interior.

Figure 3 shows the results of EPMA observation using the same samples previously observed under the optical reflection microscope. The SEM images showed no ruggedness and few pores on the surfaces. EPMA observation, on the other hand, detected black, precipitated phases as shown in the figure. The patterns of these precipitated phases were the same as those detected by the optical reflection microscope. As the oxidation temperature increased, the quantity of precipitates increased, and the size of the particles decreased. In image analysis, the black, precipitated phases were quantified as 11.0vol% for the untreated sample, and 18.3 and 23.1vol% for the samples oxidized at 900° and 1050°C respectively, proving that the volume ratio of the black precipitates increased with oxida-
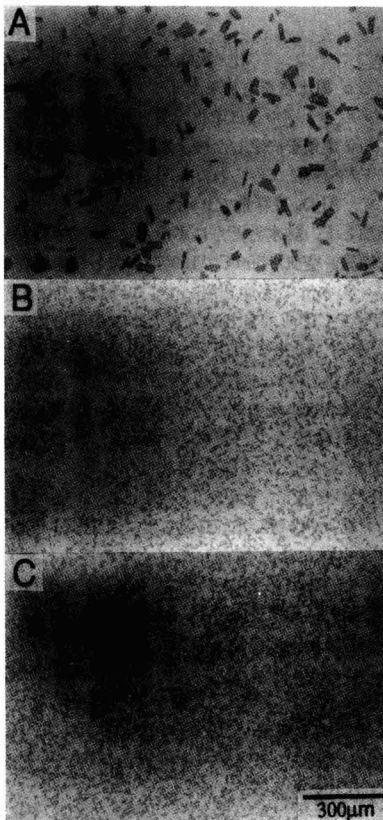
Fig. 2. Optical micrographs of β'-o' sialons after polishing.
(A) Non oxidation, (B) Oxidation at 900°C, (C) Oxidation at 1050°C.
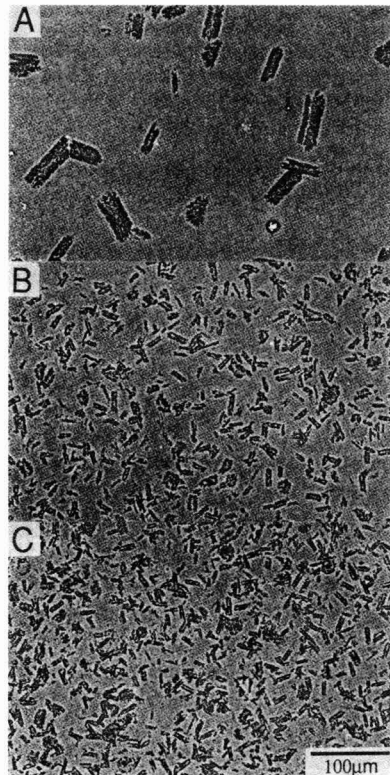
Fig. 3. Electron-probe microanalizer pictures of β'-o' sialons after polishing.
(A) Non oxidation, (B) Oxidation at 900°C, (C) Oxidation at 1050°C.

tion temperature.

The ratios of o' and other phases found in samples oxidized under various conditions were examined by X-ray diffraction. The results are shown in **Table 1**. No crystal phases were detected other than a β'-phase (β-Si₃N₄ structure) and an o'-phase (Si₂N₂O structure). This agrees with the data by Kishi, et al., for a sialon sample prepared by hot pressing a material containing aluminum alkoxide as the source of Al_2O_3.[8-10] The o'-phase ratio increased with oxidation temperature. It was 4.4% for the sample not treated and 17.2% for the sample oxidized at 1050°C.

Tables 2 and **3** give the lattice constants of the samples oxidized under various conditions. As the oxidation temperature increased, β'-phase lattice constants increased slightly, but o'-phase lattice constants decreased slightly, both changing by as little as 1%.

Figure 4 shows the relationship between the o'-phase ratio obtained by X-ray diffraction and the o'-phase volume ratio obtained from the results of image analysis of EPMA photographs. The smooth curve suggests that the precipitated phase detected by reflection microscopy as shown in Fig.2, detected by EPMA as shown in Fig.3, is the o'-phase.

Figure 5 shows the SEM photographs of the polished surface and the etched surface of a sintered sample. The o'-phase was dissolved by etching, leaving behind a peculiar structure. In addition to the structures definitely identified as etched voids of the o'-phase, a number of irregularly shaped etched scars were observed on the surface. These scars may have been voids of part of the o'-phase emerging on the polished surface, or perhaps a vitreous phase. The vitreous phase, which would result in errors when quantifying the o'-phase by image analysis, was considered small or negligible. It was thus concluded that the o'-phase could be quantified by image analysis.

$$\frac{Io'_{110} + Io'_{020}}{Io'_{110} + Io'_{020} + I\beta'_{101} + I\beta'_{200}} \times 100$$

Fig .4. Relationships between o'-phase contents calculated from the XRD results and the image on EPMA pictures.
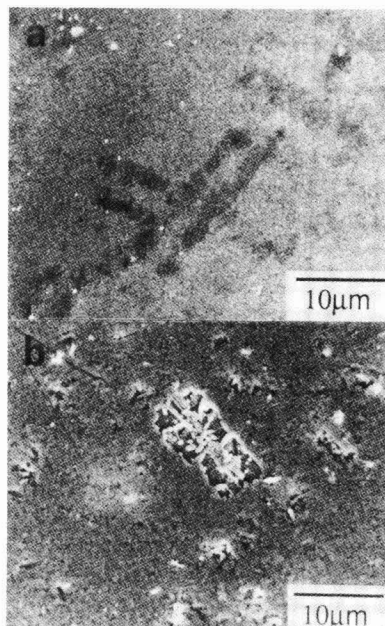
Fig. 5. Scanning electron micrographs of HIPped β'-o' sialon. (A) after polishing. (B) after etching.

Table 1. Phases and o'-phase ratio of HIPped β'-o' sialons.

Oxidation Conditions	Phases	o' phase ratio (%)
Non Oxidation	β' ,o'	4.4
900°C	β' ,o'	9.3
950°C	β' ,o'	11.9
1000°C	β' ,o'	13.8
1050°C	β' ,o'	17.2

Table 2. Lattice constants of β'-sialon in HIPped β'-o' sialons.

Oxidation Conditions	a-axis(A)	c-axis(A)	Cell volume(A³)
Non Oxidation	7.6151±0.0004	2.9183±0.0002	146.56±0.02
900°C	7.6162±0.0006	2.9183±0.0003	146.60±0.03
950°C	7.6170±0.0004	2.9190±0.0002	146.66±0.02
1000°C	7.6173±0.0005	2.9190±0.0002	146.68±0.02
1050°C	7.6166±0.0005	2.9197±0.0003	146.69±0.02

Table 3. Lattice constants of o'-sialon in HIPped β'-o' sialons.

Oxidation Conditions	a-axis(A)	b-axis(A)	c-axis(A)	Cell volume(A³)
Non Oxidation	5.5008±0.0014	8.8926±0.0026	4.8566±0.0009	237.57±0.10
900°C	5.4988±0.0007	8.8937±0.0013	4.8580±0.0005	237.58±0.05
950°C	5.4976±0.0007	8.8908±0.0013	4.8567±0.0005	237.38±0.05
1000°C	5.4951±0.0006	8.8917±0.0011	4.8580±0.0004	237.37±0.05
1050°C	5.4979±0.0006	8.8898±0.0012	4.8555±0.0004	237.31±0.05

Table 4. Theoretical density of β'-sialon and o'-sialon in β'-o' sialons.

Oxidation Conditions	β'-Sialon(g/cm³)	o'-Sialon(g/cm³)
Non Oxidation	3.184	2.806
900℃	3.184	2.805
950℃	3.182	2.808
1000℃	3.182	2.808
1050℃	3.182	2.809

Table 5. Theoretical o'-phase ratio.

Oxygen Contents(wt%)	o' phase ratio(vol%)
0.0	9.90
0.5	13.04
1.0	16.16
1.5	19.26
2.0	22.32
2.5	25.39
3.0	28.40

4. Discussion

The lattice constants for β' sialon shown in **Table 2** were a=7.615 to 7.617. Using the data on lattice constants for β' sialon reported by Mitomo:[12]   a=7.603 for Z=0, and a=7.636 for Z=1, the Z value for the β'-phase could be estimated as 0.5. Also, since the lattice constant of the β'-phase barely changed, the mean composition of the β'-phase was estimated to be $Si_{5.5}Al_{0.5}O_{0.5}N_{7.5}$ irrespective of the oxidation temperature (including the non-oxidized case).

Table 4 shows theoretical densities which gave rise to the mean compositions of β'- and o'-phases determined as $Si_{5.5}Al_{0.5}O_{0.5}N_{7.5}$ and $Si_{1.833}Al_{0.167}O_{1.167}N_{1.833}$, respectively, in conjunction with the lattice constants shown in **Tables 2 and 3**.

The theoretical densities of the sintered sialon composites of the sample not oxidized and the samples oxidized at 900° and 1050°C could be calculated on the basis of the volume ratio of the o'-phase (Fig.3) obtained from the results of image analysis and the theoretical densities (Table 4). On the assumption that the sintered samples did not contain pores, the densities of the three types of samples could be calculated as 3.142, 3.115, and 3.096g/cm³ respectively. The relative densities, i.e., the measured densities of the composite sialon samples shown in Fig.1 divided by the theoretical densities, were 98.9, 99.3 and 98.6%, respectively, which were consistent with the high densities of the HIPped samples.

In the image analysis, the o'-phase ratio was obtained on the basis of the pattern specifically identified. However, as shown in **Fig.5**, o'- and vitreous phases can exist in the other zones. The ratios of such low-density phases are probably underestimated and the theoretical densities may, in practice, be lower than the calculated values above. This consideration is consistent with the fact that no pores were detected in the polished surfaces of the sintered samples; thus, the bulk densities could be estimated as nearly 100%.

It is evident that sintered dense sialon products can be obtained irrespective of oxidizing treatment and oxidation temperature. As the oxidation temperature rose in Fig.1, the density decreased. This was because the oxygen content in the samples increased with the oxidation temperature, caus-

ing the low-density o'-phase to be precipitated in greater quantities.

Assuming that all oxygen contained in the Si_3N_4 powder existed as SiO_2, and that the SiO_2 was allocated to the β'- and o'-phases in the sintered products, we obtained the volume ratios of the o'-phase on the basis of the composition of the mixed raw material powders. The results are shown in **Table 5**. Moreover, since the Si/Al ratios slightly decreased as the oxygen content increased, the mean Si/Al ratios were calculated each time, and the Si/Al ratios of both phases were equated to the mean composition. This calculation showed that if there are no oxides in the starting Si_3N_4 powder, the volume ratio of the o'-phase was 9.90%, and that of the powder (oxygen content: 1.1wt%) used in the present test, was about 17%. Since our results showed that the unoxidized sample had an o'-phase volume ratio of 11%, it was assumed that oxygen (about 2wt%) in the starting Si_3N_4 powder contributed to the phase balance. It was also assumed that the remaining oxygen in the raw material powder escaped relatively easily during sintering, partly in the form of SiO gas (produced from the reaction of SiO_2 with Si_3N_4 and Al_2O_3 during sintering) and partly removed by weak forces such as adsorption onto Si_3N_4 surfaces.[13,14] On the other hand, with the samples oxidized at 900° and 1050°C, it was assumed that oxygen, 1.3 and 2.1wt% respectively, in the Si_3N_4 powder contributed to the phase balance. To define the quantity of oxygen added during oxidation, we measured increases in quantity, but reached no conclusion because the dehydration of H_2O in Al_2O_3 and the oxidation of Si_3N_4 occurred simultaneously.

5. Conclusion

Using compacted sialon samples, with O/N ratio varied against a constant Si/Al ratio, prepared by thermally oxidizing molded mixtures of raw material in air, we investigated the o'-phase in the sintered products, with the following results:

1) As the oxidation temperature increased, the quantity of the o'-phase increased but its particle size decreased.
2) The o'-phase ratios obtained by X-ray diffraction and the o'-phase ratios in vol% obtained by image analysis could be represented by smooth curves. With sintered β'-o' sialon products, we were able to represent o'-phase ratios of sintered products by the o'-phase ratios obtained by X-ray diffraction.

References:
1) K.H. Jack, J. Mater. Sci., 11, 1135-58 (1976).
2) Y. Koyama and O. Kamigaito: Ceramics Association, 80, 327-36 (1972).
3) Z.K. Haung, P. Greil and G. Petzow, Ceramics International, 10, 14-17 (1984).
4) M.B. Trigg and K.H. Jack, Proc. Int. Symp. on Ceramic Components for Engines, 199-07 (1983).
5) D.P. Thompson, W.Y. Sun and P.A.Walls, Proc. Int. Symp. on Ceramic Components for Engines, 643-650 (1986).
6) S. Umebayashi, K. Kishi, E. Tani, and K. Kobayashi: Ceramics Association, 92, 45-51 (1984).
7) E. Tani, H. Ichinose, K. Kishi, M. Umebayashi, and K. Kobayashi: Ceramics Association, 92, 675-79 (1984).
8) K. Kishi, S. Umebayashi, E. Tani, and K. Kobayashi: Ceramics Association, 93, 629-35 (1985).

9) K. Kishi, S. Umebayashi, and K. Kobayashi: Journal of Ceramics, 96, 546-50 (1988).

10) K. Kishi, S. Umebayashi and E. Tani, J. Materials Sci., 25, 2780-84 (1990).

11) K. Yabuta, H. Nishio and H. Okamoto, Proc. Int. Symp. on Ceramic Components for Engines, 622-30 (1988).

12) M. Mitomo, N. Kuramoto, M. Tsutsumi, and H. Suzuki: Ceramics Association, 86, 526-31 (1978).

13) D.R. Messier and E.J. Deguire, J. Am. Ceram. Soc., 67, 602-4 (1984).

14) N. Hirozaki and A. Okada: Ceramics Association, 95, 235-39 (1987).

Studies on the Synthesis of Polymetalloxanes and Their Properties as a Precursor for Amorphous Oxide (Part 6)
—Preparation of SiO$_2$-TiO$_2$ Fibers Containing Various TiO$_2$ Contents from Polytitanosiloxanes—

Takahiro Gunji, Yukinori Nagao, Takahisa Misono and Yoshimoto Abe

Department of Industrial Chemistry, Faculty of Science and Technology, Science University of Tokyo
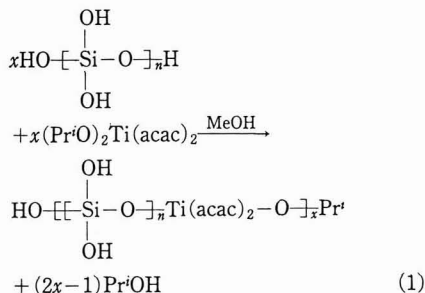2641 Yamazaki, Noda, Chiba 278, Japan

Preparation of SiO$_2$-TiO$_2$ fibers containing various TiO$_2$ contents by a new method was investigated. In order to obtain polytitanosiloxanes (PTS), a precursor, partially hydrolyzed tetraethoxysilane (TEOS) was brought into reaction with bis(2,4-pentanedionato)titanium diisopropoxide (PTP) in methanol in various molar ratios of TEOS/PTP from 1 to 15. Concentration of the resultant methanol solutions of PTS gave sols with spinnability, from which SiO$_2$-TiO$_2$ ceramic fibers containing 5-50 TiO$_2$ mol% were prepared.
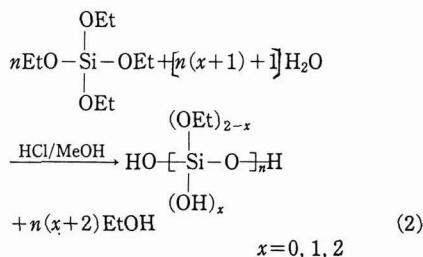[Received August 13, 1990; Accepted December 14, 1990]

A precursor method or preceramic polymer method for preparing ceramics with inorganic polymers as precursors is a potential route for synthesizing fine ceramic fibers as well as fine powders and thin films because the structure of the precursors and/or ceramics to be formed can be controlled by polymerization reaction of pure monomers. By this method, the preparation of ceramic fibers such as silicon carbide[1], silicon nitride[2] and boron nitride[3] has recently been realized.

We have reported the preparation of SiO$_2$-TiO$_2$ ceramic fibers[4] by the new method: The inorganic polymers, polytitanosiloxanes, synthesized by the reaction (eq.1) of silicic acid (SA, as SiO$_2$) with the titanium chelate com-

$$
x\mathrm{HO}\!\left[\!\begin{array}{c}\mathrm{OH}\\|\\\mathrm{Si-O}\\|\\\mathrm{OH}\end{array}\!\right]_{\!n}\!\!\mathrm{H}
$$
$$
+x(\mathrm{Pr}^i\mathrm{O})_2\mathrm{Ti}(\mathrm{acac})_2 \xrightarrow{\mathrm{MeOH}}
$$
$$
\mathrm{HO}\!\left[\!\left[\!\begin{array}{c}\mathrm{OH}\\|\\\mathrm{Si-O}\\|\\\mathrm{OH}\end{array}\!\right]_{\!n}\!\!\mathrm{Ti}(\mathrm{acac})_2\!-\!\mathrm{O}\right]_{\!x}\!\!\mathrm{Pr}^i
$$
$$
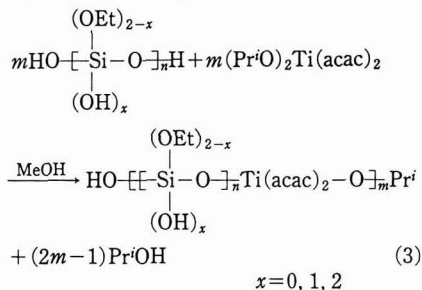+(2x-1)\mathrm{Pr}^i\mathrm{OH} \qquad\qquad (1)
$$

pound (PTP) are found to provide the fibers with a tensile strength comparable to the silica fibers prepared by the sol-gel method[5]. In this method, however, the fibers containing less than 50mol% TiO$_2$ are hardly obtained, for the reaction in the molar ratio (PTP/SA) less than one forms no soluble

polytitanosiloxanes, that is, the formation of polymerized silicic acid or more possibly polytitanosiloxanes with a highly polymerized siloxane unit takes place at molar ratio (PTP/SA) less than one. Therefore, the functionality of silicic acid has to be regulated in order to obtain soluble polymers. Works[6] on the hydrolysis of tetraethoxysilane (TEOS) suggest the formation of siloxane oligomers as unstable intermediates which undergo condensations to form polysiloxanes with different structures depending on the hydrolysis conditions. The intermediate may be represented by eq. 2 at the initial stage of hydrolysis when the functionality of the silanol intermediate is regulated to be x=0 or x=1, provided the hydrolysis is carried out in the

$$
n\mathrm{EtO}\!-\!\!\begin{array}{c}\mathrm{OEt}\\|\\\mathrm{Si}\\|\\\mathrm{OEt}\end{array}\!\!-\!\mathrm{OEt}+\left[n(x+1)+1\right]\mathrm{H}_2\mathrm{O}
$$
$$
\xrightarrow{\mathrm{HCl/MeOH}} \mathrm{HO}\!\left[\!\begin{array}{c}(\mathrm{OEt})_{2-x}\\|\\\mathrm{Si-O}\\|\\(\mathrm{OH})_x\end{array}\!\right]_{\!n}\!\!\mathrm{H}
$$
$$
+n(x+2)\mathrm{EtOH} \qquad\qquad (2)
$$
$$
x=0,\,1,\,2
$$

molar ratio H$_2$O/TEOS less than four under mild conditions, and the reaction with PTP (eq. 3) would allow the formation of a soluble PTS stable to self condensation.

The results of the reaction in various molar ratios of PTP to the hydrolysis product (as TEOS) are summarized in table

$$
m\mathrm{HO}\!\left[\!\begin{array}{c}(\mathrm{OEt})_{2-x}\\|\\\mathrm{Si-O}\\|\\(\mathrm{OH})_x\end{array}\!\right]_{\!n}\!\!\mathrm{H}+m(\mathrm{Pr}^i\mathrm{O})_2\mathrm{Ti}(\mathrm{acac})_2
$$
$$
\xrightarrow{\mathrm{MeOH}} \mathrm{HO}\!\left[\!\left[\!\begin{array}{c}(\mathrm{OEt})_{2-x}\\|\\\mathrm{Si-O}\\|\\(\mathrm{OH})_x\end{array}\!\right]_{\!n}\!\!\mathrm{Ti}(\mathrm{acac})_2\!-\!\mathrm{O}\right]_{\!m}\!\!\mathrm{Pr}^i
$$
$$
+(2m-1)\mathrm{Pr}^i\mathrm{OH} \qquad\qquad (3)
$$
$$
x=0,\,1,\,2
$$

1. The product was allowed to react with PTP just after the hydrolysis of TEOS. The polytitanosiloxanes with spinnability were obtained by the reaction in molar ratios of r$_2$ from 1 to 0.067, according to the reaction flowchart shown in **Figure1**. Initially, the partial hydrolysis of TEOS was performed for 10min followed by addition of PTP, reflux for 1h and evaporation of solvents to obtain highly viscous solutions. The hydrolysis of TEOS at 22°C probably forms

Table 1. Preparation and spinnability of PTS.[1]

No.	Molar ratios		Hydrolysis Temp.(°C)[2]	TiO$_2$ (%)	Spinnability (cm)
	r_1	r_2			
1	3	1/1	0	50	100
2	3	1/1	-17	50	0
3	3	1/1	22	50	180
4	2	1/1	0	50	0
5	4	1/1	0	50	0
6	2	1/5	0	17	25
7	2	1/10	0	9	25
8	2	1/15	0	6	30[3]
9	2	1/20	0	5	0[4]

1) r_1=H$_2$O/TEOS; r_2=PTP/TEOS; HCl/TEOS=0.1
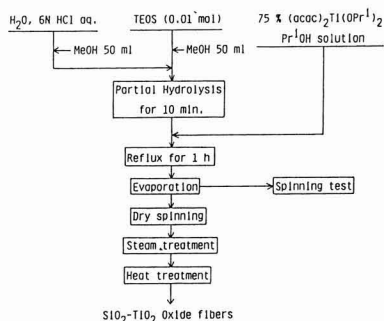2) Hydrolysis temperature of TEOS.
  Hydrolysis conditions; TEOS:10.8 g (0.05 mol)
                         MeOH:100 ml
3) Turned to gel after 5 h.
4) Turned to gel after 2 h.

Fig. 1. Flowchart of the preparation of SiO$_2$-TiO$_2$ glass fibers from TEOS and PTP by precursor method.

more condensed intermediates (eq. 2) which react with PTP to give the PTS with more complex and polymerized siloxane units, while reaction at -17°C forms product with a low degree of hydrolysis because the PTS shows no spinnability as shown in **Table 1**. Thus the partial hydrolysis of TEOS was carried out at 0°C in molar ratios of r_1 from 2 to 3. The concentrated PTS solutions showed high stability against gelation. No gelation was observed for the PTS No.1 (in Table 1) left alone in a sealed bottle for more than one year at room temperature, and the solution still showed good spinnability.

Precursor fibers were obtained by dry spinning of the polymer solutions obtained after concentration of the reaction mixture. Then the fibers were treated with steam followed by thermal treatment at 900°C to provide ceramic fibers. In this preliminary work, it was found that SiO$_2$-TiO$_2$ fibers of 50 and 4mol% showed tensile strength of about 640 and 580 MPa, respectively. Therefore this process should provide a useful method to prepare not only the SiO$_2$-TiO$_2$ ceramic fibers with variable TiO$_2$ content but also other SiO$_2$-M$_x$O$_y$ (M=Al, Zr) fibers. The effect of various moisture and thermal treatments on the mechanical properties of the fibers (4-50 TiO$_2$ mol%) and the characterization of the precursor polymers are under investigation.

References:
1) S.Yajima, K. Okamura, J.Hayashi and M. Omori, J. Am. Ceram. Soc., 59, 324-7 (1976)
2) D.Seyferth, G. H. Wiseman and C. Prud·homme, J. Am. Ceram. Soc., c-13-c14 (1983); Y. Nakaido, T. Matsuura, D. Yamashita, M. Okabe and S. Ishikita, Nippon Kagaku Kai-Shi, 1990, 487-93; O. Funayama, M. Arai, Y. Tashiro, H. Aoki, T. Suzuki, K. Tamura, H. Kaya, H. Nishii and T. Isoda, Nippon Seramikku Kyokai Gakujutsu Ronbunshi, 98, 104-7 (1990)
3) K. J. L. Paciorek, D. H. Harris, W. Krone-Schmidt and R. H. Kratzer, "Ultrastructure Processing of Advanced Ceramics.", ed. by J. D. Mackenzie and D. R. Ulrich, pp.89-97 (1988) and the literatures cited herein.
4) Y. Abe, T. Gunji, M. Hikita, Y. Nagao and T. Misono, Yogyo Kyokaishi, 94, 1243-45 (1986); T. Gunji, Y. Nagao, Y. Abe and T. Misono, J. Non-Crystal. Solids, 107, 149-54 (1989)
5) T. Gunji, Y. Abe and T. Misono, Polym. Prepr. Japan, 38, 4315-17 (1989)
6) J.C. Pouxviel and J. P. Boilot, J. Non-Crystal. Solids, 89, 345-60 (1987); Bruce D. Kay and Roger A. Assink, J. Non-Crystal. Solids, 104, 112-22 (1988); R. Campostrini, G. Carturan, G. Soraru and P. Traldi, J. Non-Crystal. Solids, 108, 315-22 (1989).

Mechanical Properties of SiC-Fiber Reinforced CVI-SiC Composite

Yoshio Akimune, Toshio Ogasawara, Naoto Hirosaki and Kouji Yoneda

Materials Research Laboratory, Central Engineering Laboratories, Nissan Motor Co., Ltd.

1, Natsushima-cho, Yokosuka-shi 237, Japan

Mechanical properties of a commercial SiC-fiber/CVI-SiC composite were examined. The composite showed high fracture toughness (12.5MPa m$^{1/2}$) and low strength (162MPa in tensile strength) compared to those for other engineering ceramics, resulting from fracture behavior dependent on the microstructure. The high fracture toughness is a result of fiber debonding and pull-out effects, while the low strength is associated with the porous microstructure.

1. Introduction

Lightweight, high-strength silicon nitride has been used in commercial automotive turbocharger rotors since 1985.[1] Another anticipated application is in the structural components of gas turbines. Silicon carbide (SiC) is one promising ceramic candidate for use in gas turbines because of its light weight and high heat resistance, although its fracture toughness is not so high.[2] As a result, efforts have been made to increase its fracture toughness using particle dispersion[2-3] and fiber reinforcement methods.[4-5] Several studies dealing with the fracture behavior of continuous-ceramic fiber reinforced ceramic matrix composites have been reported, which have suggested that improved toughness is obtainable.[6-10] The mechanical properties/structure relationship has gradually become clear through the results of those studies. However, in the case of gas turbine components having larger dimensions there is still some concern as to the relationship between the microstructure and required mechanical properties.

This paper reports the mechanical properties of commercial chemically vapor infiltrated SiC (CVI-SiC) reinforced by SiC-fiber (SiC-fiber/CVI-SiC) material and shows the mechanical properties level and fracture behavior of industrially produced SiC-fiber/CVI-SiC composites.*

2. Experimental Procedure

Commercially available SiC-fiber/chemical vapor infiltration (CVI)-SiC material* was obtained. It was a two-dimensional(2D) laminate Nicalon fiber/CVI-SiC, having 40vol% woven Nicalon fiber and 11 sheets laminated at 0/90 degrees. The fabric was chemically vapor deposited by carbon, then approximately 32% of the SiC was chemically vapor infiltrated.

Specimens having approximate demensions of 200mm×200mm×3mm were cut into pieces 40mm×4mm×3mm for a fracture toughness test, 80mm×8mm×3mm for a bending test, and 120mm×8mm×3mm for a tensile test. A fracture toughness test using chevron notched 4-point bend bars (40mm×4mm×3mm) was conducted according to a procedure developed by Sakai and Yamasaki.[11] The fracture toughness test is used to characterize composite failure behavior. The 4-point bending test was performed at a 0.5mm/min crosshead speed, and the tensile strength test was conducted at a cross head speed of 1.0mm/min. In addition, 8mm×8mm×3mm specimens were cut and polished to examine microstructure by optical microscopy and scanning electron microscopy (SEM).

3. Results and Discussion

The mechanical properties of the SiC-f/CVI-SiC composite are listed in **Table 1**. The SiC-f/CVI-SiC composite has low density resulting from the introduction of large-size pores. Young's modulus calculated from the stress-strain relation was also small, indicating the effect of the microstructure. **Figures 1A**, **1B** and **1C** show the microstructure revealing large pores in the woven SiC-f/CVI-SiC composite.[6] The diameter of the SiC-fiber ranged from 13.9 to 14.3μm.

Bending and tensile strength measurements were made to clarify the material properties.[6,7] Bending strength and tensile strength were 285MPa and 162MPa, respectively. The fracture caused during the bending test (**Figures 2A and**

Table 1. Materials properties.

	SiC-f/CVI-SiC composite
Density kg/m³×10⁻³	2.30±0.06
X-ray phase	beta-SiC
Bending strength (MPa)	285±22
Tensile strength (MPa)	162±8
Fracture toughness (MPa·m$^{1/2}$)	12.5±0.5
Young's modulus (GPa)	230

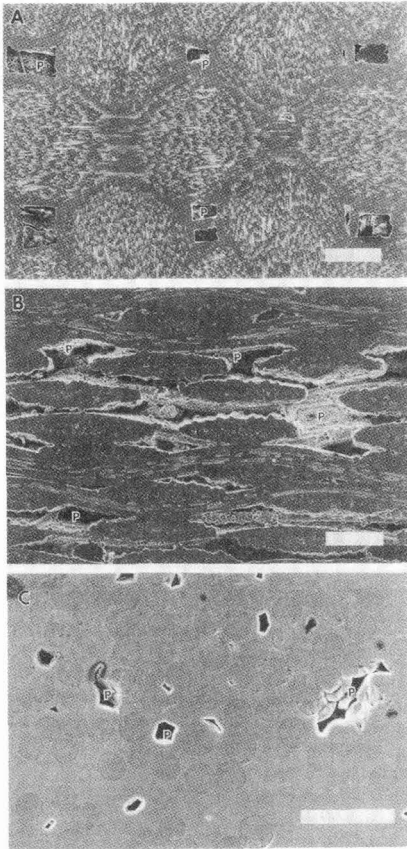Ten specimens were measured.
±1 Standard deviation.

Fig. 1. SEM micrographs revealing microstructural characteristics.
(P: pore)
(A) SiC-f/CVI-SiC composite, flatwise. (Bar=500μm),
(B) SiC-f/CVI-SiC composite, edgewise. (Bar=500μm),
(C) SiC-f/CVI-SiC composite, showing fiber, matrix, and pores.
(Bar=50μm).

Fig. 2. Fracture surface of bending test specimen.
(A) Specimen surface. (Bar: 2.0mm),
(B) Cross section. (Bar: 1.0mm).
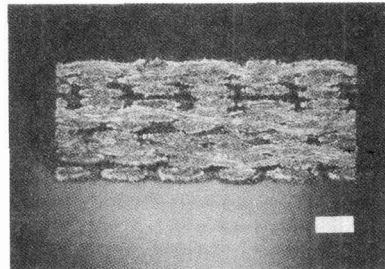
Fig. 3. Fracture surface of tensile test specimen.
(Bar: 1.0mm)

2B) occurred perpendicular to the surface. The crack then proceeded along a woven SiC sheet resulting in delamination,[5-8] since SiC fibers were woven parallel and perpendicular to the longitudinal direction of the specimen. SiC-fiber pull-out in the early stage of failure during the bending test was observed on the surface, but fibers were not completely pulled out. On the other hand, catastrophic fracture caused by tensile stress occurred perpendicular to the surface similar to the fracture behavior of monolithic ceramics in the tensile strength test (**Figure3**). SiC fiber orientation was the same as that of the bending test specimen. This fracture proceeded along the SiC-fiber oriented perpendicular to the longitudinal direction.

The fracture toughness test was conducted using a chevron notched specimen and fracture occurred in the edgewise direction.[10] Stable fracture was observed during this test, and fracture toughness was calculated from a load-load point displacement curve (**Figure4**). The results are in the same range of data reported for similar material.[10] The fracture toughness value includes uncertainty related to the complicated fracture process as noted later. SEM observa-
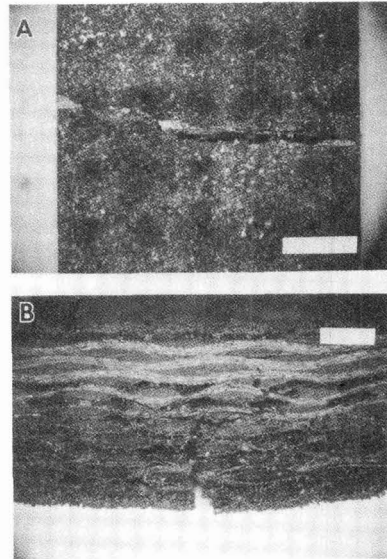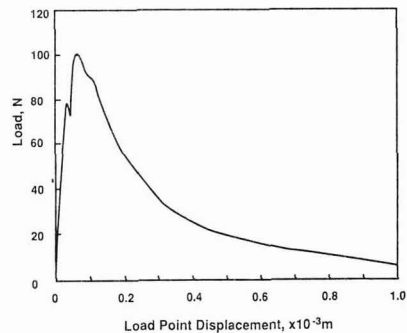

Fig. 4. Stress-load point displacement curve of chevron notched specimen.

tion showed the fracture surface of the specimen (**Figure5A**), revealing much fiber pull-out and matrix cracking
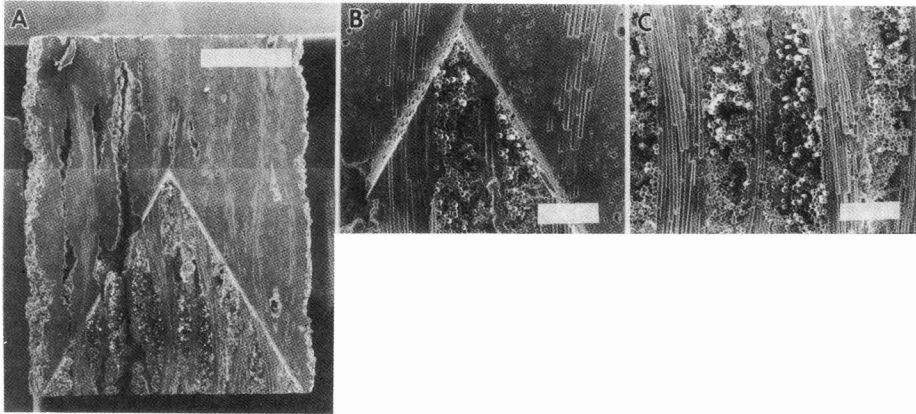
Fig. 5. Fracture surface of chevron notched specimen.
(A) Fracture surface of chevron notched specimen. (Bar: 1.0mm), (B) Fiber pull-out behavior at the early stage of fracture. (Bar: 200μm), (C) Fiber pull-out behavior at the final stage of fracture. (Bar: 200μm)

behavior (**Figures5B and 5C**), however the length of pull-out SiC-fiber is several times the fiber diameter. This composite displayed stable failure resulting from weak fiber-matrix interface, and the pull-out behavior was restricted by strong interface at curved fibers in contrast to that reported in other literature.[9,10] It is assumed that SiC-fiber is fractured in the early stage of debonding due to limitations of fiber debonding caused by the fabric structure. The fibrous structure may influence debonding behavior, resulting in a shorter value of pull-out length.

In this SiC-f/CVI-SiC composite, fracture occurred perpendicular to the direction of tensile stress. The fracture process is thought to occur as follows. Matrix cracking occurres first, followed by debonding at the fiber/matrix interface, and then fiber bridging occurrs.[12] At the final stage, the SiC fiber was fractured with short range debonding. In this process, matrix cracking, debonding, and fiber fracture occurred in a small range, and this may have contributed to the fracture toughness value, although fracture toughness in this experiment includes some uncertainty.

4. Summary

The mechanical properties of commercial SiC-fiber/CVI-SiC composites were examined in this short research. The composite shows low strength (162MPa in tensile strength) and high fracture toughness (12.5MPa m$^{1/2}$) compared to results reported for other engineering ceramics, because of its microstructure and fracture behavior. Low strength is thought to be the result of the porous microstructure. On the other hand, high fracture toughness resulted from fiber debonding and pull-out effects, and even pull-out length was small. The microstructure produced by the fabric structure may influence debonding behavior, resulting in a shorter value of pull-out length.

References:
1) M. Taguchi, "Application of High-Technology Ceramics in Japanese Automobiles," Advanced Ceramic Materials, 3 [3] 246-50 (1987).

2) G.C. Wei and P.F. Becher, "Improvement in Mechanical Properties in SiC by the addition of TiC Particle," J. Am. Ceram. Soc., 67 [8] 571-574 (1984).

3) C.H. McMurtry, W.D.G. Boecher, S.G. Seshadri, J.S. Zanghi, and J.E. Garnier, "Microstructure and Material Properties of SiC-TiB$_2$ Particulate Composites," Am. Ceram. Soc. Bull., 66 [2] 325-329 (1987).

4) E. Fizer, D. Hegen, and H. Strohmeier, "Chemical Vapor Deposition of Silicon Carbide and Silicon Nitride and Its Application for Preparation of Improved Silicon Ceramics," pp.525-35, in Proc. Seventh Int'l Conf. Chem. Vapor Dep., Edited by T.D. Sedwick and H. Kydtin, Electrochem. Soc., princeton, NJ. 1979.

5) A.J. Caputo and W.J. Lackey, "Fabrication of Fiber-Reinforced Ceramic Composites by Chemical Vapor Infiltration," Ceram. Eng. Sci. Proc., 5 [7-9] 654-67 (1984).

6) P.J. Laqmicq, G.A. Bernhart, M.M. Dauchier, and J.G. Mace, "SiC/SiC Composite Ceramics," Am. Ceram. Soc. Bull., 65 [2] 336-38 (1986).

7) A.J. Caputo, D.P. Stinton, R.A. Lowden, and T.M. Besmann, "Fiber-Reinforced SiC Composites with Improved Mechanical Properties," Am. Ceram. Soc. Bull., 66 [2] 368-72 (1987).

8) R.D. Veltri, D.A. Condit, and F.S. Galasso, "Chemical Vapor Deposited SiC Matrix Composites," J. Am. Ceram. Soc., 72[3] 478-80 (1989).

9) A.J. Eckel and R.C. Bradt, "Strength Distribution of Reinforcing Fibers in a Nicalon Fiber/Chemically Infiltrated Silicon Carbide Matrix Composite," J. Am. Ceram. Soc., 72 [3] 455-58 (1989).

10) Y.M. Pan, M. Sakai, J.W. Warren, and R.C. Bradt, "Toughness Anisotropy of A SiC/SiC Laminar Composite," pp.631-38, in the Proc. 21th University Conf. on Ceram. Sci., Plenum Press, NY (1986).

11) M. Sakai and M. Yamazaki, "Numerical Fracture Analysis of Chevron-Notched Specimen I, Shear Correction Factor," J. Am. Ceram. Soc., 66 [5] 371-75 (1983).

12) D.B. Marshall and A.G. Avans, "Failure Mechanisms in Ceramic-Fiber/Ceramic Matrix Composite," J. Am. Ceram. Soc., 68 [5] 225-31 (1983).

Preparation of Monodispersed Hydrous Aluminum Oxide Powders

.Nobuyasu Mizutani, Masaki Ikeda,[*] Lee Seok-Keun, Kazuo Shinozaki and Masanori Kato

Department of Inorganic Materials, Faculty of Engineering, Tokyo Institute of Technology,
2-12-1, O-okayama, Meguro-ku, Tokyo 152, Japan
[*]Nippon Light Metal Co. Ltd., 4025-1, Miho, Shimizu-shi, Shizuoka 424 Japan

Hydrolysis of aluminum secondary-butoxide in various solvents was studied. Mixed solvents of n-octanol and organic solvents affected the nature of the final products. Gel was formed when hydrophobic solvents were added, whereas sol was formed in the case of hydrophilic solvents. The mixed solvent of n-octanol and acetonitrile was found to be optimum in the preparation of monodispersed spherical powders. In addition, the influences of water, acetonitrile, dispersant, hydrolysis temperature and aging time on the preparation of monodispersed aluminum oxide particles were investigated.
[Received November 22, 1990; Accepted December 14, 1990]

1. Introduction

Metal alkoxides are generally very reactive and hydrolyzed vigorously. Only several moodispersed oxide powders have been produced by hydrolysis of metal alkoxides, mainly in dilute ethanol solutions. These are silicon[1], titanium[2], zirconium[3] and tantalum[4] oxides and doped oxides of these metals[3,5,6]. Monodispersed PZT particles also have been prepared by hydrolysis of complex alkoxide of Pb, Zr and Ti in a similar way[7]. These metals are relatively highly electronegative and their alkoxides are less reactive. Hydrolyzing more reactive alkoxides of less electronegative metal under the same condition results in the formation of gel or agglomerates. Unfortunately, one of these is aluminum alkoxide. The hydrolysis reaction of aluminum alkoxide may be presented as shown below[8]:

$$Al - OR + H_2O \rightarrow Al - OH + ROH \quad \ldots \ldots (1)$$

Following formation of hydroxy groups, polycondensation reaction occurs.

$$Al - OH + HO - Al \rightarrow Al - O - Al + H_2O \quad . . (2)$$

$$Al - OH + RO - Al \rightarrow Al - O - Al + ROH \quad . . (3)$$
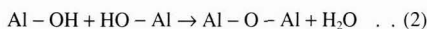
The higher hydrolysis rate leads to the formation of polymeric species when almost all alkoxids are consumed in solution. Crosslinking of these polymeric species results in a gel network. Therefore, it is necessary to retard hydrolysis reaction and promote three dimensional polycondensation reaction according to eqs.(2) and (3) for formation

of spherical particles. In conventional solvents, spherical particles could not be obtained from aluminum alkoxide. Recently, Riman et al.[9] prepared spherical particles of strontium titanate by hydrolyzing strontium-titanium double alkoxide in n-butanol-acetonitrile solvent. It is important to investigate the effects of mixed solvents composed of alcohols and other organic solvents on the hydrolysis of metal alkoxide and to find a new technique for controlling hydrolysis reaction.

2. Experimental

Aluminum sec-butoxide ($Al(O-sec-C_4H_9)_3$) (Soekawa Chemical Co. Ltd., Tokyo, Japan) was dissolved in a mixed solvent of n-octanol and an organic solvent selected from toluene, dimethyl ether, methyl iso-butyl ketone, acetone, 1,4-dioxane and acetonitrile (Wako Pure Chemical Industries, Ltd., Osaka, Japan). Water was dissolved in the same mixed solvent. When water was insoluble in the solvent, it was first dissolved in n-butanol and then in the solvent. Hydroxy-propyl-cellulose (HPC, Wako Pure Chemical Industries, Ltd., Osaka, Japan)[10,11] was added as a dispersant in alkoxide solution. Then, the water solution and alkoxide solution were mixed. The concentrations of the alkoxide, water, and HPC were 0.05 mol/l, 0.05mol/l and 0.2g/l, respectively. In the case of mixed solvents, the concentration of the organic solvent was 40vol% after two solutions were mixed. Hydrolysis temperature was 40°C and aging time was 1h. Products were centrifuged after aging. Next, the precipitates were redispersed in i-propanol in order to sample for TEM observation. The concentrations of acetonitrile, HPC, water, aging time and hydrolysis temperature were varied in the mixed solvent of n-octanol and acetonitrile in order to find out the optimum condition for preparation of monodispersed aluminum oxide particles. In this experiment, the concentration of the alkoxide was fixed at 0.05mol/l.

3. Result and Discussion

In alcohol solution, alcoholysis reaction of aluminum sec-butoxide is represented as follows:

$$Al(O - sec - C_4H_9)_3 + xROH \rightarrow$$
$$Al(O - sec - C_4H_9)_{3-x}(OR)_x + xsec - C_4H_9OH \quad (4)$$
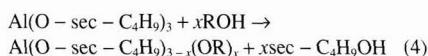
The alkyl chain length and degree of branching exerted a great effect on the hydrolytic stability of aluminum sec-

butoxides. The rate of hydrolysis reaction decreased with the increase of the alkyl chain length. As a result, particles tended to precipitate in higher alcohol solution. However, precipitated particles were still highly agglomerated in n-octanol solution, which is the highest liquid alcohol at room temperature.

Organic solvents mixed with n-octanol were found to affect the nature of the final products, as shown in **Figure1**. Gel was formed when one of toluene, dimethyl ether and methyl result-butyl ketone was added, and the structure of gel was different in each case. On the other hand, sol was formed when one of acetone, 1,4-dioxane and acetonitrile was added. In these cases, agglomeration was drastically reduced compared to that in unmixed solvent, n-octanol. The former solvents are hydrophobic and the latter solvents are hydrophilic. When a hydrophilic organic solvent is added to n-octanol, water is reasonably dissolved in this solvent and the alkoxide is dissolved in n-octanol. In such cases, hydrolysis reaction could be depressed because water and alkoxide molecules were separated by being dissolved with different solvent. Of course, the above consideration does not mean that any mixed solvent of a hydrophobic and

a hydrophilic solvent is always effective for the formation of spherical unagglomerated particles. For example, gelatinous precipitates were formed in the mixed solvent of toluene and acetonitrile. Furthermore, polycondensation reaction could also be influenced by solvents. According to eqs.(2) and (3), polycondensation reaction produces water and alcohol, and was affected by solution.

Figure2(a) shows geometrical standard deviation and the effect of the amount of acetonitrile on the formation fraction of unagglomerated particles. The formation fraction of unagglomerated particles was calculated by dividing the number of spherical particles by that of all particles. In this time, although the intense agglomeration was accompanied with the increase of the number of particles consisting of agglomeration, each agglomerate was calculated as one particle. The number of agglomerated particles decreased as acetonitrile concentration increased, and all particles were spherical and unagglomerated not less than 40vol%. It is considered that water dissolved in acetonitrile is more uniformly dispersed microscopically as acetonitrile concentration approaches 40vol%. Geometrical standard deviation was almost constant in the concentration range of
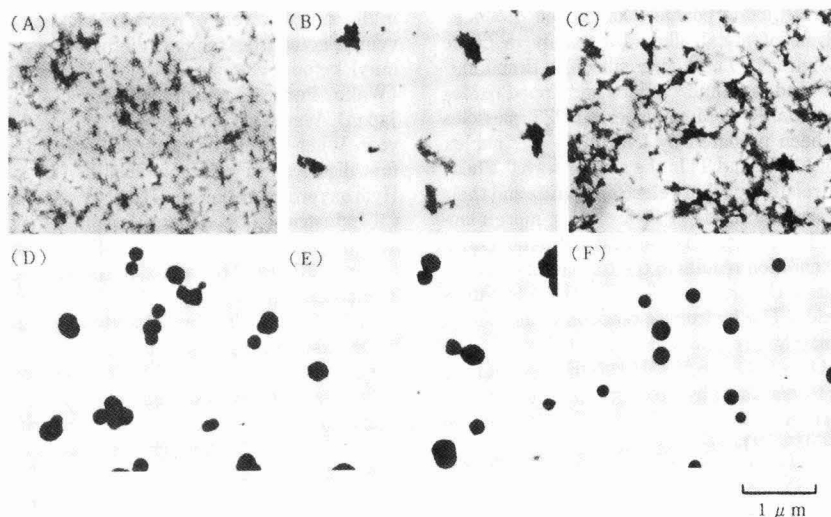
Fig.1. TEM photographs of Al₂O₃ particles precipitated by the hydrolysis of aluminum sec-butoxide in various organic solvents added to n-octanol; (A)toluene, (B)diethyl ether, (C)methyl iso-butyl ketone, (D)acetone, (E)1,4-dioxane, (F)acetonitrile.

(a)   (b)   (c)

Fig.2. Effect of (a) acetonitrile concentration, (b) water concentration, and (c) HPC concentration on agglomeration and geometrical standard deviation of particles.

Fig. 3. Growth curve of particles as a function of aging time.

Fig. 4. Effect of hydrolysis temperature on agglomeration and geometrical standard deviation.

10 to 40vol%. However, acetonitrile concentration higher than 40vol% resulted in polydispersed particles. Therefore, in this study, the optimum acetonitrile concentration was 40vol%.

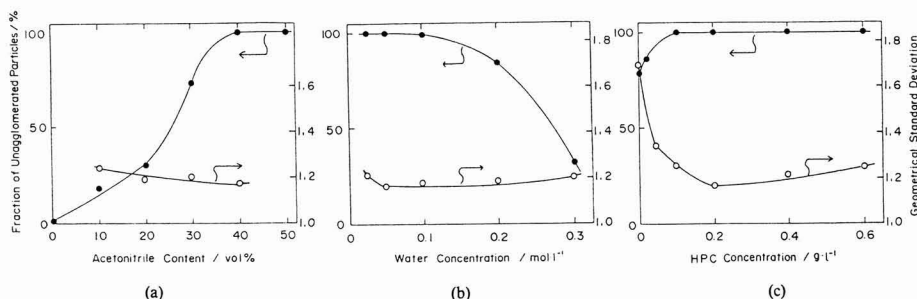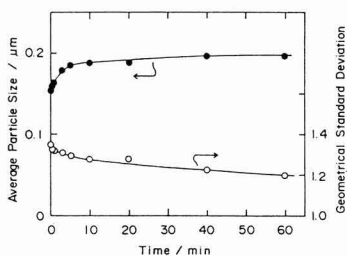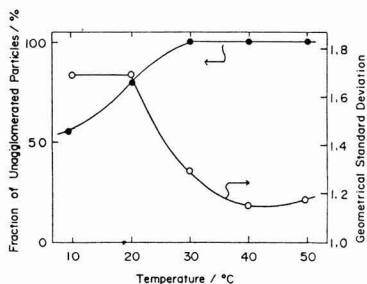Water concentration was also an important factor which affected the size and shape of particles. Geometrical standard deviation and the effect of water concentration in the formation fraction of unagglomerated particles is shown in **Fig.2(b)**. Particles did not agglomerate and particle size was 0.18-0.20um when water concentration was below 0.1mol/*l*. However, agglomerated particles appeared when water concentration was above 0.1mol/l because of a higher hydrolysis reaction rate.

Fig.2(c) shows the effect of the amount of HPC on the formation fraction of unagglomerated particles. 22% of the particles were agglomerated without HPC. The agglomerated particles disappeared when HPC concentration was not less than 0.1g/l. HPC molecules seemed to be adsorbed on particle surfaces, and prevented agglomeration. Therefore, HPC concentration of 0.1g/l was considered as the critical concentration at which all surfaces of particles were covered.

The change of average particle size and geometrical standard deviation according to aging time up to 1h were shown in **Figure3**. The average particle size and the geometrical standard deviation of the final products were 0.19um and 1.18, respectively. The growth rate of aluminum hydroxide particles was higher than those of other hydroxides such as TiO_2, ZrO_2, Ta_2O_5, etc., and the growth of particles was almost completed after 10min in spite of relatively low concentrations of the alkoxide and water. It could be assumed that since the hydrolysis reaction proceeds rapidly and consumes almost all alkoxide in a relatively short time, there is not enough alkoxide left for

growth. In general, particle size becomes uniform gradually throughout the growth process. However, this mechanism did not operate in this case, and geometrical standard deviation was reduced only down to 1.18. For obtaining larger and more uniform particle size, it is necessary further to retard hydrolysis reaction and to control particle growth rate.

Geometrical standard deviation and the effect of hydrolysis temperature on the formation fraction of unagglomerated particles is shown in **Figure4**. Particles were agglomerated at 20°C or less because n-octanol and acetonitrile were immiscible at such low temperature. Agglomerated particles were also observed at 80°C due to a high reaction rate similar to the case of higher water concentration.

Prepared particles were amorphous and converted to beomite, amorphous, γ-alumina and α-alumina by heating for 2h at 200°C, 400°C, 600°C and 1100°C, respectively. A weight loss of about 40% was observed when the products were heated at 1000°C for 2h.

4. Conclusion

Hydrolysis of aluminum sec-butoxide was drastically influenced by the selection of solvents. Hydrolysis reaction could be controlled in the mixed solvent of higher alcohol and hydrophilic solvent. Especially, the mixed solvent of n-octanol and acetonitrile was effective for the formation of spherical unagglomerated particles. The optimum conditions for preparing monodispersed aluminium oxide particles could be obtained as follows: an acetonitrile concentration of 40vol%, water concentration 0.05mol/l, HPC concentration 0.2g/l, aging time of 1h and hydrolysis temperature of 40°C. Prepared particles were amorphous and the weight loss was about 40% after heating at 1000°C.

References:
1) W. Stöber, A. Fink and E. Bohn, J. Colloid Interface Sci., 26, 62-69 (1968).
2) E.A. Barringer and H.K. Bowen, J. Am. Ceram. Soc., 65, C199-201 (1982).
3) B. Fegley, Jr. and E.a. Barringer, Mater. Res. Soc. Symp. Proc. Vol.32, Ed. by C.J. Brinker, Elsevier, New York (1984) pp.187-97.
4) T. Ogihara, T. Ikemoto, N. Mizutani, M. Kato and Y. Mitarai, J. mater. Sci., 21, 2771-74 (1986).
5) B. Fegley, Jr., P. White and H.K. Bowen, Am. Ceram. Soc. Bull., 64, 1115-20 (1985).
6) N.J. Jubb and H.K. Bowen, J. Mater. Sci., 22, 1963-70 (1987).
7) T. Ogihara, H. kaneko, N. Mizutani and M. Kato, J. Mater. Sci. Lett., 7, 867-69 (1988).
8) B.E. Yoldas. J. Appl. Chem. Biotechnol., 23, 803-09 (1973).
9) A.B. Hardy, G. Gowda, T.J. McMahon, R.E. Riman, W.E. Rhine and H.K. Bowen, "Ultrastructure Processing of Advanced Ceramics," Ed. by J.D. Mackenzie and D.R. Ulrich, Wiley-Interscience, New York, (1988) pp.407-28.
10) J. Jean and T.A. Ring, Am. Ceram. Soc. Bull., 65, 1574-77 (1986).
11) T. Ogihara, M. Ikeda, M. Kato and N. Mizutani, J. Am. Ceram. Soc., 72, 1598-601 (1989).

Information & Communications

News

Nanometer-level Control of Fine Ceramics Micro-structure

Prof. Shinichi Hirano, Faculty of Engineering, Nagoya Univ. has established a new processing technique to control the micro-structures of fine ceramics at a nanometer level. The new process controls the bond between the molecules by solution-reacting titanium and tin organic metallic compounds. The solutions are put in the form of films on the sapphire (or platinum, etc.) substrate. By heating, uniform crystalline films are synthesized. After that, by processing the films at a spinodal decomposition temperature, the phases abundant in titanium and tin are reciprocally oriented and crystallized at a nanometer level. He has also succeeded in crystallizing oxides of cobalt and iron by spinodal decomposition. The research is part of the international co-operative research-subsidizing activities of the Ministry of International Trade and Industry which has been entrusting from the fiscal year of 1988 to the New Energy and Industrial Technology Development Organization (NEDO). This technology can control not only micro-structures but also surface states and electronic properties of matter. So it is expected to be a processing technique for preparing new functional materials in the development of new sensors such as ceramics sensors and electronic materials.

Ceramic Composite Films To Filter 2 Nanometer Materials

TOTO Ltd. has developed the densest ceramic composite film in the world by using the ultrafiltration film which can separate materials of about 2 to 100 nm. This ceramic composite film is a 4-layer composition consisting of a supporting body, an interlayer, a precision filtering layer and a ultrafiltering layer, in order of roughness. Several layers of alumina and Zirconia are calcined onto the support body of the ceramic composite film and high-purity Zirconia is calcined onto the ultrafiltering film by a special sintering technique. The ceramic composite film can filter materials of more than 2 thousand times as large as the hydrogen atom. The film has excellent thermal and chemical resistance. As alkali-acid cleaning is possible, it can be used semi-permanently without clogs. It can be applied to the filtration of yeast and various bacteria in the manufacture of Japanese sake and wine. It can be also applied for highly viscous liquid separations and so on in the manufacturing process of medical drugs. At present, the size of separation films market is about 30 billion yen, the ceramic film has a market share of less than 10%. Future growth is wrong type face.

Non-linear Glass Added With 7 Kinds of Super-micro Grains

Prof. Katsumi Nagasaka and Associate Prof. Masayuki Nogami of Aichi Institute of Technology have succeeded in producing non-linear glass by doping silica glass with super-micro grains of 7 different compound semiconductors such as cadmium sulfide by the sol-gel method. The non-linear optical glass was prepared by the sol-gel method as follows. First hydrolysis of compounds of metallic alkoxide and salts of lead, cadmium and zinc produce a gel.

Then by heating this gel at a temperature of 500°C to 800°C, silica glass containing these metals was made. After this, the silica glass was reacted with hydrogen sulfide at room temperature and doped with super-micro grains of cadmium sulfide, zinc sulfide and lead sulfide. Finally, the silica glass doped with super-micro grains of cuprous chloride, cuprous bromide, selenium sulfide and cadmium telluride was prepared simply by the hydrolysis of these semiconductive compounds and heating them at 600°C to 900°C. The non-linear perception rate of cuprous chloride is 10^{-8}esu. The non-linear glass added with these super micro grains is expected to promote the development of optical-related elements such as optical switches and optical shutters.

Making Compositions of Lithium and Niobium at a Ratio of 1 to 1

Prof. Shinichi Hirano, Faculty of Engineering, Nagoya Univ. has succeeded in making a chemical composition of lithium niobate at the exact ratio of 1 to 1 by the sol-gel method. A composite alkoxide was first synthesized by the solution reaction of alkoxides of lithium and niobium. Then, by partial hydrolysis of this composite alkoxide, a structurally controlled gel was prepared and coated on substrate by the dip coating method. When sintering was conducted in a mixed gas of steam and oxygen at a temperature of 250°C to 400°C, an epitaxial film was synthesized. By the conventional preparing method, it was impossible to make the composition of lithium and niobium at a ratio of 1 to 1. Due to this, it was not possible to control the diffusion of titanium into the crystal and it was difficult to prepare uniform optical paths. By doping with titanium lithium niobate having a 1-to-1 composition ratio, a uniform and highly refractive optical wave path was produced. It is expected to be useful for the manufacture of non-linear optical composite elements and the development of chips on memory. This research result was announced at the second international ceramics science and technology meeting in the U.S.

New Process for Powder Diamonds

The study group of Associate Prof. M. Horio, Material Biotechnology, Faculty of Engineering, Tokyo Univ. of Agriculture and Technology has nearly completed development of a new process which can efficiently synthesize diamond powders of similar grain sizes. It may be possible to reduce the production cost to below one tenth that by the conventional methods. The plasma chemical vapor deposition (CVD) method was selected among the vapor methods for synthesizing diamonds at low pressures. Molybdenum was vapor-deposited on the porous carbon particles, which were then infused with a mixed gas of methane, hydrogen and argon, thereby forming a plasma in the vacuum container and infusing. It was then found that powdery diamond deposited around molybdenum packed inside innumerable pores of the carbon particles. Simply by changing the synthesis conditions such as the density and temperature of the gas, the grain size can be controlled in the range of 5 to 50μ. The study group considers that the larger the diamond-deposited area of carbon particles is, the more diamond is synthesized. It plans to study the structure of carbon particles, and to quickly establish a technique to eliminate carbon particles and collect diamond powders.

Bonding Machine for Aluminum and Ceramics

Altex Corporation starts to sell ultrasonic metal and ceramics depositing machines "CAW" series which bond aluminum and ceramics by using the ultrasonic vibration. The

joint method (which is now under a patent application) can display various data such as deposition gaps and strengths, and the quality of joint products, by inputting data such as energy levels and cycle times to the computer. The bonding is carried out by means of ultrasonic vibrations at 20 to 40 kilohertz. the bonding of aluminum and ceramics is completed in a few seconds. The price ranges from 2.5 to 6 million yen. Some are already scheduled for delivery to semiconductor manufacturers. In the future, the company will seek customers among domestic and overseas research laboratories of electrical equipment, automobile and semiconductor manufacturers. A dozen or so machines are expected to be sold in the first year.

Development of New Ceramic Bonding Technique

In co-operation with the Government Industrial Research Institute of Osaka and the Agency of Industrial Science and Technology, and financed by the Japan Key Technology Center, Daihen Corporation has developed a new bonding technique for ceramics. The bonding method involves the following process. First, researchers inserted fluoride

system bonding agents between two ceramics and pre-heated them to approx. 800°C by gas fire. They then impressed some thousands of voltages to this plane and bonded it with the heating effect (Joule heat). The current carrying time was only about six minutes, which is quite short. The results of bonding performance tests using silicon nitride ceramics showed a bending strength of 425 megapascals. This is equal to more than 85% of the mother material's strength. The bonding plane endurès temperatures higher than 1000°C, has strong esistance to acid and alkali, and has excellent anti-corrosion properties. Ceramics of many sizes can now be easily bonded and applied to silicon nitride, silicon carbide and alumina. At the moment, the companies are evaluating the market and plan to produce a bonding system in 3 to 5 years.
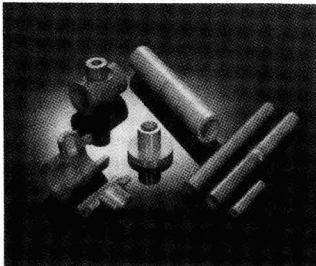
Static Blade Test under Actual Conditions

Tokyo Electric Power Co. has been developing heat-resistant ceramic gas turbines since 1984 to enhance the efficiency of combined cycles, with the objective of realizing a turbine output of 20,000kW at an inlet gas temperature of 1,300°C. The company recently, demonstrated the two-stage static blade system with Mitsubishi Heavy Industries, following the previously established combuster. A major problem in the development of the static blade is to prevent damage to ceramic parts of the first-stage blade by high thermal stress created during emergency stops; the blade is exposed to very severe thermal conditions while running. The new turbine system uses a first-stage static blade of silicon carbide and nitride, and a second-stage blade of silicon nitride, tests have been successfully conducted at 15kg/cm² and 1,300°C for the first-stage blade to confirm that the ceramic parts are sufficiently resistant to these conditions.
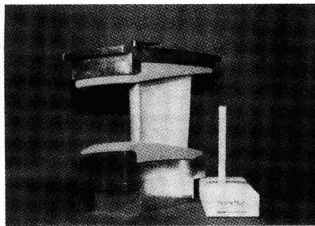
## New Slip Casting Method for Fine Ceramic Materials

Koransha has developed a new slip casting method to form fine ceramic products of complex shapes such as turbo rotors without using a gypsum mold. Slip adjustment is the key point of the development. The starting material (zirconia or silicon nitride) is ball-milled in the presence of water or alcohol as the solvent and a dispersant (such as ammonium polycarbonate) to form a slurry. The slurry is then degassed after adding a small quantity (3 to 8wt%) of reaction-hardening resin as the binder, and poured into a mold absorbing no moisture, (one of metal, resin and wood), to harden the slurry in a short time. The formed product is then dried and degassed in an oxidative atmosphere for a short time to remove the solvent. It is relatively hard, machinable, and turns into a fine ceramic article when sintered. The new process can be incorporated into an automatic system, and is also applicable to powder metallurgy. Achievements by the Superconducting Generator Development Association

The developmental work on an AC generator employing superconducting wires has taken 3 years. Fourteen electric power companies, electric machine manufacturers, and cable manufacturers formed the development team along with CRIPI and the Fine Ceramics Association. The team has developed high-temperature oxide superconducting wires through various processes including the doc-

tor blade process, plasma spray process, laser pedestal process, and CVD. The testing of these wires showed favorable results for the R&D phase. As for metallic materials, a wire which used aluminum as stabilizer has been developed for the first time. This type of wire demonstrated better performance than copper wires in showing less electric resistance. Heat generation is 1/10 that of a conventional type. The diameter of the filament has been reduced to a sub-micro range, while the current density increased to 10,000↓, so that it can also be used for transformer and transmission cables as well.

A basic design of a 70,000kW generator has been completed. Manufacture of a rotor and magnetic wire winding has begun. A field coil using superconducting wires can have its current vary inside the rotor and is kept in a vacuum. Three types of dampers which prevent AC magnetic flux and heat are being prepared. They are single-layer, cage and three-layer types. In 1991, a large damper of 3m long and 80cm in diameter will be manufactured. Square wire will be used for its starter.
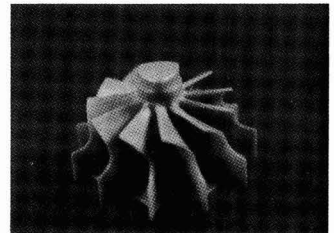
Non-Copper System Superconductor Showing 130K for Tc

NTT has developed a new type of superconductor which does not contain any copper. It is composed of Bi, V, and Sr. It therefore belongs to the vanadium system superconductor family, for which Hitachi announced its first developmental model on September 19,1990. However, NTT substituted tarium for bismuth. NTT prepared 15 samples, all of which showed the Meissner effect. A patent has been applied for. The starting materials were oxides of V and Sr. They were reduced in hydrogen atmosphere. At first, NTT announced that it confirmed the Meissner effect by five staff members independently. But it withdrew the first announcement which claimed the confirmation of the Meissner effect. Many other companies tested the process; however, no company was able to confirm the Meissner effect. NTT has again begun confirmation work on the Meissner effect.

Development of Bi System High-Temperature Superconductor Fiber

Prof. K. Matsushita, Nagaoka Technology and Science University, has succeeded in fabrication of fiber made of Bi system superconductor. Its critical temperature was 45K, lower than that of bulk; however, it was the first case where glass fiber having 2212 phases of the Bi system was produced.

He melted Bi, Sr and Ca at 1250°C and spread the mixture on the surface of a steel plate at 200°C to obtain glassy material. The bulk was annealed at an intermediate temperature between the glass transition and crystallization temperatures to form wire. Fibers of 20μm in diameter and 50cm long were covered with silver paste, which was then heated. With these processes, he successfully fabricated glassy fibers similar to optical fibers for telecommunications. The bulk of the Bi system showed a critical point of 80K, but that of the fibers was 45K. He said that when the crystalline grain was controlled, its critical point would increase further.

Skepticism of American Scientist over V System Superconductor

It has been reported that Hitachi, followed by NTT, announced the development of a V system superconductor. Voices of skepticism over it, however, have been raised by American scientists. In particular, Prof. Hasman said that he could not confirm there was any possibility of the creation of a V system superconductor, but that there was some possibility that it was not a superconductor. He claimed that Hitachi should confirm the Meissner effect by themselves.

Movements in Development of Superconducting Supercomputers

A magnetic flux quantum parametron project team headed by Prof. Goto has succeeded in the development of a magnetic flux quantum parametron, which has established fundamentals for superconducting supercomputers.

For a long time, the Japanese have had a lead in superconducting computers because Americans abandoned development of a Josephson computer. However, American engineers and scientists have begun R&D on superconducting computers again, and published R&D results. For example, Westinghouse has announced that they developed 4GHz Josephson elements. A technologist who had spun out from IBM announced a similar development as well. Although WH's achievement does not permit assembly of a computer, their elements showed the fastest performance in the world. Goto's magnetic flux quantum parametron works at 8GHz. Competitions have intensified.

Measurement of Stress at Very Low Temperatures

Kyowa Dengyo Co., Ltd. has developed a strain gauge which permits measurement of strains of a superconductor at very low temperatures of under the on-set point. It can measure displacements of up to 4mm at resolution of 0.015%. It is the first operational strain gauge ever developed.

Neodium Aluminate Single Crystal as Substrate for Superconductor

The National Research Institute for Inorganic Materials has developed a neodium/aluminate single crystal which can be used as a substrate for a superconductor. It has a crystal structure in which one neodium atom and one aluminum atom can be combined with three oxygen atoms.

Its lattice structure is close to that of a bismuth system superconductor when compared with the conventional magnesium oxide or strontium titanate. It permits fabrication of a substrate with a large area.

The single crystal is 60cm long, 23mm in diameter and red in color. Aluminum oxide powder is mixed with neodium oxide powder to be fused by CIP at a pressure of 1 ton. The green powder of the mixture is then melted at a temperature higher than 2050°c to form single crystals.

Increased Production of Multi-layered PC Board

Fujitsu Co. is producing multilayered printed circuit boards of over four layers for in-house demand, affiliated companies and customers; annual sales in 1989 reached 46 billion yen, which was the highest in the PC board business.

High production levels in super computers, general purpose computers, personal computers, etc., and high demand in affiliated companies in Japan and the U.S.A. necessitated the expansion of facilities in the Akasi plant, which will produce $22,000/m^2$ of mainly 6- or 8-layer boards monthly.

The Nagano plant production of multilayered boards of over ten layers will be transferred to the Akasi plant; the Nagano plant will now produce ceramic printed circuit boards for general-purpose and super computers.

To sell more boards along with the increased production, sales volume to affiliated and subsidiary companies will increase to 30% from 28%; as few U.S. manufacturer produce 18-to 20-layered boards, Fujitsu will receive the bulk of orders. In Japan, large boards and those of 6 or more layers will be targeted.

With this policy, the sales value will reach 55 billion yen yearly by March 1991.

Abstracts of Articles on Ceramics from the Selected Journals of the Academic Societies

Permeation Controls through an Adsorbed Monolayer of Alkylsilane Amphiphiles immobilized on a Porous Glass Plate

Katsuhiko ARIGA, Osamu SHIMIZU, Yasuhito EBARA and Yoshio OKAHATA*

Department of Biomolecular Engineering, Tokyo Institute of Technology ; Ookayama, Meguro-ku, Tokyo 152 Japan

Monolayers of alkylsilane amphiphiles were immobilized in a porous glass plate (average pore diameters were 50, 100, and 200 Å). Permeation rates of NaCl and water-soluble fluorescent probe across the porous glass plate occluded with the monolayer were reduced largely compared with those across the original glass plate. The 100 Å glass plate occluded with the monolayer reduced permeabilities effectively compared with other pore sizes in the glass plate. The permeation rate could be regulated by phase transitions from solid to liquid crystalline states of the immobilized monolayer of dialkylsilane amphiphiles. The mono-alkylsilane monolayers reduced the permeabilities only slightly and did not show the permeation change by the phase transition. The permeability were also influenced by the nature of the monolayer surface. The monolayer with the hydrophobic surface more reduced the permeation rate of NaCl than those with the hydrophilic surface. Permeation behaviors through the adsorbed monolayer were compared with those through the Langmuir-Blodgett (LB) monolayer transferred on a porous glass plate. The adsorbed monolayer reduced effectively as compared with the Langmuir-Blodgett (LB) monolayer on a porous glass plate. The LB monolayer was transferred only on the outer surface of the glass plate, while the adsorbed monolayer could ocllude both on the outer surface and inner core of the glass.

An Idea to Obtain Artificial Rain Falls on Arid Area by Man-made Mountain Range

Yoshito ISONO

(Director, Engineering Division, Taiyo Kogyo Corp.)

SYNOPSIS : — The possibility of obtaining artificial rain falls on arid area by the man-made mountain range with a huge air-supported membrane structure is discussed.

The arid area selected as a ideal geographical model is Saudi Arabia and various aspects of climate condition of the area are considerd.

The man-made mountain range proposed is held by continuously supplied air by many blowers. The minimum size of the structure will be 10km long, 1.2km width and 600m high.

The membrane material of the structure will be TEFLON coated glass fiber fabrics. And cable reignforcements at certain intervals are also recommended.

As a conclusion, the idea has high capability in realization of rain falls but more detailed research is required for the location of site, etc.

Key Words

Air-supported structure, Man-made mountain range, Artifical rain fall

Metal Coating of Carbon Fibers Using Organomentallic Compounds

Tamotsu TAKAHASHI
Department of Industrial Chemistry
The University of Tokyo
(7-3-1, Hongo,Bunkyo-ku, Tokyo, 〒113)

Development of functional materials by taking advantage of properties of organometallic compounds is discussed in this article.

Metals, metal oxides, and multimetal oxides are prepared by the CDL (chemical deposition in liquid phase) method by using liberation of ligands, reductive elimination, and complexation reactions of organometallic compounds. This method is applied for metal coating of carbon fibers. The advantages of metal coating using organometallic compounds by the CDL method over conventional melted-metal coating method or the CVD method are discussed.

^{63}Cu Knight Shift Study in High-T_c Superconductor Tl$_2$Ba$_2$CuO$_{6+y}$ with a Single CuO$_2$ Layer

Kenji FUJIWARA, Yoshio KITAOKA, Kunisuke ASAYAMA,
Yuichi SHIMAKAWA,[†] Takashi MANAKO[†] and Yoshimi KUBO[†]

*Department of Material Physics, Faculty of Engineering Science,
Osaka University, Toyonaka, Osaka 560*

*†Fundamental Research Laboratories, NEC Corporation,
4-1-1 Miyazaki, Miyamae-ku, Kawasaki 213*

^{63}Cu Knight shift in Tl$_2$Ba$_2$CuO$_{6+y}$ with a single CuO$_2$ plane has been measured by using a partially oriented powder with the *c-axis* perpendicular to the external field (K_{ab}). For the compounds with $T_c = 72$ K and 40 K, K_{ab} exclusively connected to the spin susceptibility (χ_s) is T-independent above T_c, while it decreases rapidly below T_c. By taking into account the T-independent orbital shift of $K_{orb} = 0.24\%$ and 0.26%, respectively, $\chi_s(T)$ is found to become almost zero below $T/T_c = 0.3$, in good agreemt with the isotropic energy gap (*s-wave*) model with a larger energy gap ($2\Delta = 4.4k_BT_c$) than the BCS value ($2\Delta = 3.5k_BT_c$). For the nonsuperconducting Tl$_2$Ba$_2$CuO$_{6+y}$, $K_{ab}(\chi_s)$ exhibits no T-variation, which is different from the behavior observed in other high-T_c oxides except YBa$_2$Cu$_3$O$_7$.

Transverse Relaxation of Cu Nuclear Spins in YBa$_2$Cu$_3$O$_{6.98}$

Yutaka ITOH, Hiroshi YASUOKA and Yutaka UEDA

*Institute for Solid State Physics, University of Tokyo,
Roppongi, Minatoku, Tokyo 106*

We have measured the transverse relaxation of the planar Cu(2) nuclear spins in an oriented powder sample of YBa$_2$Cu$_3$O$_{6.98}$ ($T_c = 92$ K) by using the nuclear quadrupole resonance (NQR) technique. Above T_c, after subtraction of the T_1 process, the spin echo envelope decay follows a Gaussian form, and its time constant is almost independent of temperature. In the vicinity of T_c, however, the Gaussian line shape is gradually narrowed. The calculated value ($T_G = 149$ μsec) for the Gaussian time constant based on the direct nuclear dipole-dipole interaction is comparable to the experimental one ($T_G = 131 \pm 2$ μsec) at 297 K. Hence, the nuclear indirect coupling proposed previously may not be needed. Below T_c, the Gaussian line shape was found to be narrowed depending on H_1, and especially, it is sharply narrowed at 35 K and 87 K.

Cu-NQR Study of Successive Magnetic Phase Transition in Antiferromagnetic YBa$_2$(Cu$_{1-x}$T$_x$)$_3$O$_6$ (T=Fe, Co and Ni)

Tomomasa TAKATSUKA, Yoyu NAKAMICHI and Ken-ichi KUMAGAI

*Department of Physics, Faculty of Science,
Hokkaido University, Sapporo 060*

Split spectra of Cu nuclear quadrupole resonance (NQR) in the chain (Cu(1)) site of the antiferromagnetic YBa$_2$(Cu$_{1-x}$T$_x$)$_3$O$_6$ (T=Fe, Co, and Ni) show that the spin alignment of Cu moments in the CuO$_2$ plane changes at a critical concentration of the substitution of Cu by T. The spin structure of the low-temperature magnetic phase is discussed.

[nuclear quadrupole resonance (NQR), antiferromagnetic order, YBa$_2$Cu$_3$O$_6$]

ESR Study of Ferroelectric Phase Transition in h-BaTiO$_3$

Masayoshi SHIMOKOSHI* and Kikuo OHI

*Department of Physics, School of Science and Engineering,
Waseda University, Shinjuku-ku, Tokyo 169*

Angular dependence of Fe^{3+} ESR spectra in hexagonal BaTiO$_3$ has been measured around the ferroelectric phase transition temperature of 66 K (T_c). The principal axes of crystal field tensor rotate in the *ab*-plane with decreasing the temperature from T_c to 51 K. The rotation angle becomes 30° at 51 K and the axes do not rotate below 51 K. Analysis due to the superposition model indicates that shear strain u_{sy} appears in the *ab*-plane between T_c and 51 K, and the symmetry becomes monoclinic 2.

[h-BaTiO$_3$, ferroelectric phase transition, ESR, superposition model]

*   Present address: Research Center, Denki Kagaku
Kougyo Co. Ltd., Machida, Tokyo.